Electro-chemo-mechanical coupling of nanoporous gold at the microscale

Vom Promotionsausschuss der
Technischen Universität Hamburg

zur Erlangung des akademischen Grades

Doktor-Ingenieurin (Dr.-Ing.)

genehmigte Dissertation

von
Yijuan Wu

aus
Nanning, China

2022

Gutachter der Dissertation

Prof. Dr. Erica Lilleodden

Institute of Material Research, Materials Mechanics
Helmholtz-Zentrum Hereon, Germany

Prof. Dr.-Ing. Jörg Weißmüller

Institute of Materials Physics and Technology
Hamburg University of Technology, Germany

Vorsitzender des Prüfungsausschusses

Prof. Dr.-Ing. Robert Meißner

Institute of Polymers and Composites
Hamburg University of Technology, Germany

Tag der mündlichen Prüfung

25th February 2022

ORCID: 0000-0002-2648-9938

DOI: https://doi.org/10.15480/882.4256

Abstract

Its tunable strengthening, stiffening and actuation behavior, induced by a change of surface state controlled via electrochemical potential, make nanoporous gold (NPG) a promising candidate for many applications. Due to the complex network structure, a fundamental understanding of the functional behavior of NPG requires accurate measurements of the electro-chemo-mechanical coupling. While many experiments at the macro-scale were published, only few experiments have been carried out at the micro-scale. In this work, the micromechanical testing with and without electrochemical control has been carried out, using a modified nanoindentation system with which the effects of deformation length-scale and microstructural length-scale are investigated.

Based on the results of nanoindentation and microcompression without electrochemical environment, the elastic modulus, strength and hardness show a decrease with increasing ligament size. By varying ligament size (L) and sample diameter (D) of NPG micropillars, a critical ratio ($\alpha=D/L=20$) was found, above which the test structure can be considered a representative volume element (RVE) resulting in reproducible stress-strain behavior and uniform deformation. Below this critical ratio, both flow stress and elastic modulus decrease with decreasing pillar diameter, as evidenced for a fixed ligament size of L=350 nm. Stochastic behavior along with non-uniform deformation for $\alpha<10$, indicate that the size of the load-bearing unit is close to 10 times the corresponding ligament size.

In the case of *in situ* microcompression, a novel loading profile was developed to decouple the contribution of displacement due to the actuation from the compression-induced deformation. The flow stress of pillars under potential jumps exhibited the same trend as the corresponding macroscopic results; strength is enhanced significantly due to the surface adsorption, and this response is reversible. The amount of previous deformation of pillars with a clean surface has no impact on the subsequent flow stress coupled with adsorption. The elastic modulus was found not to depend on the potential, in contrast to what was found with dynamic mechanical analysis at the macro-scale. The stress-strain curves of pillars with varying α indicate that the relative change in strength induced by adsorption ($\Delta\sigma/\sigma_{off}$) decreases with increasing ligament size, i.e. the absolute change in strength and the strength itself scale differently with the ligament size. A change in pillar size does not impact the $\Delta\sigma/\sigma_{off}$ for a fixed ligament size, even though α is below the ratio of the RVE for the mechanical behavior.

Zusammenfassung

Sein einstellbares Verstärkungs-, Versteifungs- und aktorisches Verhalten, das durch eine über das elektrochemische Potenzial gesteuerte Änderung des Oberflächenzustands hervorgerufen wird, macht nanoporöses Gold (NPG) zu einem vielversprechenden Kandidaten für zahlreiche Anwendungen. Aufgrund der komplexen Netzwerkstruktur erfordert ein grundlegendes Verständnis des funktionellen Verhaltens von NPG genaue Messungen der elektrochemisch-mechanischen Kopplung. Während auf der Makroebene bereits viel untersucht wurde, ist auf der Mikroebene noch wenig geschehen. In dieser Arbeit wurden mikromechanische Tests mit und ohne elektrochemische Umgebung durchgeführt, wobei ein modifiziertes Nanoindentationssystem zum Einsatz kam, mit dem die Auswirkungen der Verformungslängenskala und der mikrostrukturellen Längenskala untersucht wurden.

Die Ergebnisse der Nanoindentation und der Mikrokompression ohne elektrochemische Kontrolle zeigen, dass der Elastizitätsmodul, die Festigkeit und die Härte mit zunehmender Ligamentgröße abnehmen. Durch Variation der Ligamentgröße (L) und des Probendurchmessers (D) von NPG-Mikrosäulen wurde ein kritisches Verhältnis ($\alpha=D/L=20$) gefunden, oberhalb dessen die Teststruktur als repräsentatives Volumenelement (RVE) betrachtet werden kann, was zu einem reproduzierbaren Spannungs-Dehnungsverhalten und einer gleichmäßigen Verformung führt. Unterhalb dieses kritischen Verhältnisses nehmen sowohl die Fließspannung als auch der Elastizitätsmodul mit abnehmendem Säulendurchmesser ab, wie für eine feste Ligamentgröße von $L=350$ nm nachgewiesen wurde. Stochastisches Verhalten zusammen mit ungleichmäßiger Verformung für $\alpha<10$, deuten darauf hin, dass die Größe der tragenden Einheiten nahe dem Zehnfachen der entsprechenden Ligamentgröße liegt.

Im Falle der Mikrokompression in situ wurde ein neuartiges Belastungsprofil entwickelt, um den Beitrag zur Verschiebung durch Aktorik und durch kompressionsinduzierte Verformung zu entkoppeln. Die Fließspannung von Säulen unter Potenzialsprüngen zeigte denselben Trend wie die entsprechenden makroskopischen Ergebnisse; die Festigkeit wird durch die Oberflächenadsorption deutlich erhöht und diese Reaktion ist reversibel. Das Ausmaß der vorherigen Verformung von Säulen mit sauberer Oberfläche hat keinen Einfluss auf die sich einstellende Fließspannung in Verbindung mit der Adsorption. Es wurde festgestellt, dass der Elastizitätsmodul nicht vom Potenzial abhängt, im Gegensatz zu Ergebnissen der dynamisch-mechanischen Analyse auf der Makroebene. Die Spannungs-Dehnungs-Kurven von Säulen mit unterschiedlichem α zeigen, dass die relative Änderung der Festigkeit durch Adsorption

($\Delta\sigma/\sigma_{off}$) mit zunehmender Ligamentgröße abnimmt, d.h. die absolute Änderung der Festigkeit und die Festigkeit selbst skalieren unterschiedlich mit der Ligamentgröße. Eine Änderung der Säulengröße wirkt sich bei fester Ligamentgröße nicht auf $\Delta\sigma/\sigma_{off}$ aus, selbst wenn α unter dem Verhältnis der RVE für das mechanische Verhalten liegt.

Acknowledgements

I would like to express my gratitude to the following people who encouraged and supported me throughout my doctoral studies. I would not have been able to complete this work without their guidance and help.

First and foremost, I deeply grateful to my supervisor, Prof. Erica Lilleodden, for giving me the opportunity to work in her group, and for her invaluable advice, patience and consistent support during my PhD study. Her immense knowledge and plentiful experience have encouraged me in all the time of my academic research and daily life. I am proud of my time working with her.

My gratitude extends to my co-supervisor, Dr. Jürgen Markmann. His enthusiasm, insight, and knowledge into the subject matter steered me through this research. The door to his office was always open whenever I ran into troubles or had questions. I have learned a lot from the discussion with him.

I would like to offer my special thanks to the second reviewer, Prof. Jörg Weißmüller, for his valuable comments regarding my dissertation. I also gratefully thank Prof. Robert Meißner for agreeing to be the Chairman of my PhD defense. Additionally, I would like to extend my thanks to Prof. Norbert Huber for his helpful suggestions about my work.

I would like to express my acknowledgements to all my colleagues I am working with in the past of five years at the Helmholtz-Zentrum Hereon: Dr. Henry Ovri, Dr. Markus Ziehmer, Dr. Paula Guglielmi, Dr. Nadiia Mameka, Dr. Shan Shi, Dr. Jie Li, Dr. Murilo Hablitzel, Dr. Xin Zhang, Dr. Maowen Liu, Mohammadhadi Maghsoudi, Claudia Richert, Xinyan Wu, Yong Li, Stefan Berger, Olga Matts, Lukas Riedel, Seoyun Sohn. Thank all of you for the help in the lab and the scientific discussions. I would like to thank Stephanie Koch for her assistance with official matters. In addition, financial support from the German Research Foundation (DFG) via SFB 986 Tailor-Made Multi-Scale Materials Systems Project B8 is gratefully acknowledged.

Finally, I want to thank my parents for their love and support. Many special thanks go to my husband for his tremendous understanding, encouragement and company during these years.

Contents

Nomenclature

A	contact area of indenter
A_s	surface area
c	capacitance of the double-layer
CE	counter electrode
CSM	continuous Stiffness Measurement
CV	cyclic voltammogram
D	Pillar diameter
D_{bottom}	diameter at the bottom of pillar
d	sample dimension
DMA	dynamic mechanical analysis
E_{Au}	elastic modulus of bulk Au
E	elastic modulus of the tested sample
E_{NPG}	elastic modulus of NPG
E_i	elastic modulus of indenter
E_r	effective elastic modulus
E_p	elastic modulus of the micropillar
EBSD	electron backscatter diffraction
EDX	energy-dispersive X-ray spectroscopy
E_{SHE}	potential vs. SHE
E_{pzc}	potential at zero charge
ETD	everhart thornley detector
f	half the trace of the surface stress tensor
f_{pzc}	surface stress at zero charge
FCC	face-centered cubic

FIB	focused ion beam
G	excess free energy
H	hardness
H_0	initial height of pillar
h_{raw}	raw displacement of microcompression
h_p	displacement of pillar during microcompression
$h_{substreate}$	displacement of substrate during microcompression
h_{LF}	displacement of load frame during microcompression
h	nanoindentation displacement
h_s	depth of sink-in during nanoindentation
h_c	contact depth during nanoindentation
$\mathbf{I}$	second-order identity tensor
IHP	inner Helmholtz plane
K_s	stiffness of the supporting spring
L	ligament size
NP	nanoporous
NPG	nanoporous gold
OCP	open circuit potential
OHP	outer Helmholtz plane
P	raw load of nanoindentation
P_{max}	maximum load during nanoindentation testing
P_{raw}	raw load of microcompression
P_p	load on pillar
q	charge density
RE	reference electrode
RVE	representative volume element

$\mathbf{s}$	surface stress
$\mathbf{s}^{\mathrm{L}}$	surface stress in Lagrangian coordinate
S	contact stiffness
S_{LF}	stiffness of load frame
S_p	stiffness of pillar
SCCM	standard cubic centimeter per minute
SCE	saturated calomel electrode
SEM	scanning electron microscopic
SHE	standard hydrogen electrode
T	temperature
TEM	transmission electron microscopic
TLD	thru-the-Lens detector
V_{Au}	volume of Au
V_{NPG}	volume of NPG
WE	working electrode
α	ratio of pilar diameter (D) to ligament size (L)
σ	engineering stress
$\sigma_{y,Au}$	yield strength of bulk Au
$\sigma_{y,NPG}$	yield strength of NPG
ε	engineering strain
γ	surface tension
γ^L	surface tension in Lagrangian coordinate
μ_i	chemical potential
β	a constant that depends on the geometry of the indenter
ϵ	geometric constant of indenter
ϑ	Poisson's ratio of the tested materials

ϑ_i	Poisson's ratio of the indenter
ς	electrocapillary coupling coefficient

1 Introduction

1.1 Motivation and objectives

Owing to the high specific surface area, nanoporous metals with a stochastic bicontinuous network structure composed of nanometer-sized metallic ligaments and pores, exhibit interesting functional behavior induced by external stimuli. For instance, an application of an electrical potential to nanoporous gold (NPG) results in a strain, while the straining of NPG can cause a measurable voltage or current, which is not commonly found in conventional metals [1]. These functional properties make them promising candidates as actuators [2], sensors [3] and catalysts [4].

Dealloying is one of the most effective methods for producing NPG as well as other nanoporous metals, such as NP Pt [5], NP Cu [6] and NP Pd [7], during which the less noble element is selectively dissolved from a master alloy, resulting in a sponge-like and open-cell network structure consisting of interconnected ligaments and pores [8], as shown in Figure 1.1. Importantly, the ligament size of NPG can be adjusted from tens to hundreds of nanometers by controlling the dealloying conditions and post annealing treatment [9].

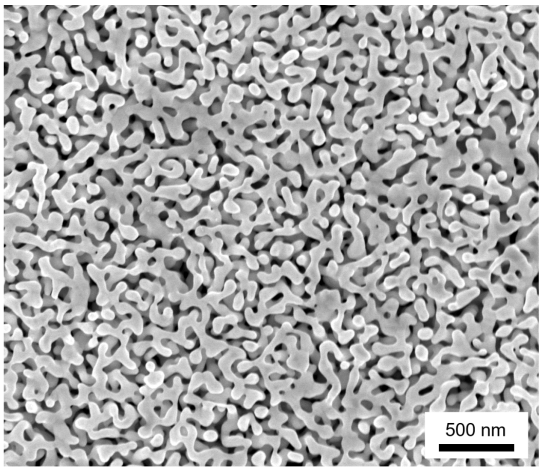

Figure 1.1. Scanning electron microscopic (SEM) image of nanoporous gold (NPG) made by electrochemical dealloying.

The functional behaviors, such as actuation and sensing, are inherently mechanically coupled; the amount of actuation for a given applied potential or the strength of the signal sensed for a given strain applied is dependent on the mechanical properties. Any possible applications requires the comprehensive understanding in mechanical behavior of this material because it has a considerable influence on the actuation capability if stress is applied to such an actuator, i.e. if it really has to do work against an external load. Therefore, the interdependencies of mechanical behavior, microstructure of NPG, and electrochemical environment, have attracted increased interests in the past of decades [10-15].

It was found that the elastic modulus and yield strength of NPG, predicted by the Gibson-Ashby scaling law, where the relative density is the sole impact factor, are not in agreement with the experimental measurements [16]. In addition, other structural features, such as ligament size, morphology and topology of the network structure were demonstrated to have significant impacts on mechanical properties of NPG [17-19]. However, due to the complexity and disorder of the porosity structure and length-scales involved, it is still challenging to understand the correlations between the structure and mechanical responses comprehensively. Especially, the effect of the ratio of specimen size (deformation length-scale) to pore or ligament size (microstructural length-scale), which was found to play an important role in determining mechanical behavior of cellular Al foams: a reduction of such ratio at a certain range causing a decrease in Young's modulus and plastic collapse strength [20], has not been systematically investigated in NPG. Besides, the recent mechanical results of hierarchical NPG revealed that both sizes of upper-hierarchical-level struts and lower-hierarchical-level struts have significant influence on the elastic modulus [21]. Since the ligaments of hierarchical structures are themselves nanoporous, these results indicate that the impact of sample size of NPG can not be neglected especially when only several ligaments cross span the samples.

Interestingly, the application of external signals can not only bring functional behavior to NPG, but also affects mechanical properties. When NPG samples are immersed in an electrochemical environment, such as $HClO_4$ or HCl aqueous solutions, the surface state of Au can be altered from an electrical double layer to electrochemical adsorption by an applied potential [22]. It was found that the formation of an oxidation monolayer on the NPG ligament surface caused by applied potential can lead to a ~10% increase in elastic modulus [23], and even a twofold increase in strength during compression. These variations in mechanical properties can be controlled reversibly by cyclic potentials [24]. Yet the mechanism of this electro-chemo-mechanical coupling is still under debate, and both sides of the debate will be

presented in chapter 2. While most investigations of mechanical responses coupled by electrochemical potentials are carried out on macroscopic NPG samples, a better understanding of the underlying correlations between structure, chemical states, and mechanical behavior is best achieved via micromechanical testing *in situ* in an electrochemical environment. Such an approach allows us to measure mechanical responses of micro-scaled volumes or even several load-bearing units under electrical potentials, by which we can address the effects of microstructure aspects, sample size and local structural geometries. Micromechanical approaches, such as nanoindentation, microcompression and microbending, employed for testing mechanical response of micro- and nano-scale objects, provide opportunities to observe changes in the dependence of strength on specimen size, which are not observed in macroscopic samples.

Nanoindentation testing with a sharp tip in electrochemical or other liquid environments has been conducted in some studies. The effect of surface covered by a metal or an oxide monolayer on the elastic-plastic transition of Au was addressed by Corcoran *et al*. [25, 26]. Recently, Barnoush *et al*. [27-29] studied the influence of hydrogen on dislocation nucleation of FeAl and Ni using a designed nanoindenter setup, where the samples were immersed in the electrolyte. However, in the case of nanoporous gold, the actuation response induced by potentials simultaneously needs to be considered during testing, which makes the experimental setup more challenging. Additionally, with the reduction of sample size to the microscale, whether existing size effects on mechanical behavior coupled with electrochemical potential is unclear.

One of the objectives of the current thesis is the achievement of electro-chemo-mechanical coupling measurements on micro-scaled NPG samples by means of a modified nanoindenter equipped with an electrochemical cell. With the help of a multiple load-unloading profile, actuation of NPG that has significant influence on the load and displacement measurement can be decoupled during testing. The elastic and plastic responses coupled with electrochemical potentials obtained from our setup are compared with the corresponding macroscopic results. Furthermore, micromechanical testing, including nanoindentation and microcompression, are carried out on NPG samples with and without electrolyte. By varying the ligament size and the external diameter of micropillars fabricated by focused ion beam (FIB) milling, the effects of deformation length-scale and microstructural length-scale on the mechanical behavior with and without electrochemical coupling are investigated. In addition, the dependence of plastic

behavior on the deformation history of NPG pillars under various potentials was also studied in this work.

1.2 Outline of thesis

Chapter 2 focuses on the background of the current thesis. Mechanical behavior and its correlation with NPG structure in the literature are reviewed, followed by an introduction of fundamental knowledge in terms of metal-electrolyte interface and electrochemical adsorption on the Au surface. Finally, the influence of surface state on properties of nanoporous materials is described.

Chapter 3 first introduces the electrochemical systems and techniques used in the current work, and then details the preparation procedure of bulk NPG samples and micro-pillars. Additionally, the techniques used for microstructural characterization and micromechanical testing carried out on NPG are presented.

In chapter 4, results from microcompression of NPG with varying ligament size and pillar diameter are presented. Basing on that, the influences of deformation length scale and microstructure length scale on elasticity and plasticity of NPG were discussed, and a critical ratio is found above which the test structure can be considered a representative volume of material resulting in reproducible stress-strain behavior and uniform deformation.

Chapter 5 presents the results of microcompression of NPG micro-pillars *in situ* in an electrochemical environment under potential control using a modified nanoindenter. A novel loading protocol is developed to decouple the dimension of change of samples from actuation and the imposed deformation. The elastic and plastic behaviors under different types of potential control was studied. The results obtained are compared to the corresponding results measured at the macroscale from literature.

In chapter 6, the influences of deformation length scale and microstructure length scale, as well as deformation history, on the plastic behavior of NPG coupled with electrochemical potentials is investigated. The size effects on mechanical behavior with and without electrolyte (in Chapter 4) are compared and discussed here.

Chapter 7 summarizes the main findings of the current thesis and proposes suggestions for further work.

2 Background

2.1 Mechanical behavior of nanoporous gold

At present, NPG is mainly prepared by dealloying that allows the selective dissolution of one or two components in an aqueous medium from a parent alloy, resulting in a stochastic nanoporous structure formed inside the residual alloy [8, 9, 14, 30, 31]. Due to this unique bicontinuous network structure, consisting of numerous disordered nano-scaled struts, NPG exhibits interesting functional behavior [32] that is not found in conventional metals, but the structural complexity makes understanding of correlations between structure and properties challenging. The elastic and plastic responses of NPG from the macro- to micro-scale were studied via many experiments [33-35], including tension [36], compression [10] and nanoindentation [17], and simulations [37-39].

2.1.1 Gibson-Ashby scaling laws

Scaling laws proposed by Gibson-Ashby in 1988 [40, 41], which are based on a model of 3D periodic constant section struts interconnected at rigid nodes, representing the conventional open-cell foam structure, can be used for predicting the mechanical properties of porous solids. According to the scaling laws, where the solid fraction and corresponding mechanical properties of the bulk materials are the two factors taken into account, the elastic modulus and yield strength of NPG are obtained by:

$$E_{NPG} = E_{Au}(\frac{V_{Au}}{V_{NPG}})^2 \tag{2.1}$$

$$\sigma_{y,NPG} = 0.3\sigma_{y,Au}(\frac{V_{Au}}{V_{NPG}})^{3/2} \tag{2.2}$$

Where E_{Au} and $\sigma_{y,Au}$ are elastic modulus and yield strength of the bulk Au, respectively. V_{Au}/V_{NPG} is the relative density of NPG. These equations work well for macroscopic conventional porous materials with low solid fraction (around 0.1) and micro or macro cell size [42]. However, in the case of NPG with solid fraction typically ranging between 0.2 and 0.5 [8, 35, 43], the mechanical properties predicted by this law is not consistent with the corresponding experimental measurements. This discrepancy might be because the random bicontinuous

structure of NPG composed of ligaments with different shapes, curvatures and space orientations, is more complicated than the ordered structure proposed in Gibson-Ashby model.

2.1.2 Size effects

2.1.2.1 Plasticity

Unlike macro cellular foams, where the cell size has a minimal effect in the mechanical behavior [44], the yield strength of NPG is strongly dependent on ligament size. It is increasing significantly with decreasing ligament size even if the relative density is identical. Many studies suggested the ligament size-dependent strength of NPG can be interpreted as the "size effect" of massive gold, since the single ligaments of NPG can be treated as Au nanowires.

The "smaller is stronger" size effect refers to a phenomenon that flow stress for plastic deformation in small volumes is higher than that needed for plastic flow in bulk materials, which has been found on many metals [45], such as Ni and its alloys [46-50], Cu [51-54] and Au [45, 55-57]. The mechanical testing results of face-centered cubic (FCC) metals indicates that the relationship between yield strength (σ_s) and sample dimension (d) at the submicron scale can be described by a simple power-law: $\sigma_s \propto d^{-n}$ [58]. In the case of Au, the values of n estimated by experiments (0.61 [57]) and by simulation (0.49 [59]) agree well. The yield strength of Au nanowires or ligaments as a function of sample dimension is illustrated in Figure 2.1 (a) [35]. It was demonstrated that the yield strength of Au increases dramatically from 50 MPa to 560 MPa as the sample size decreases from 11 μm to 200 nm [57]. In particular, the yield stress of Au ligaments with diameter of 15 nm, calculated using Gibson-Ashby scaling laws based on the measured yield stress of NPG, is around 1.5 GPa [60], approaching the theoretical shear strength of Au and is up to 50 times higher than the strength of bulk Au (30 MPa) [61].

Due to the huge discrepancy in yield stress between bulk and nanoscaled ligaments induced by size effects, many studies suggested that the influence of ligament size on the local yield strength of Au ($\sigma_{y,Au}$) used in Gibson-Ashby scaling law should be taken into account [12, 62-66]. According to that, a modified scaling equation proposed by Hodge *et al*. [65], where the $\sigma_{y,Au}$ exhibits a closed inverse square root dependence on ligament size, was used for predicting the yield strength of NPG.

The mechanism of plastic size effects mentioned above was explored by experiments [55, 57] and computation [39, 67-69] in the literature. It is unclear if the strain gradient due to the bending of the Au ligaments could lead to the size effects observed in NPG during deformation. In the absence of strain gradients, the strain gradient theory associated with geometrically

necessary dislocations [54] fails to interpret this phenomena. Currently, there exists two main mechanisms that are considered as the origin of the size-dependent behavior. One is the dislocation starvation hardening model that was proposed in many studies [45, 48, 57, 70, 71] (also called dislocation source-limited mechanism in [57]). In this scenario, the reduction of sample size to the submicron range leads to a decrease of distance for dislocation motion before they reach the sample surface where they dissolve. In this case, dislocations escape from pillars at the nearest free surface more quickly than they multiply and interact with other dislocations during deformation, which results in the decrease of dislocation density. Therefore, more external load must be applied on pillars in order to nucleate or activate new dislocation sources for plastic deformation. This mechanism has been verified by transmission electron microscopic (TEM) images of deformed Au nanopillars, where the elimination of defects in the course of deformation was found [55]. Additionally, the experimental observation of the pronounced decrease in dislocation density of a Ni crystal during nanocompression *in situ* in TEM also provided support for this model [47].

Another competing model, source-truncation hardening, where dislocations are not starved, which was first introduced basing on some simulation studies, is related to the size of dislocations sources [67, 72-75]. In this description, with the reduction of the sample dimension, the sample size becomes close to the average dislocation source length, usually resulting in, for instance, the double-pinned Frank-Read sources being truncated into single-arm sources due to the interaction with nearby the surface. The stress required to activate these single-arm dislocation sources was found to increase with decreasing source length. Therefore, the flow stress needed for the plastic deformation of smaller volume is higher. Recent *in situ* TEM mechanical testing of a submicrometer Al single crystal, where the single-end sources with the equivalent source length limited approximately by half of the crystal width were observed, provided experimental proof for this source truncation model [76]. Furthermore, the results of the operation of spiral dislocation sources at high stresses and the hardening by a gradual loss of defects during quantitative *in situ* TEM tensile testing of 100~200 nm thin Cu single crystal suggested that both mechanisms of dislocation starvation and source truncation should be taken into account simultaneously for explanation of the size effect phenomena [77].

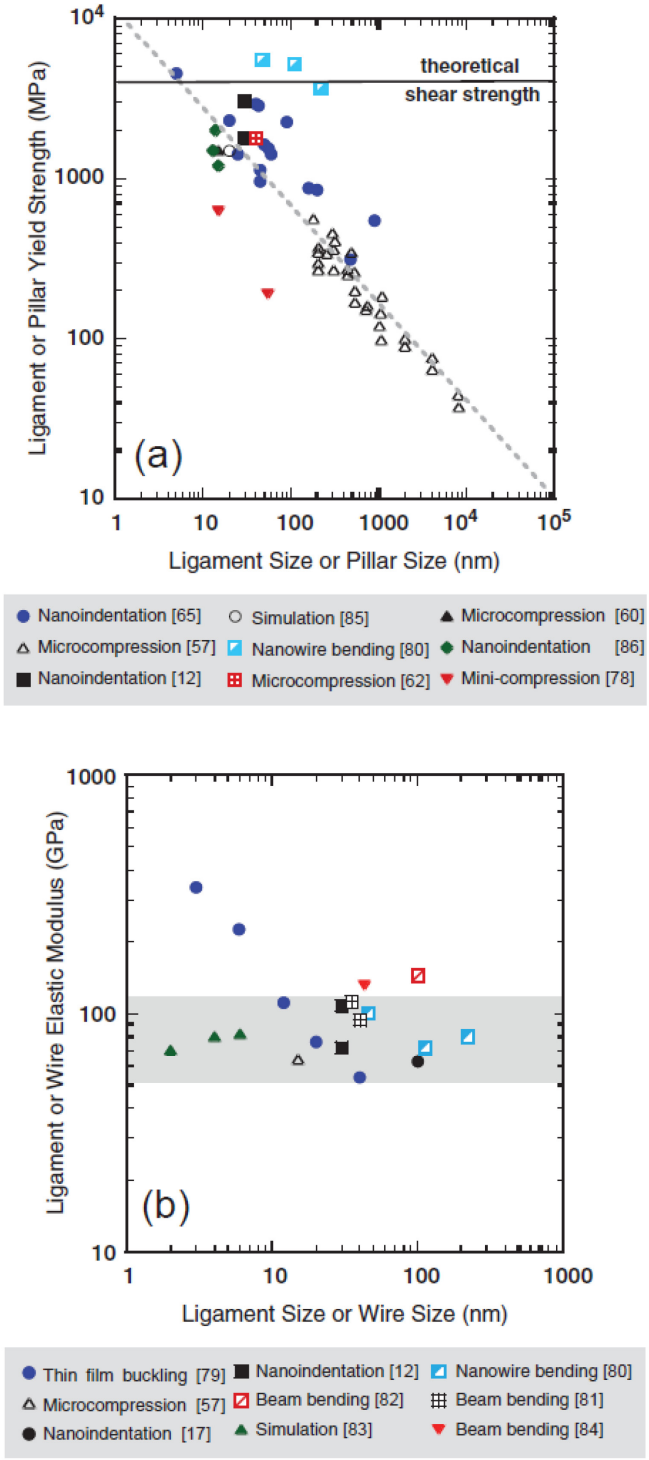

Figure 2.1. (a) Yield strength and (b) Elastic modulus as a function of ligament size of NPG or diameter of Au pillar selected from experimental data and simulation results in the literature [12, 17, 57, 60, 62, 65, 78-86]. Grey area in the middle of (a) denotes range of elastic modulus of single crystal Au in various crystallographic direction. In (b), the slid line represents theoretical shear strength of Au, and the dashed line is a power law with exponent of -0.6. Adopted from Ref. [35].

2.1.2.2 Elasticity

Similarly, a size-dependent elasticity of NPG for ligament sizes ranging from 20 nm to 500 nm has been observed in many experimental measurements [16, 79]. According to earlier theoretical calculations [87-90], the reduction of the sample size from the macroscale to nanoscale results in a considerable increase of specific surface area, which has influence on the elastic modulus. The contribution of surface factors associated with only a few layers of atoms near the surface or the volume occupied by the surface atoms, such as surface roughness, surface tension, surface stress and surface excess elasticity, play an important role in the overall elasticity.

However, the experimental results regarding size effect on elasticity of massive metals is contradictory. With sample size decreasing, some testing data showed an increase in stiffness of Ag nanowires [91-93] and Pd nano-whiskers [94], due to the effects of surface tension, while others found an enhanced compliance on Si [95] and chromium cantilevers [96]. Besides, some studies revealed that the elastic modulus is not sensitive to the sample size [80, 97-99]. In the case of Au, elastic modulus as a function of sample size measured by different methods is displayed in Figure 2.1 (b) [35]. Micromechanical testing [80] of Au nanowires showed that the Young's modulus exhibits independence on sample dimensions and it is close to the values (~78 GPa) reported for bulk Au when the nanowire diameter is larger than 40 nm. The atomic simulation of Au nanowires indicated a size dependence of the elastic modulus if the thickness of wires is less than 3 nm [100]. Recently, it was found that the surface excess elasticity can induce a weak decrease of the stiffness of Au nanowires in various deformation modes as the sample size decreases, but this decrease is only a few percent even for the diameter of nanowire as small as 10 nm [101]. Therefore, weak variation of elastic modulus caused by the reduction of ligaments size fails to interpret the size-dependent elasticity found in NPG in some studies.

2.1.3 Effects of structural geometry

Apart from size effects, the influence of structural geometry on the mechanical response has been investigated based on the random three-dimensional ligament network [16, 102-104]. Numerical models developed by Huber [105] and Roschning [106] revealed that structural disorder (degree of randomization of network) played a key role in determining Poisson's ratio, Young's modulus and yield strength of NPG, and they revisit the scaling equations by taking into account this factor. In addition, the influence of morphology characteristics, including ligament size and length distribution, ligament junctions, interfacial shape distributions and structural anisotropy, as well as topological features characterized by the scaled connectivity

density (also called scaled genus density in some literature), were found critical. A phenomenological model based on SEM images of NPG proposed by Pia *et al*. [19], provides a description of the relationship between morphological features (the ligaments and nodes in terms of characteristic lengths) and elastic response. Yet, some studies suggested that the stiffness and strength of NPG shows more dependence on topological connectivity than morphological features, through quantitative analysis and comparison of a series of nanoporous structures with different geometry as well as their mechanical behavior [107, 108].

Furthermore, regarding the phenomenon that the yield strength and elastic modulus of NPG measured by experiments are still lower than the corresponding values predicted by the Gibson-Ashby scaling law, even though considering the size effects [78, 109, 110], a concept of effective relative density or load-bearing solid fraction related to the connectivity (defined as the number of continuous tunnels or "handles" in the structure [111, 112]) was proposed by Liu *et al.* [18, 113] and Hu *et al*. [114, 115]. For a NPG network structure, a 2D skeleton schematic graph of which is shown in Figure 2.2 (a) [115], only the interconnected ligaments (belonging to closed rings, denoted by red lines and cyan nodes in Figure 2.2 (a)), which contribute to the connectivity of the network, bear the external load during deformation, while the floating and dangling ligaments (represented by black lines and blue nodes in Figure 2.2 (a)) do not contribute to the mechanics of the nanoporous structure. Thus, the solid fraction used for the scaling laws is the effective relative density only consisting of the ligaments contributes to the closed rings, i.e. load-bearing units, rather than the total relative density. The agreement between the mechanical measurements and predictions of scaling equations using the relative density of load-bearing units obtained by skeletonization analysis, as shown in Figure 2.2(b) [114], and experimental testing [18] confirmed the validity of this suggestion. Recently, scaling relations for the change of Young's modulus and Poisson's ratio was developed, basing on a NPG model generated by Cahn's method of levelled Gaussian random fields, where the variation in the topological genus is considered, exhibits consistent with the experimental data, which further verify the importance of topology in mechanical properties of nanoporous materials [116].

Apparently, ligaments are the smallest elements of a nanoporous structure, but the transition of mechanical behavior from single nanoscaled ligaments to the overall network, is done via the load-bearing units that are significantly softer and more compliant than single ligaments. It is expected that the load-bearing units, which are generally larger than the single

ligaments, determine the mechanical behavior of NPG, but an exact and appropriate quantification of these load-bearing rings is still not established.

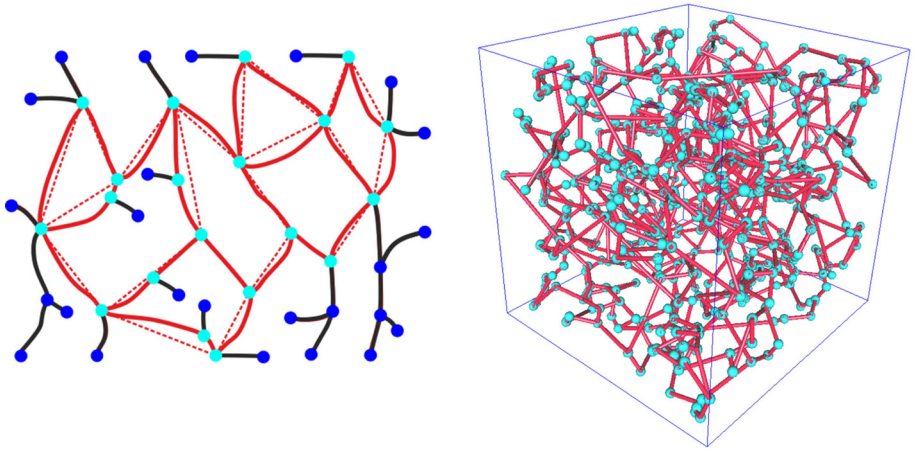

Figure 2.2. (a) 2D schematic graph of a NPG skeleton structure, the fully interconnected load-bearing ring skeletons are shown in red lines and the dangling branches is in black. The nodes that belong to the ring structure and to the dangling ligaments are shown in cyan and blue, respectively. The red dashed line denotes the Euclidean distance between the cyan nodes. (b) Skeletonization of a 3D reconstruction RV of the NPG network with a fully interconnected ring structure. The nodes are shown in cyan, and the ligaments are shown in red [115].

2.2 Metals surface modified by electrochemical potential

2.2.1 Metal-electrolyte interface

When a metal is introduced into an aqueous electrochemical environment, the electrons of the metal, as well as the ions in the solution near the metal-electrolyte interface will rearrange, which generates an electrical field over the interface [117-119]. This rearrangement region, including the array of electrons and ions, is called the electric double layer. The thickness of the double layer at the metal side is very thin and less than 1Å, while the corresponding layer in the electrolyte is thicker, in the range between 5 and 20 Å [120]. A model of the double-layer region is illustrated in Figure 2.3 [119]. In this model, there is an excess of electrons in a thin layer underneath the metal surface while the solution side of the double-layer region is more complicated, consisting of several layers. The layer closest the interface, called the Helmholtz or Stern layer, contains solvent molecules, and ions specifically adsorbed on the metal surface, commonly observed with weakly solvated anions because they can escape from the solvation

shells and form chemical bond with the metal [121]. The locus of the electrical centers of these specifically adsorbed ions is called the inner Helmholtz plane (IHP). Outside this layer, some solvated cations with strongly bound solvation shells, surrounded by polarized water molecules that screen the fields originating from the ions, have electrostatic interaction with the charged metal surface [122]. The locus of the centers of cations is called the outer Helmholtz plane (OHP). The region between the OHP and the bulk of the solution is a diffuse layer. The organization of the ions close to the surface determines the distribution of potential as a function of distance from the interface.

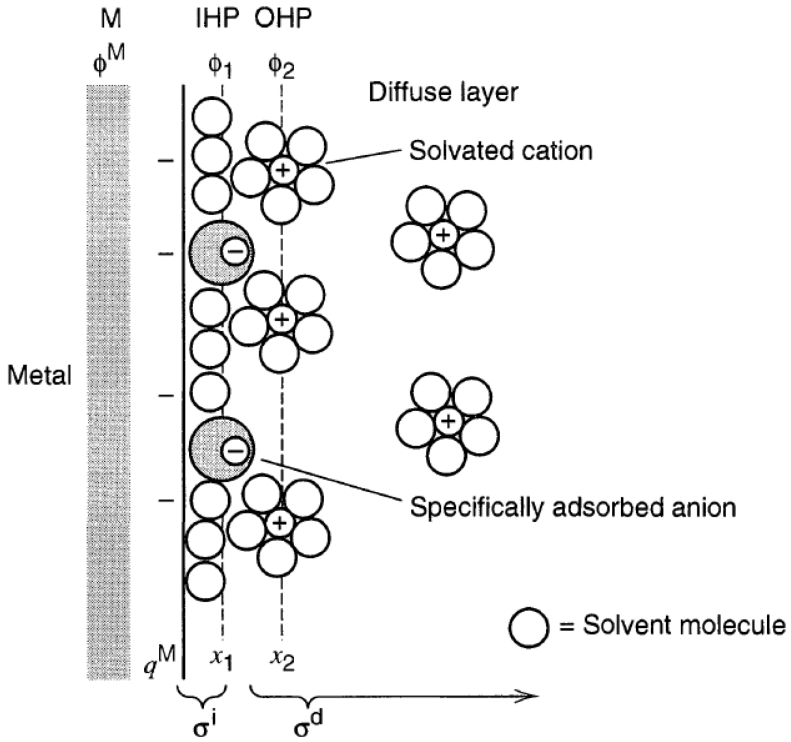

Figure 2.3. A model of electrical double-layer region under conditions where the anions are specifically absorbed [119]. IHP: inner Helmholtz plane. OHP: outer Helmholtz plane.

It turned out that the metal-electrolyte surface behave like a capacitor. In the case of clean metal surface in contact with aqueous electrolyte, the capacitance of the double-layer region is typically in the range of 10 to 40 μF/cm^2 [119]. Application of potentials on the metals can produce the accumulation of charges on the metals surface, causing the change of ions distribution in the interfacial region. The charges on the metal surface can be positive or negative, leading to the attraction of anions or cations in the electrolyte [117]. The charge

density of the electric double layer can be tuned if a varying potentials are imposed, resulting in small nonfaradic currents.

If the applied potential with respect to the reference electrode is sufficiently positive and reaching or exceeding the critical potential of oxidation, the oxidation reactions occur accompanied by electrons transferring across the metal-electrolyte interface, producing faradic currents considerably higher than that in the capacitive region. Inversely, a sufficient negative potential can generate the reduction reactions. The onset potential for oxidation or reduction depends on the metal and its surrounding electrochemical environments

2.2.2 Electrochemical oxidation adsorption on Au surface

If a positive potential is imposed on a noble metal, such as Pt or Au, which is immersed in an electrolyte, such as $HClO_4$, H_2SO_4, or NaF aqueous solution, the oxidation and reduction taking place at the metal-electrolyte interface, are typically referring to the adsorption and desorption of oxide film on the metal surface, respectively [123, 124].

In the case of Au, the formation of the oxide monolayer consists of several stages, including sub-monolayer formation, reconstruction and growth of oxide film [22, 125-127]. At the beginning, the first sub lattices of monolayer (two-dimensional OH arrays) is generated in between anions specifically adsorbed, during which place-exchange occurs between the adsorbed OH species on the surface, and Au atoms within the surface lattice. It is followed by a reconstruction process, i.e. a turn-over process, where the position of AuOH dipoles change from parallel to antiparallel orientation, and the development of OH layer accompanied by the desorption of other anions until the three-dimensional oxide monolayer on Au surface was completed. The oxide monolayer formed on the Au surface is the state of the chemical occupancy of the lattice, rather than stoichiometric phase compounds. Subsequently, if the applied potential decreases to the capacitive region, the oxide monolayer will move away from the Au surface, after the interface changes back to the electrical double-layer state. Hence, the surface state of Au can be changed reversibly between surface electrosorption and double-layer state in a potentials-sweep by changing the potential in time, or the same state of oxide formation be attained by holding the electrode at a suitable potential for an appropriate length of time. The information regarding the oxidation adsorption and desorption can be obtained by cyclic voltammogram (CV) measurement.

The formation of an oxide monolayer, especially the initial formation of 2-dimenonal OH arrays, on the Au surface is affected by the anion species of the electrolyte, which are pre-adsorbed on the surface before oxidation occurs, such as Cl^-, $HClO_4^-$ and SO_4^{2-}. Due to existence

of competition, these anions can inhibit the onset of the first stage of surface oxidation, which has been confirmed in many experiments on single-crystal Au surface [128, 129].

2.2.3 Influence of electrode potential on surface tension and surface stress

Compared to the interior atoms, the atoms on the surface show considerably different interatomic interaction due to the absence of constraints from the neighboring atoms [130], which leads to a redistribution of the atoms on, or near the surface [131]. The equilibrium condition for surface atoms is modified with respect to the bulk, resulting in an excess energy of the surface. Therefore, increasing of surface area requires to overcome the energy difference. The surface area of a solid can be extended by two different modes. One is plastic deformation, where the surface area increases by adding surface atoms at constant strain, e.g. division, during which, the atomic structure of the surface remains identical. The other is elastic strain, where the variation in surface area is achieved by changing the interatomic distance at constant number of atoms, e.g. elastic stretching. Surface tension and surface stress are two concepts related to these two different physical processes [132, 133].

Surface tension (γ) is defined for a one-component system as the excess free energy per area required form a new surface at constant structure [132, 133], where the chemical potential (μ_i), temperature (T) and elastic strain ($\boldsymbol{\varepsilon}$) is constant:

$$\gamma = \left(\frac{\partial F}{\partial A_s}\right)_{\mu_i, T, \boldsymbol{\varepsilon}} \tag{2.1}$$

where ∂F is the variation in excess free energy, ∂A_s is the variation in surface area, and $\boldsymbol{\varepsilon}$ is the tangential strain tensor at the surface. The surface tension is a scalar quantity representing the excess free energy per unit area owing to the existence of a surface.

In contrast, the surface stress ($\mathbf{s}$) is associated with the work spent in elastically stretching an existing surface of a solid [134, 135]. According to Shuttleworth, $\mathbf{s}$ is given by:

$$\mathbf{s} = \gamma \mathbf{I} + \frac{\partial \gamma}{\partial \boldsymbol{\varepsilon}} \tag{2.2}$$

Since the $\mathbf{s}$ is dependent on the direction of the straining, $\mathbf{s}$ is a second-rank tensor. $\mathbf{I}$ is the second-order identity tensor, and γ represents the surface free energy per unit area (surface tension) of the strained surface.

In addition, equation 2.2 is equivalent to a simpler form introduced by Cahn [136] using Lagrangian coordinates that defined relative to crystal coordinates, where the surface area is

measured in the undeformed state, thus $\partial A_s = 0$. The surface stress ($\mathbf{s}^{\mathrm{L}}$) in Lagrangian coordinates then results in the strain derivative of the surface tension:

$$\mathbf{s}^{\mathrm{L}} = \frac{\partial \gamma^{\mathrm{L}}}{\partial \boldsymbol{\varepsilon}} \tag{2.3}$$

Equation 2.3 emphasizes that the value γ^{L} of the function and its derivative $\mathbf{s}^{\mathrm{L}}$ are thermodynamic parameters with fundamentally different meaning which can take on independent numerical values [135].

In the case of isotropic straining and high symmetry surfaces, we can use a scalar surface stress, f, which is associated with half the trace of the surface stress tensor $\mathbf{s}$ ($f = \frac{1}{2}tr(\mathbf{s})$), for conciseness [135].

If a polarizable solid electrode is immersed in an aqueous electrolyte and charged by potentials, the response of surface tension to the changes in the electrode potential (dE) can be described by the Lippmann equation at constant T, μ_i, and $\boldsymbol{\varepsilon}$ [133, 137, 138]:

$$(\frac{d\gamma}{dE})_{\mu_i,T,\boldsymbol{\varepsilon}} = -q \tag{2.4}$$

Considering the capacitance of the double-layer ($\mathrm{c} = dq/dE$) is potential-independent, the variation of surface tension $\Delta\gamma$ shows parabolic dependence on the charge density (q) during capacitive charging, as shown by the results of cantilever-bending experiments with an Au electrode in 7 mM aqueous NaF in Fig 2.4 [137]. It is seen that the maximum value of surface tension is at the potential of zero charge (pzc).

$$\gamma - \gamma_{pzc} = \Delta\gamma = \frac{1}{2}c\big(E - E_{pzc}\big) = -\frac{1}{2}\frac{q^2}{c} \tag{2.5}$$

In contract to the surface tension, surface stress, f, exhibits linear dependence on the surface charge near the pzc. The variation of surface stress with the charge density is given by:

$$\varsigma = (\frac{df}{dq})_{\mu_i,T,\boldsymbol{\varepsilon}} \tag{2.6}$$

$$f - f_{pzc} = \Delta f = \varsigma q \tag{2.7}$$

Where ς is a electrocapillary coupling coefficient.

Based on the results shown in Figure 2.4 [137], it can be found that the amount of variation in f is much larger than the corresponding amount of variation in γ, and the value of the electrocapillary coupling coefficient ς in Figure 2.4 is $-1.95 \pm 0.1\ V$.

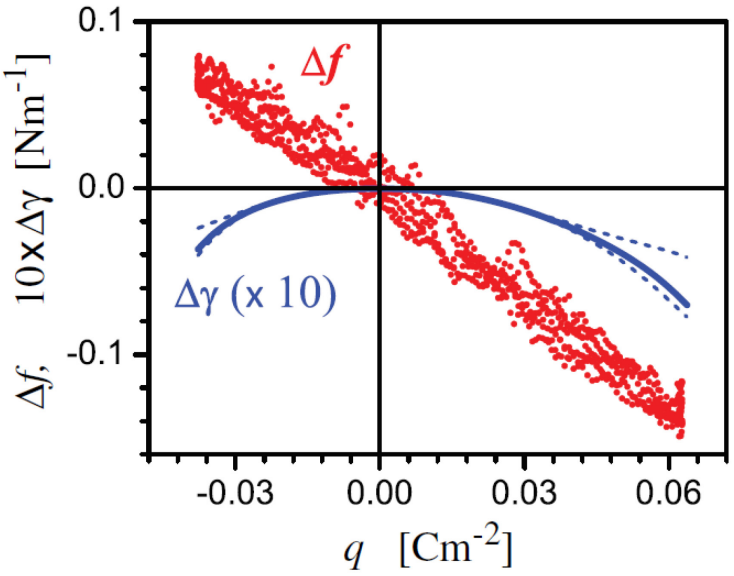

Figure 2.4. Variation of the surface stress, f (red dots), and surface tension, γ (blue solid line, data multiplied by 10 for better readability), with superficial charge density q during the potential scans, measured from a cantilever-bending experiment with a gold electrode in aqueous NaF (7mM). The parameter γ is computed from the voltammogram data using Lippmanns equation, while f results from the curvature data and Stoneys equation. The blue dashed lines shows the estimated error in integration of Lippmanns equation [137].

2.3 The influence of surface states on properties of nanoporous materials

As mentioned in 2.2.3, the energy of surface atoms is higher than the energy of interior atoms since the surface atoms have fewer neighboring atoms, as shown in Figure 2.5 (a) [130]. Even though the structure of the surface is different from the internal structure, the influence of the surface on the overall properties of a solid is typically weak, since the ratio of the number of surface atoms to the total number of atoms is generally considerably low. However, the percentage of surface atoms increases significantly as the sample size decreases to nanoscaled [130]. As shown in Figure 2.5 (b), the percentage of surface atoms reach to 20% when the diameter of nanowire is less than 10 nm. Hence, nanomaterials, such as nanoparticles, nanowires, as well as cellular ceramics and nanoporous metals composed of nanoscaled struts, show a quite high ratio of surface area to volume or mass. For example, the specific surface area of NPG with ligament size of 10-20 nm made by dealloying reaches 10-15 m^2g^{-1}, which is 3~5 × 10^5 times larger than the bulk solid gold with a size of millimeter-scale [139, 140].

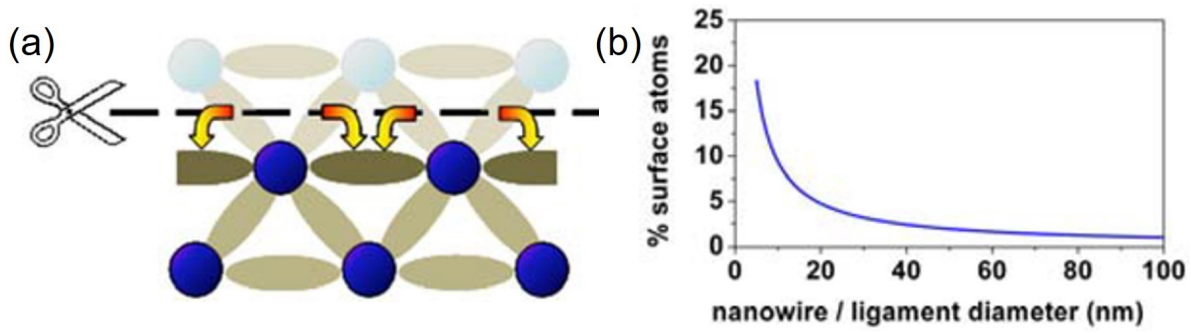

Figure 2.5. (a) Schematic diagram of the surface atoms with the absence of constraints from neighboring atoms. (b) Percentage of surface atoms as a function of nanowire diameter [130].

For nanomaterials with high specific surface area, the contribution of surface can not be ignored and sometimes it plays a dominant role in the overall properties of materials [141-143]. It was found that many nanoporous materials exhibit interesting behaviors controlled by surface of interface modification [1, 144]. The surface state can be changed irreversibly by depositing a thin film of the second material on the struts surface [145, 146], or controlled reversibly using elctrochemical method when the surface is exposed in a electrolyte, as mentioned in the last section. Both of them play significant roles for optimizing the properties of nanoporous metals. In this section, we are focusing on the influence of surface state on the functional and mechanical responses of nanoporous metals.

2.3.1 Functional behavior

It was found that reversible strain of NPG was measured when the sample was alternately exposed to ozone and carbon monoxide atmosphere where the surface can be switched between the oxygen-covered and clean states [139]. In addition, when nanoporous metals, such as NP Pt, NP Pd and NP Au, are immersed in an electrochemical environment, the surface condition of samples can be changed, such as from clean to adsorption state, by applying a varying potential [2, 147-151]. In this case, the sample undergoes isotropic expansion and contraction as potential varies in a certain range. The amplitude of potential-driven strain is around 0.3%~1% mainly dependent on the ligament size. The dimension change of NPG under electrochemical potentials, as displayed in Figure 2.6 (a), indicated that the actuation response is reversible [2, 152]. Moreover, the sign of dimension change of NPG in response to the oxygen adsorption was found to be dependent on the external load [153]: increasing load can lead to a significant decrease in the amount of actuation and even inverting of its direction. This functional behavior chemically or electrochemically controlled by surface state is resulting from the variation of capillary force, here the surface stress [152, 154-156]. The surface stress of a solid tuned by the

surface state can modify the compensating bulk stress, resulting in a dimension change throughout the bulk when the specific surface area of the sample is large.

The change of surface stress of NPG in an electrolyte is not only able to convert the electrochemical energy into a mechanical energy, but also to convert mechanical energy into electric energy. As shown in Figure 2.6 (b) [3], an application of cyclic strain on NPG immersed in an electrolyte causes a measurable variation of voltage (at constant charge) or current (at constant potential). This behavior gives NPG a new property, piezoelectricity, a phenomenon usually found on ceramic materials. Additionally, NPG shows a great catalytic activity for methanol electrooxidation [157].

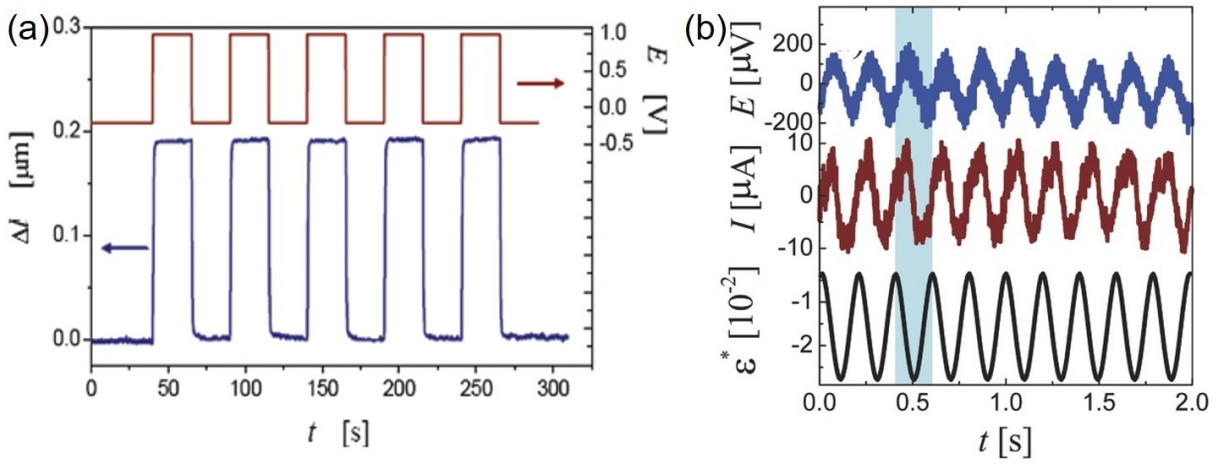

Figure 2.6. Functional behaviors of NPG with a ligament size of 20 nm in an electrochemical environment. (a) Dimension change of NPG under potential jumps in 50 mM H_2SO_4 solution [2, 152]. (b) Oscilloscope traces of potential (blue) and current (red) modulation due to a cyclic strain (black) at a frequency of 5 Hz [3].

2.3.2 Mechanical behavior

The influence of the surface state is not limited to the functional performance, but also affects the mechanical behavior, which has been attracted much attention since 1940s [158-163]. Environmental effects, such as hydrogen embrittlement and stress corrosion cracking, have been observed on conventional metals in many investigations [27, 164]. The early studies done by Rehbinder and his associates, have shown that the plastic behavior of nanocrystals are sensitive to the surface states [158, 165]. When a metal is exposure to liquids with surface-active substance, the adsorption occurring on metal surface will cause a decrease in yield stress and rate of work-hardening (called “Rehbinder effect”), which is associated with the decrease

in surface energy accompanying surface adsorption. This would facilitate the escape of dislocations from crystals and the growth of surface microcracks during deformation [158]. Additionally, it was found that the anodic or cathodic polarization exhibits significant influence on creep behavior of gold wire, depending on the composition, oxygen content and pH of the solutions [166, 167].

In the case of nanoporous metals, especially NPG, the effect of surface on elastic and plastic response becomes notable because of their high specific surface area. It was turned out that the dynamic fracture behavior of NPG showed dependence on the electrode potential [168]. Increasing electrochemical potential in the double-layer region can increase the creep rate of NPG, while the presence of oxygen adsorption does the opposite: weakening the creep rate [169]. Apart from that, the effective stiffness increased by ca.10% if the surface of ligaments is charged in an electrolyte and covered by an oxide monolayer, owing to the contribution of surface excess elasticity [23].

The most impressing is the influence of the surface state on the effective mechanical strength of NPG. An improvement of strength and hardness up to 50% caused by surface modification with self-assembled monolayers was observed [170]. In other studies, plastic behavior of NPG is sensitive to the electrochemical potentials. It was found that flow stress can be modulated by potential jumps within the regime of capacitive charging [171]. Moreover, the variation of strength is more noticeable when the applied potential is sufficiently positive to generate oxidation adsorption on surface [24, 171, 172]. As the compressive stress-strain curve of NPG measured in 1 M $HClO_4$ shown in Figure 2.7 [24], the flow stress was simply tuned by applying potential jumps where the two potentials refers to double-layer surface state and oxidation adsorption , and this modification is reversible which was not found in conventional metals. In particular, the strength can be doubled by surface adsorption at the strain of around 0.4, while the extent of the increase in flow stress is dependent on the ligament size [172].

A recent study [171] suggested that the effect of surface tension (i.e. specific surface excess energy), rather than surface stress, dictated the variation of flow stress under potentials control in the capacitive region. Yet much debate remains regarding the mechanisms that couple plasticity and electrochemical surface adsorption on NPG. Two possible mechanisms might contribute to the improvement of the strength [24, 159, 160]. One hypothesis, proposed based on the plastic behavior of ionic crystals affected by environments, is associated with the variation of surface tension [160]. Potential changes from capacitive to OH adsorption region can cause a significant decrease in surface tension of NPG, which has been found in many

studies [135, 171]. Since the cross-gliding of the screw dislocations during plastic deformation is opposed by the surface energy of the step created via dislocation motion, the reduction of the surface tension induced by potential variation promotes cross-slip, resulting in dislocation multiplication and producing pinning points hindering dislocation movement, consequently, leading to an increase in flow stress [160, 173]. Another possible scenario is the "adsorption locking" mechanism [24, 159]. The adsorption species induced by potential have an impact on the elastic interaction of dislocations near the surface. During plastic deformation, the adsorbates bonded to the ligament surface are likely to block the subsequent motion of dislocations via pinning the dislocation's endpoints at the surface, resulting in strengthening materials [159, 167, 174]. This effect is similar to the effect of Cottrell clouds observed in conventional solid solutions.

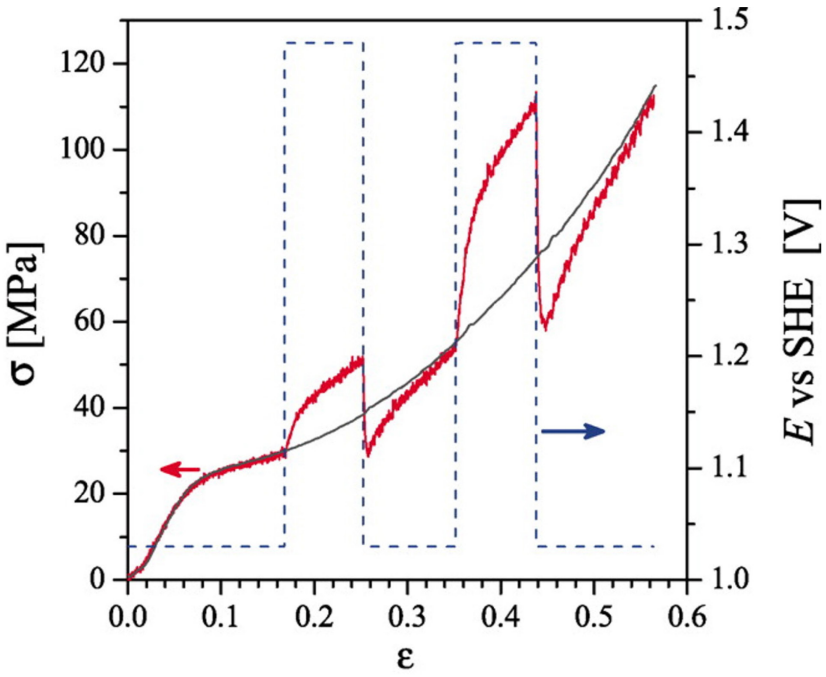

Figure 2.7. Compressive stress-strain curve (red) of bulk NPG with ligament size of 20 nm under potential jumps control in 1M $HClO_4$ aqueous solution, where 1.03 V and 1.48 V refer to clean and OH-covered surface state, respectively. Another stress-strain curve (black) measured at constant potential of 1.03V plotted for comparison [24].

Most of experiments focused on mechanical properties coupled with the electrochemical potentials were carried out at the macroscale, while a better understanding of underlying mechanism requires the corresponding testing at the microscale since the surface variation occurs on the nanoscaled ligaments surface. Additionally, effects of microstructure aspects on

the electro-chemo-mechanical coupling are unclear, which can be investigated with the assistance of *in situ* micromechanical experiments.

3 Sample preparation and methods

3.1 Electrochemical systems and potential control

3.1.1 Electrochemical cells

The three-electrode electrochemical cells, where the interested reactions occur on the interface between electrodes and electrolyte, were utilized in this thesis for nanoporous gold (NPG) fabrication and to modify the surface state of the sample during *in situ* micromechanical testing. All the cells were manufactured out of chemically inert materials, available for a wide range of aqueous solutions. Three electrodes: working electrode (WE), counter electrode (CE) and reference electrode (RE) were immersed in the electrolyte during electrochemical experiments. The schematic diagram of an electrochemical cell for the dealloying is shown in Figure 3.1.

Different types of electrolyte were chosen here for experiments according to different purposes. 1M $HClO_4$, prepared by diluting a standard high concentrated $HClO_4$ (Merck, Alfa Aesar) with ultrapure water (Ultra Clear TWF UV TM, Siemens), was used for NPG fabrication (dealloying and the subsequent reduction). In addition, the electrolyte for *in situ* micromechanical testing is 0.5 M NaF that is made from NaF powder (Merck) and ultrapure water, in order to minimize potential damage to the nanoindentation system.

Our samples, where the electrochemical event of interest occurs, serve as WE in the electrochemical systems. For instance, the WE for dealloying and electro-chemo-mechanical measurement are master alloy $Au_{25}Ag_{75}$ and NPG, respectively. During experiments, the potential of WE that we applied is with respect to the potential of RE that should be made of materials with fixed and stable potentials. The RE used for NPG fabrication is custom-made Ag/AgCl electrode. It is prepared by electrolytic coating of AgCl on a Ag wire (WE, Ag ≥ 99.99%, Alfa Asesar) with diameter of 0.5 mm in 1M HCl, where a constant potential of 0.95 V with respect to another coiled Ag wire (serving as CE and RE) was applied on the WE for 2 minutes. For *in situ* testing, a commercial Ag/AgCl electrode with 2 mm diameter (Driref-2, World Precision Instruments) was selected as RE, since its size was fit for the corresponding electrochemical cell. Both of REs were calibrated by Standard hydrogen electrode (SHE,

Gaskatel) or Saturated calomel electrode (SCE, Radiometer analytical) before use, in order to make sure the accuracy and stability. The CE, where the electric current flows, should be inert and its surface area is generally larger than the surface area of the WE. In order to avoid the reactions generated at the CE interfering with the reactions occurring at the WE we are interested in, polarizable electrodes, behaving like capacitors, where there is no charge crossing electrode-electrolyte interface when a current is applied, are general used as CE. In the current work, Ag coil (Ag ≥ 99.99%, Alfa Asesar) and carbon net (Kynol Europa GmbH) served as CE for dealloying and reduction, respectively, while platinum (Pt) wire (Pt ≥ 99.9%, Sigma-Alorich) was chosen for *in situ* testing because its size is fit for the electrochemical cell. All the electrochemical experiments in this thesis were performed at room temperature and three electrodes described above were connected to a high-performance potentiostat (PG-STAT 302N, Metrohm AUTOLAB) through which the potential and current can be controlled and recorded by NOVA software (Metrohm).

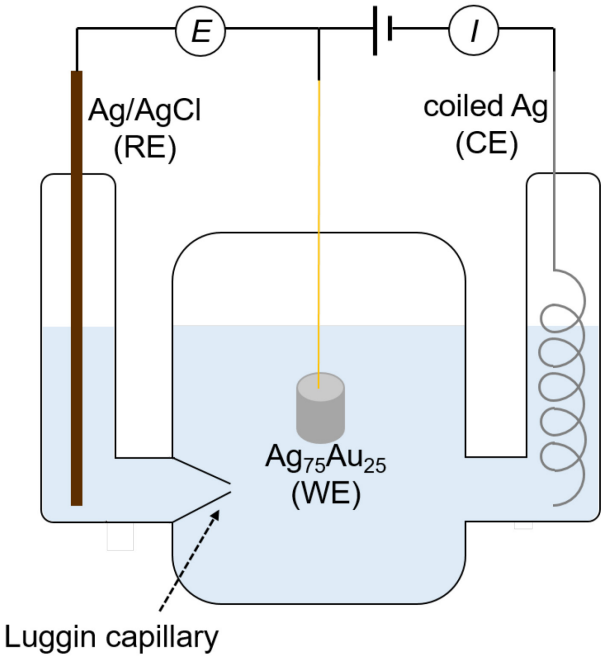

Figure 3.1. Schematic diagram of a three-electrode electrochemical cell for dealloying. WE: working electrode ($Ag_{75}Au_{25}$); RE: reference electrode (Ag/AgCl); CE: counter electrode (coiled Ag).

3.1.2 Electrochemical methods

3.1.2.1 Cyclic voltammetry

Cyclic voltammetry (CV) is a technique used for studying and characterizing the oxidation and reduction processes of an electrochemical system. During CV measurement, the current of an electrochemical circuit is recorded while the electrode potential of WE against RE is changing cyclically between two preset potentials at a constant scan rate. The reactions occurring on WE induced by the variation of potentials can be reflected by the current-potential curves (CV curves). A CV curve of NPG with ligament size of 35 nm in 0.5 M NaF, where potential varied with a rate of 5 mV/s is illustrated in Figure 3.2. The potential imposed on NPG started with open circuit potential (OCP), increasing to 1.4 V, then decreasing to -0.2 V, finally coming back to the starting point. All electrode potentials mentioned in this paper are specified versus standard hydrogen electrode (SHE). The most significant features of CV curves of NPG were two peaks where the surface state changed reversibly: OH adsorption peak associated with the formation of an OH monolayer at positive potential, and desorption peak, i.e. the stripping of that monolayer, at negative potential. The region after monolayer desorption is called capacitive region where an electric double-layer is formed on the interface of gold and electrolyte. Basing on that, the potential window of adsorption and desorption of NPG is recorded, through which we are able to change the surface states by selecting appropriate potentials.

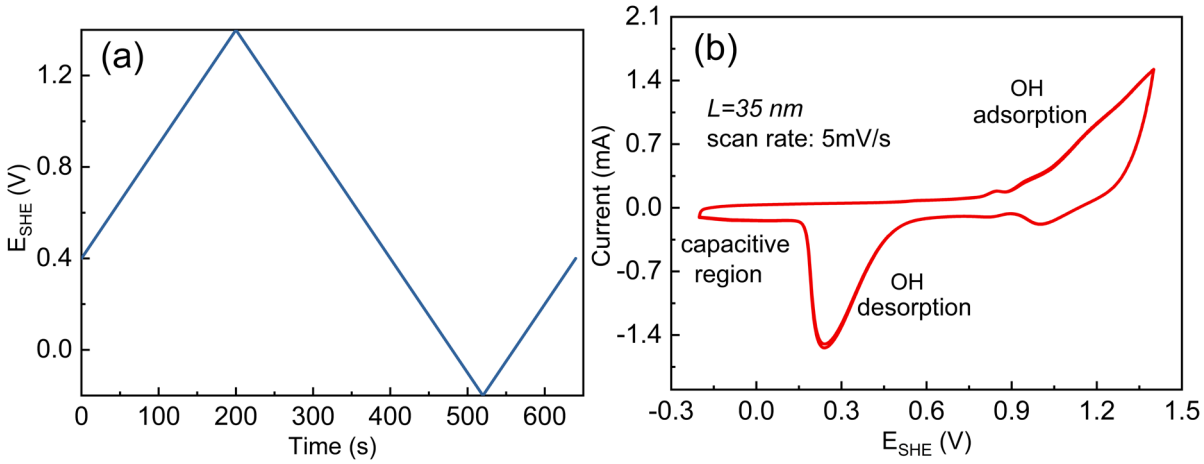

Figure 3.2. Cyclic voltammogram (CV) measurement of NPG at room temperature in the small electrochemical cell used for *in situ* mechanical testing. (a) Potential (E_{SHE}) waveform with the scan rate of 5 mV/s, starting with 0.4V; the lowest potential and the highest potential are -0.2 and 1.4 V, respectively. (b) CV curve of NPG with ligament size of 35 nm measured in 0.5 M NaF using the cell for electro-chemo-mechanical coupling testing.

3.1.2.2 Chronoamperometry

Chronoamperometry is an electrochemical method by which a constant potential or potential jumps can be applied on the WE, and the inducing current as a function of time is recorded. The current shows exponential decay with time, as shown in Figure 3. 3. In the current work, chronamperometry was used for dealloying, during which a constant potential of 1.25 V is applied on a master alloy ($Ag_{75}Au_{25}$, WE) in order to remove the Ag element and generate nanoporous network structure. Apart from that, potential jumps consisting of -0.2 V and 1.4 V, where these two potentials are selected according to the CV curve shown in Figure 3.2 (b) and refers to electric double-layer and OH adsorption state, respectively, were imposed on the NPG sample during *in situ* micro-mechanical testing, in order to change the surface conditions of NPG.

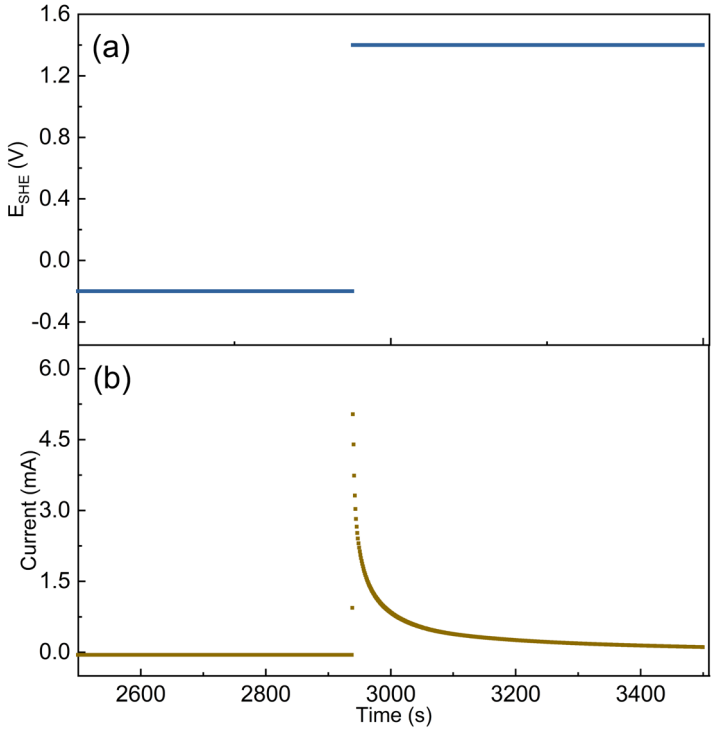

Figure 3.3. Potential jumps consisting of -0.2 V and 1.4 V applied on NPG samples via chronoamperometry during *in situ* micromechanical testing. (a) Potential versus time curve. (b) Variation of current under potential jumps.

3.2 Sample preparation

Three types of samples, bulk NPG with cylindrical and disc shapes, and NPG thin films are used in the current work. Cylindrical samples, which are easy to fix and move during fabrication, especially in the processes of mechanical polishing and dealloying, were used for

micromechanical testing in Chapter 4. In the case of *in situ* experiments, in order to minimize the actuation of the substrate and meet the testing requirements, which will be detailed in Chapter 5.2.2 and 6.1.1, respectively, disc-shaped samples and NPG thin films are used for micromechanical testing in an electrochemical environment in Chapter 5 and 6. In this section, the emphasis lies in the fabrication processes of these NPG samples.

3.2.1 Bulk NPG

3.2.1.1 Precursor alloy

The master alloy used for fabrication of bulk NPG in current work was a $Au_{25}Ag_{75}$ alloy, which was produced from Ag and Au wires (Ag ≥ 99.99%, Au ≥ 99.99%, Sigma-Aldrich) by arc melting (MAM-1 Edmund Bühler) under Ar atmosphere, followed by a homogenized annealing procedure at 850°C for 120 h in vacuum (customized furnace setup). The $Au_{25}Ag_{75}$ ingots were shaped into wires of 1 mm and 2.3 mm diameter via wire drawing, and then cut into cylindrical (diameter: 1 mm, height: 2 mm) and disc-shaped (diameter: 2.3 mm, thickness: 700 µm) samples, by a wire saw (Model 3032, Well Diamond Wire Saw). The schematics of these two samples are illustrated in Figure 3.4. Afterwards, the specimens underwent mechanical grinding and one-side polishing, using diamond pastes with consecutively decreasing particle size down to 3 µm. This process reduced the thickness of the disc-shaped samples to approximately 300 µm. In order to diminish the residual stress, samples were subsequently annealed at 800°C for 1h in Ar atmosphere (infrared furnace behr IRF 10, Labor Technik).

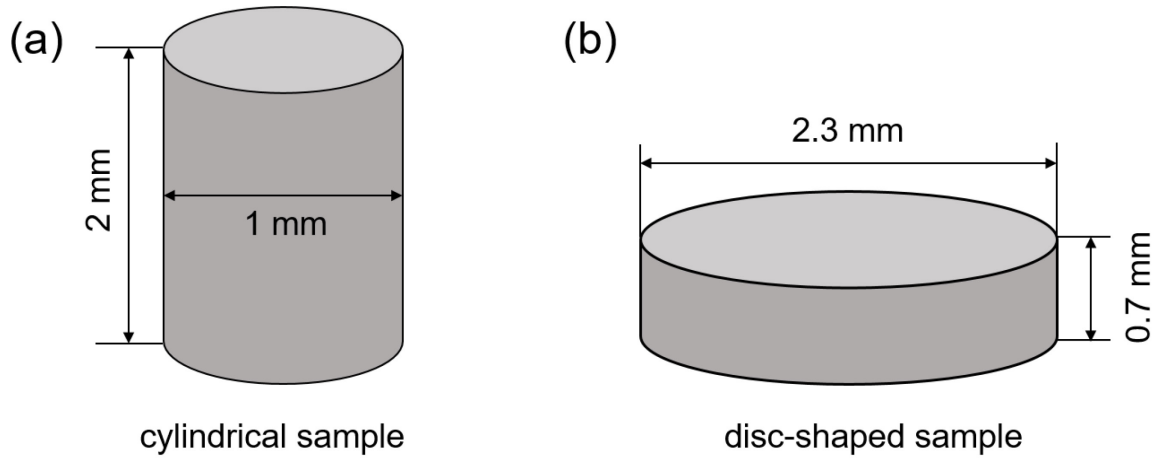

Figure 3.4. Schematics of (a) cylindrical (diameter: 1 mm, height: 2 mm) and (b) disc-shaped (diameter: 2.3 mm, thickness: 700 µm) $Ag_{75}Au_{25}$ samples.

3.2.1.2 Electrochemical dealloying

Bulk $Au_{25}Ag_{75}$ master alloys, obtained from the preparation procedures described above, serving as WE, were dealloyed electrochemically in a three-electrode electrochemical cell, as shown in Figure 3.1. The electrolyte chosen here was 1M $HClO_4$ aqueous solution diluted from a standard high concentration $HClO_4$ (60%, Merck, Alfa Aesar) with ultrapure water (Ultra Clear TWF UV TM, Siemens). An Ag coil and a custom-made Ag/AgCl wire electrode (+0.505 V vs. SHE) served as CE and RE, respectively. During dealloying, a constant potential of 1.25 V was applied on samples, which induced dissolution of Ag in the electrolyte, resulting in formation of the nanoporous network structure. The dealloying process was stopped when the current decreased to a value lower than 10 μA. This process lasted several hours for both of these two samples. After dealloying, the color of samples changed from silver to dark brown, indicating structured sizes below the wavelength of visible light. The samples were cleaned repeatedly using ultrapure water.

Although most of the Ag content has been dissolved in the electrolyte during dealloying, there are still approximately 10 at. % Ag left in samples after the first dealloying step. In order to remove the residual silver, samples after cleaning were transferred to another electrochemical cell which was filled with fresh 1M $HClO_4$ diluted from a higher concentration $HClO_4$ (70%, Merck, Alfa Aesar, super pure) for the reduction treatment. The CE and RE used for this process were carbon net and a custom-made Ag/AgCl electrode, respectively. A cyclic varying potential from 0 V to 1.5 V was imposed on NPG specimens for 15 successively cyclic scans at a scan rate of 5 mV/s. Finally, NPG specimens were cleaned by rinsing in ultrapure water, and were dried in air. The average of ligament size of cylindrical and disc-shaped NPG after fabrication is around 35 nm, which was measured by linear intercept method from scanning electron micrographs (SEM) images using ImagJ software. During measurement, four of straight lines were drawn though the SEM images, as shown in Figure 3.5 (a), and the number of ligament boundaries intersected by each line was counted. The average ligament size is obtained through dividing the number of intersections by the actual line length. There is no residual Ag content that can be detected by Energy-Dispersive X-ray spectroscopy (EDX) detectors equipped with SEM after NPG fabrication, indicating that the Ag residual in NPG after fabrication is below 0.1 wt. % what corresponds to the sensitivity of this machine.

3.2.1.3 Structure coarsening

The ligament structure of cylindrical and disc-shaped NPG samples can be adjusted from tens to thousands of nanometers by post-annealing, which has been confirmed in many works

[9, 12, 63]. During annealing, the porous structure coarsens via surface diffusion controlled by the temperature and time [175]. As mentioned above, the ligament size of as-dealloyed NPG is around 35nm. Here, NPG samples with larger ligament size of 50 nm, 200 nm and 350 nm were obtained by consecutive thermal annealing in a furnace (infrared furnace IRF 10, behr Labor Technik) at 300℃ for 12 min, 60 min, and 500℃ for 60 min in air, respectively. The SEM images of bulk NPG with ligament size of 35 and 350 nm are shown in Figure 3.5 (b) and (c). As can been seen, these two porous structures exhibit similar geometry characteristics, except for the feature size.

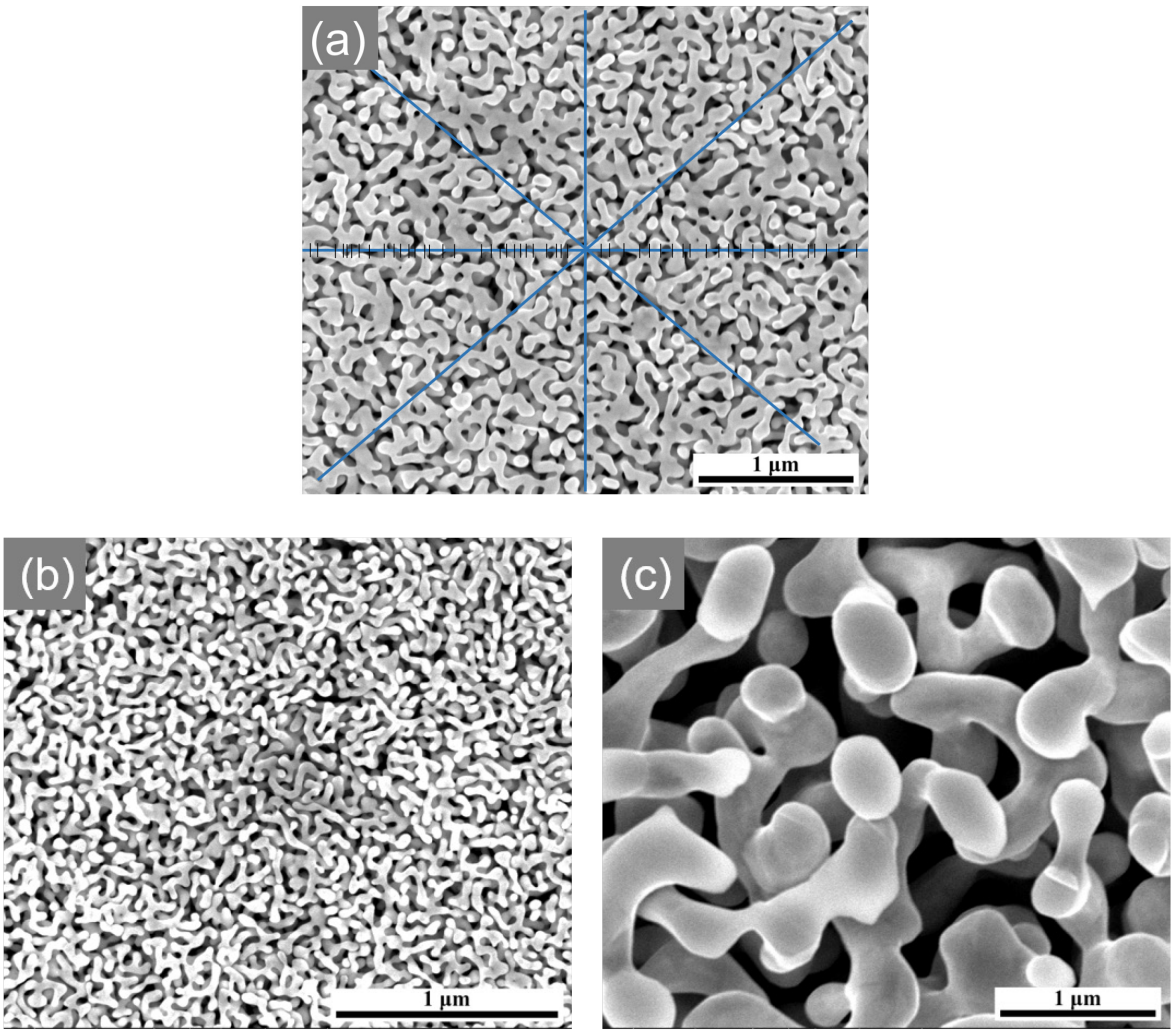

Figure 3.5. (a) An example of the ligament size estimation by the linear intercept method. SEM images of NPG surface structure with ligament size of (b) 35 nm and (c) 350 nm obtained by dealloying and post-annealing, respectively.

3.2.2 Thin film NPG

3.2.2.1 Precursor alloy

Another precursor alloy film (thickness: 2.5 μm) was prepared via deposition from a commercial $Au_{25}Ag_{75}$ target (purity: 99.99%, Sindlhauser Materials) on a cuboid pure Au substrate (length: 2 mm, width: 1.4 mm and height: 1.7 mm, Au ≥ 99.99%, Sigma-Aldrich) by a DC magnetron sputtering device. The Au substrates were cleaned by argon plasma etching, and then transferred via a load lock to the sputter chamber where the base pressure is below 4E-7 mbar. During deposition, the working pressure in the sputter chamber is 5.5E-3 mbar established by a constant flow of 7 SCCM (standard cubic centimeter per minute) of argon (purity: 99.99%). Sputtering was performed at a constant power of 50 W, and the distance between the sample and target is around 15 cm. The thickness of the film can be altered via control of sputtering time. Here, $Au_{25}Ag_{75}$ films with 2.5 μm thickness used in this work were generated by 90-minute sputtering procedure. The schematics of thin film and Au substrate is illustrated in Figure 3.6.

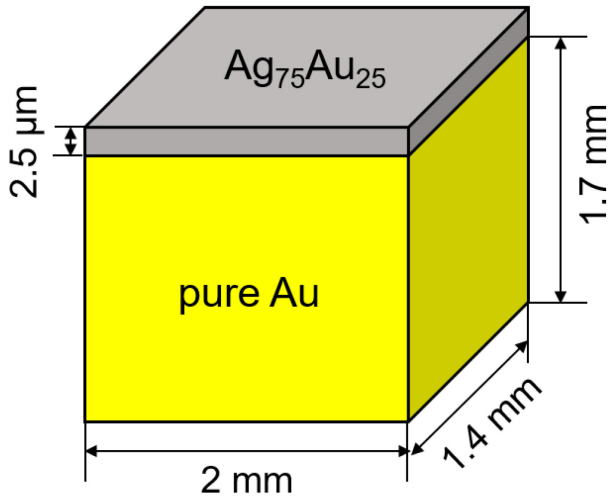

Figure 3.6. Schematic of NPG thin film with thickness of 2.5 μm deposited on a cuboid pure Au substrate using sputter device.

3.2.2.2 Dealloying

After sputtering, $Au_{25}Ag_{75}$ films together with the Au substrate were transferred to an electrochemical cell for dealloying and subsequent reduction treatment, the processes of which are the same as that used for the fabrication of bulk NPG, as described in the last section. Dealloying of a NPG thin film lasted around 10 min, which is very short compared to the

corresponding time for bulk NPG (several hours). The SEM image of surface structure of a NPG thin film after synthesis is presented in Figure 3.7 (a). Apparently, the nanoporous structure of NPG is homogeneous, similar to the structure of bulk NPG, and the average ligament size is around 25 nm.

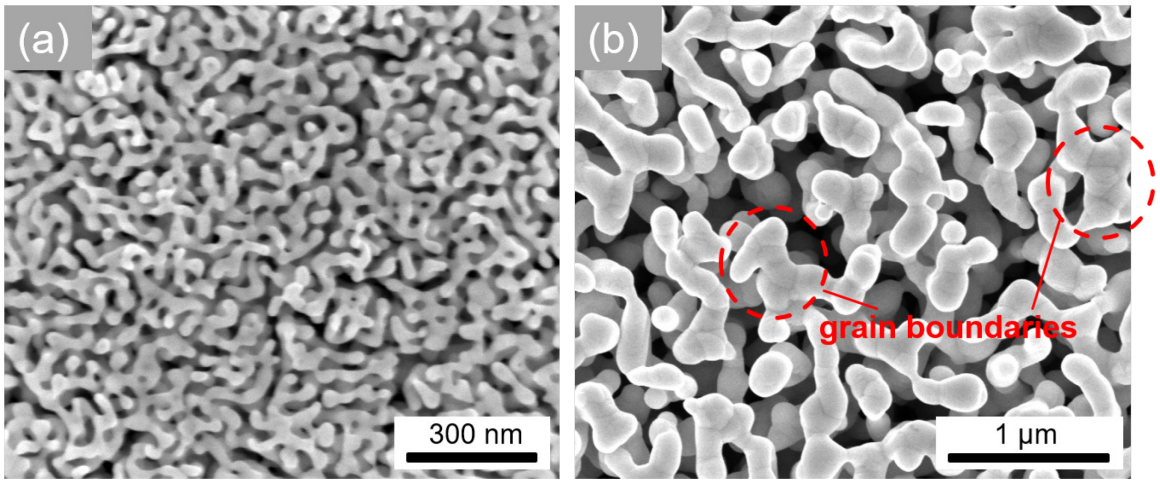

Figure 3.7. SEM images of the network structure of NPG films with different ligament size (*L*). (a) *L=25 nm* fabricated by electrochemical dealloying in 1M $HClO_4$ at room temperature. (b) *L=200 nm* fabricated by free corrosion in 3.585 mol/L HNO_3 at 80°C.

Unlike bulk NPG, whose ligament size can be tuned by heating treatment while the network structure is maintained, as mentioned in section 3.2.1, annealing causes high stress that accompany extensive sintering and cracks in NPG film samples due to the constraints from the bulk Au substrate. Therefore, the coarse structure (ligament size: 200 nm) of a NPG film was fabricated through another dealloying protocol, namely free corrosion, where the master alloy was dealloyed in a 3.585 mol/L HNO_3 aqueous solution diluted from a standard concentrated HNO_3 (65%, Carl Roth) at 80°C for 3 hours. The temperature of HNO_3 solution during dealloying was controlled using a refrigerated bath circulator. The corresponding SEM image of the coarse structure with a ligament size of 200 nm is displayed in Figure 3.7 (b). Clearly, numerous grain boundaries are observed on the ligament surface, as marked by the red cycles. These grain boundaries might come from the master alloy with fine or ultrafine crystals, which can be verified by the EBSD and XRD results presented in the following section 3.3.1, since the dealloying process is thought not to change the orientation structure [176]. Apart from that, a recent study focusing on the structure development of NPG during annealing revealed that some particles detachment and reattachment during structure coarsening can lead to the

formation of new grain boundaries [177]. Similar to the bulk NPG, no residual Ag content in NPG thin films can be detected by Energy-Dispersive X-ray spectroscopy (EDX). Since ligament size does not rise with increasing the time of free corrosion, 200 nm is the maximum size we can achieve by this method.

The information of all the NPG samples synthesized by different methods used in the current work are summarized in Table. 3.1.

Table 3.1. NPG samples fabricated by different methods

Sample	Shape	Fabrication method	Post-annealing	Ligament size (nm)
bulk NPG	cylinder	electrochemical dealloying in 1 M $HClO_4$ at room temperature	/	35
			300°C/12 min	50
			300°C/60 min	200
			500°C/60 min	350
	disc-shaped		/	35
			500°C/60 min	300
NPG thin film	rectangle		/	25
		free corrosion in 3.585 mol/L HNO_3 at 80°C	/	200

3.3 Materials characterization

3.3.1 Microstructure characterization

Scanning electron microscopy (SEM, FEI Nanolab 200) was employed to characterize the microstructure of the samples. After NPG samples synthesis, they were mounted on a SEM stub made of stainless steel using gold paste (Plano). The secondary electron images of NPG were obtained using Everhart Thornley detector (ETD) in field-free mode while the Thru-the-Lens detector (TLD) in immersion mode is employed for high-resolution images. Here, the focused working distance is 5 mm, and the accelerating voltage of the beam is 10 kV. The overview of network structure, the shape and the size of ligaments can be characterized and analyzed by SEM.

In addition, more comprehensive information regarding the microstructure of samples can be gained if the SEM instrument is equipped with other detectors, such as Energy-Dispersive X-ray (EDX) and Electron Backscatter Diffraction (EBSD) detectors. With EDX technique, the

chemical elements of samples were analyzed qualitatively and quantitatively according to the characteristic X-ray emission from samples stimulated by the electron beam. Here, the amount of residual Ag content in NPG samples after preparation was analyzed by EDX.

EBSD technique, providing crystallographic information of materials, has been widely employed in many scientific investigations. Employing that, crystal orientation maps of bulk $Au_{25}Ag_{75}$ alloy and $Au_{25}Ag_{75}$ thin films, as shown in Figure 3.8, were analyzed in this thesis. During the measurement, the focused working distance was around 10 mm and the sample was tilted to 70º. It is seen that the orientation map of the bulk master alloy is clear and the corresponding grain size is around 20~30 μm, while many blind spots are observed on the orientation map of thin films made via sputtering as a result of the weak Electron Backscatter Patterns, which might be because the grain size of such samples is below the resolution of EBSD.

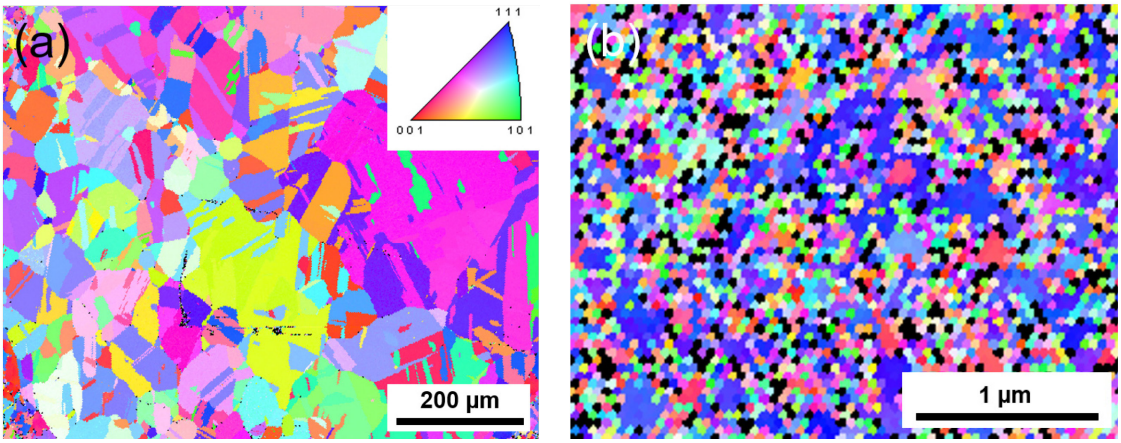

Figure 3.8. Electron Backscattering Diffraction (EBSD) orientation map of (a) bulk $Ag_{25}Au_{75}$ alloys and (b) $Ag_{25}Au_{75}$ thin films surface before dealloying.

Since the crystallographic information of the thin films can not be characterized accurately by EBSD technique, the X-ray diffraction (XRD) was employed for analysis of the orientation and grain size of these two types samples before dealloying, the results of which are shown in Figure 3.9. As can be seen, bulk $Ag_{25}Au_{75}$ and $Ag_{25}Au_{75}$ thin films show a strong intensity in (111) planes, implying a texture with <111> perpendicular to the sample surface. The sharp peak in this planes observed from these two types samples indicates coarse grains existing along the thickness direction of the samples. However, the diffraction peaks in other planes of thin films, such as (200) and (311), broadens and their intensity decreases dramatically, comparing to the corresponding peaks of bulk samples. This reveals that the grains size of thin films in

terms of other directions is much smaller. The grain size in plane direction probably is similar to the small size of the non- <111> oriented grains perpendicular to the film surface because the texture development is restricted to the growth direction of the films. Since the dealloying process does not change the microstructure of the sample, the discrepancy of grain size might be attributed to the different fabrication methods of the master alloys.

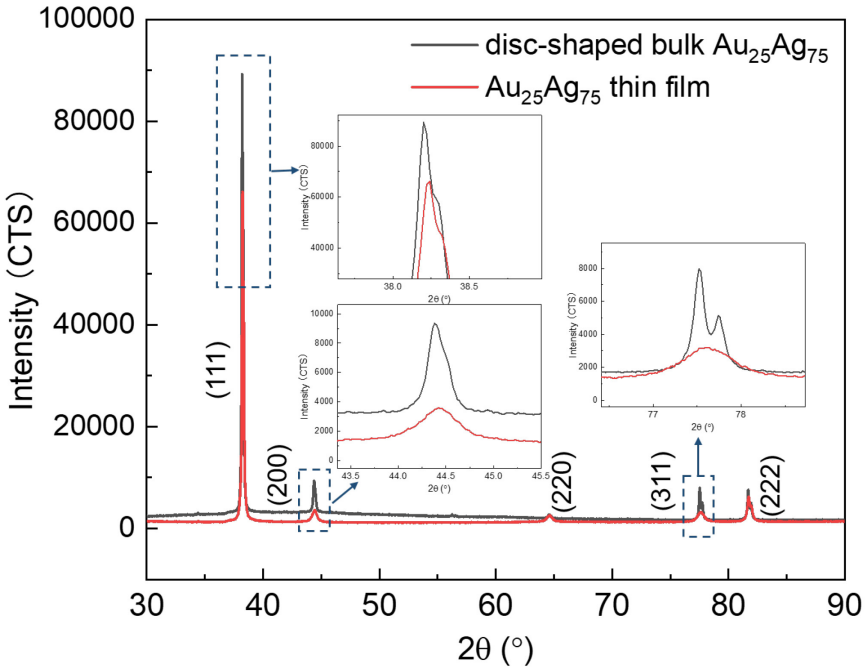

Figure 3.9. X-ray diffraction patterns of intensity vs. the scattering angle, 2θ, of disc-shaped bulk $Ag_{25}Au_{75}$ (black line) and $Ag_{25}Au_{75}$ (red line) thin films before dealloying using a Cu anode.

3.3.2 Micropillar fabrication

NPG micro-pillars used for micromechanical testing were produced by means of focused ion (gallium) beam (FIB) milling installed on SEM. After focusing well with a working distance of 5 mm, samples were tilted to 52° where the ion beam was vertical to the sample surface. Adjustment of beam shift made the electron beam and ion beam centered on the same region of the sample, as shown in Figure 3.10 (a), so that we could select the positions of interest from the SEM images rather than imaging with the FIB which would damage our samples.

Cylindrical micropillars were milled out of the polished surface of different bulk NPG samples and NPG films with different ligament size using annular milling technique, which utilizes circular ring patterns [178]. The ion beam remains perpendicular to the sample surface

throughout the entire preparation process. In order to decrease the milling time, the machining process followed two steps, as shown in Figure 3.10 (b), where the ion beam was operated at 30 kV. First, a pillar with a diameter several microns larger than the desired dimension was obtained via a ring pattern cutting at a current of 3 nA. The height of the pillar was controlled by the cutting time closes to the targeted height. The outer diameter of the pattern is around 45 μm, three times larger than the diameter (15 μm) of the indentation flat punch, in order to prevent touching between flat punch and surrounding material during compression, and to enable observed the bottom of pillars when SEM imaging. In the second step of the milling process, another ring pattern, whose inner diameter is identical to the desired diameter, was applied on the pillar obtained from the first step, using a lower milling current ranging from 1 to 0.1 nA, dependent on the final diameter of the pillar, to control the final shape and limit the amount of ion-induced damage. It took approximately 20 to 40 min for the fabrication of one pillar. The annular milling carried out here with the "single-pass" mode, where the ion beam scanned over the pattern once only during the cutting, resulting in a higher sputter yield and help to avoid redeposition on the sidewalls of the pillars [57, 179].

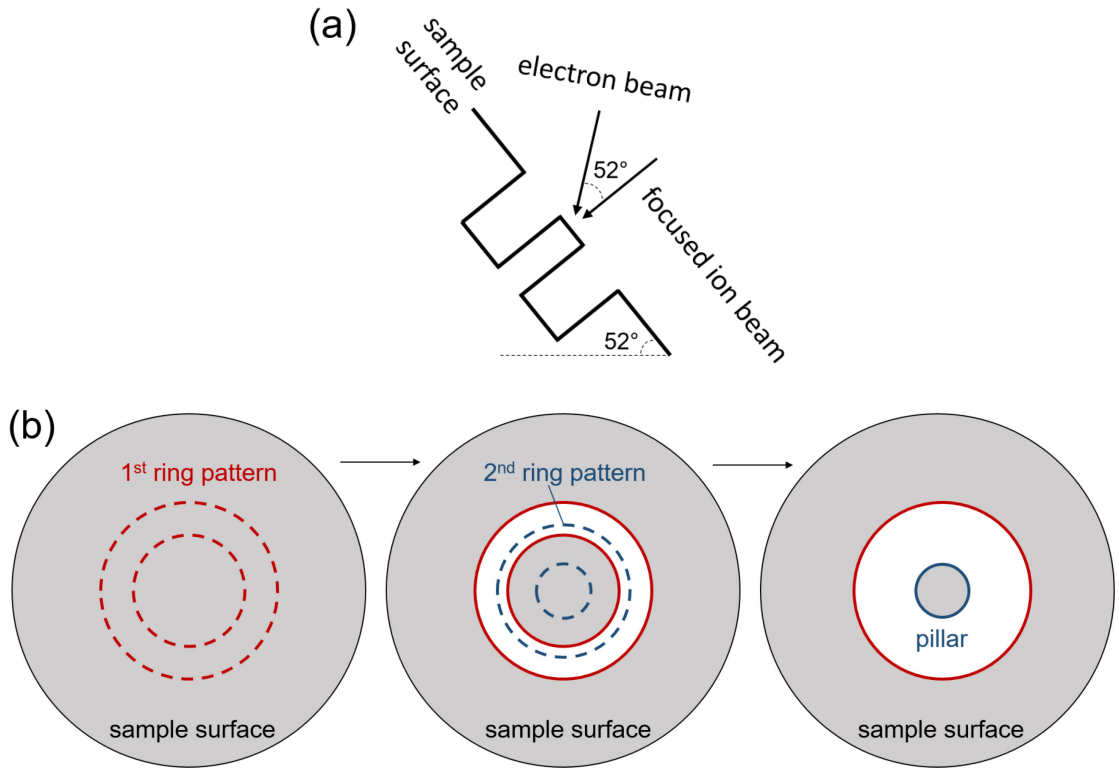

Figure 3.10. Schematics of (a) the SEM-FIB system for the annular milling and (b) two-step FIB milling patterns for NPG pillars fabrication.

The SEM image of a pillar with a diameter of 8 μm and a height of 22 μm cut following the milling processes described above is shown in Figure 3.11. It is seen that the network structure of the pillar is homogeneous and there is no obvious redeposition observed on the structure. The geometry of the pillar is critical for analyzing compression data. The shape of such a pillar is not an ideal cylinder, the diameter at the bottom of the pillar is a little larger than the diameter at the top of the pillar, which usually exists on pillars obtained by the annual milling method even though the cutting current of the ion beam is comparably small. The taper angle of pillars is around 1°, which causes little variation in axial stress along the pillar during deformation, but it can help to support the pillar if there is misalignment existing between the pillar and the flat punch. The height of the pillar is defined as the vertical distance between the pillar top and the underlying material, while the diameter is defined as the diameter at the middle of the pillar height. The aspect ratio of pillar diameter to height is around 1:3, and pillars will not be used in the experiments once their aspect ratio is below 1:2 or above 1:4.

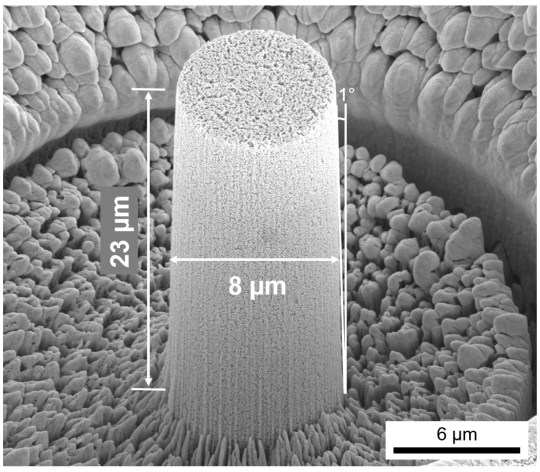

Figure 3.11. SEM image of NPG pillars with diameter of 8 μm and height of 23 μm fabricated by FIB annular milling.

Since each pillar has two varying length-scales, microstructural length-scale (ligament size, L) and deformation length-scale (pillar diameter, D), the ratio $\alpha=D/L$ is used in the current work as a characteristic parameter to couple these two length-scales of the pillars. All the information regarding pillars with varying α, used in this work, is illustrated in Table. 3.2. By varying the ligament size and pillar diameter, the α of pillars used for mechanical testing without electrolyte in Chapter 4 ranges from 6 to 160, while the corresponding range of pillars used for electro-chemo-mechanical coupling is from 7.5 to 228. Due to the compliance of the pillars with coarse

structure, a contact problem occurs between the pillar and flat punch during compression *in situ* in the electrolyte when α<7.5, which negates the testing of samples with lower α.

Table 3.2. Information regarding all the pillars with varying ratios ($\alpha=D/L$) of pillar diameter (D) to ligament size (L)

Samples used for pillar fabrication	**Ligament size, *L* (nm)**	**Pillar diameter, *D* (μm)**	***α=D/L***	**Experiments**
cylindrical NPG	50	8	160	mechanical testing without electrolyte (Chapter 4)
		4	80	
		2	40	
		1	20	
	350	20	57	
		8	23	
		4	11	
		3	8.5	
		2	6	
disc-shaped NPG	35	8	228	electro-chemo-mechanical coupling (Chapter 5 and 6)
		4	114	
	150	8	53	
	300	8	26	
		4	13	
NPG thin films	25	2.5	100	
		1.5	60	
	200	8	40	
		1.5	7.5	

3.3.3 Nanoindentation-based micromechanical testing

Nanoindenter, as one of the most commonly employed instruments on small-scale mechanics, allows us to conduct micromechanical testing under different conditions to measure elastic and plastic behaviors of a large variety of materials. Due to its high resolution, the fundamental mechanisms of deformation and the effects of microstructure on mechanical behaviors can be studied via nanoindentation testing.

With different types of the indenter tip, such as Berkovich and flat punch, nanoindentation, microcompression and microbending testing can be carried out by nanoindenter. In this thesis,

we focus on nanoindentation and microcompression experiments of NPG with and without an electrochemical environment. While Berkovich indentation testing is a convenient method to quantify hardness and elastic modulus, it does not allow the measurement of stress-strain behavior. Furthermore, in porous materials, it is complicated due to the impact of the densification.

Nanoindentation and microcompression testing in the air were conducted by Nano XP indenter (MTS), since it has great loading and displacement capabilities, where the maximum force and displacement of the instrument can reach are 500 mN and 20 μm, respectively. Mechanical testing *in situ* in an electrolyte was implemented by the TI 980 Triboindenter (Bruker). This device provides a multifunctional sample stage, on which the electrochemical cell can be installed. Additionally, the large space of the chamber reduces the risk of touching the indenter tip when refreshing the electrolyte during testing.

3.3.3.1 Nanoindentation

Instrumented indentation testing was implemented on bulk NPG samples using a Berkovich tip made from diamond, in order to measure hardness and elastic modulus. Samples were loaded at a constant strain rate of 0.05/s to the desired displacement, holding for 10 s at the peak load prior to unloading. The schematic diagram of nanoindentation and a typical load (P)-displacement (h) curve are shown in Figure 3.12 (a) and (b). Assuming that only elastic deformation recovery occurs at the beginning of unloading, according to the Oliver-Pharr method [180, 181], the elastic modulus of the sample can be calculated from the contact stiffness (S) which is defined as the slope of the upper portion of the unloading curve and expressed as:

$$S = \frac{dP}{dh} = \beta \frac{2}{\sqrt{\pi}} E_r \sqrt{A} \tag{3.1}$$

where β is a constant that depends on the geometry of the indenter ($\beta = 1.034$ for a Berkovich indenter). A is the contact area which is dependent on the geometry of indenter tip and indentation displacement, and it is expressed by the following approximation:

$$A = C_0 h_c^2 + C_1 h_c + C_2 h_c^{1/2} + C_3 h_c^{1/4} + \cdots + C_8 h_c^{1/128} \tag{3.2}$$

where C_0 ... C_8 are constants determined by curve-fitting procedures. Considering the amount of sink-in, $h_s = \epsilon \frac{P_{max}}{S}$, h_c is the vertical distance along which contact is made (contact depth), as shown in Figure 3.11 (a), which is given by:

$$h_c = h_{max} - \epsilon \frac{P_{max}}{S} \tag{3.3}$$

where h_{max} is the displacement at the maximum load (P_{max}) during loading, ϵ is a geometric constant ($\epsilon = 0.75$ for Berkovich indenter).

E_r is the effective elastic modulus defined by equation 3.4, representing the elastic modulus of the system (including indenter and sample):

$$\frac{1}{E_r} = \frac{1-\vartheta^2}{E} + \frac{1-\vartheta_i^2}{E_i} \tag{3.4}$$

where E and E_i are the elastic modulus of sample and indenter, respectively, ϑ and ϑ_i are Poisson's ratio of sample and indenter, respectively. According to the results of microcompression and molecular dynamics simulation reported in some studies [69, 109, 115], the Poisson's ratio of NPG is close to 0 because of the densification during deformation. Based on the equation 3.4, the elastic modulus of the sample can be determined.

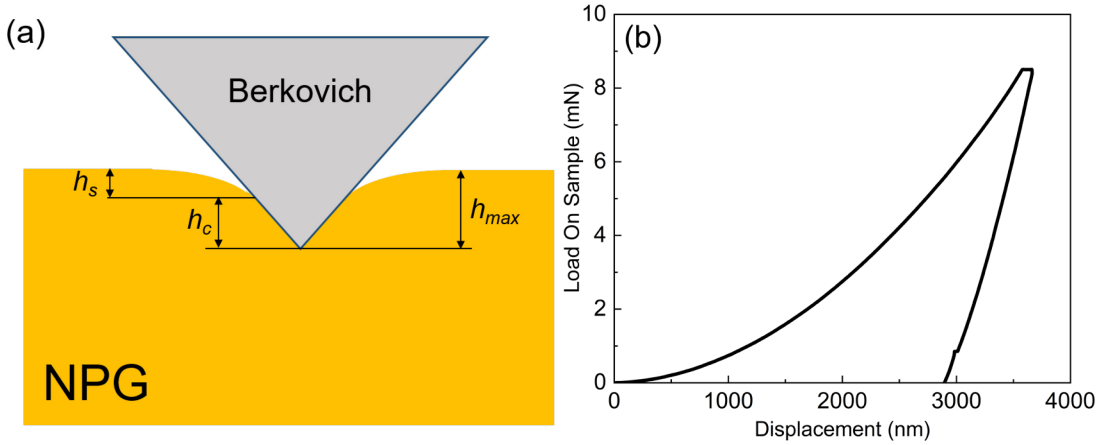

Figure 3.12. Nanoindentataion testing. (a) Schematic diagram of nanoindentation testing on bulk NPG sample with a Berkovich indenter. (b) Typical load (P) - displacement (h) curve.

The hardness (H) of the sample is determined from:

$$H = \frac{P_{max}}{A} \tag{3.5}$$

With the Continuous Stiffness Measurement (CSM) option applied simultaneously, the contact stiffness of the sample during loading can be measured continuously by imposing an oscillation signal with a fixed frequency on the loading signal and analyzing the resulting displacement signal. Thus, the elastic modulus as a function of displacement were obtained,

which is useful for characterizing the varying mechanical properties of the sample during deformation. The CSM mode with oscillation amplitude of 2 nm and frequency of 45 Hz was applied on all the nanoindentation testing in the current work to track the change of elastic modulus of NPG.

3.3.3.2 Microcompression

Compression testing on micro-pillars can be carried out using the nanoindenter outfitted with a flat punch. In this thesis, the mechanical behaviors of NPG pillars fabricated by FIB milling with and without an electrochemical environment is studied through microcompression testing. During testing, pillars were compressed at a constant strain rate (0.001/s) to around 25% strain, holding at the peak load for 10 s before unloading. The schematic diagram on microcompression on NPG is illustrated in Figure 3.13 (a).

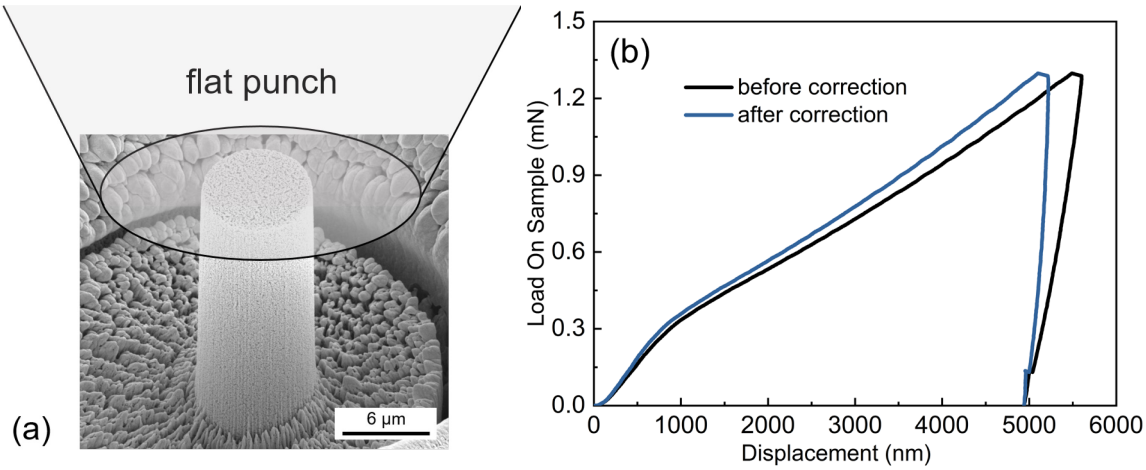

Figure 3.13. Microcompression testing. (a) Schematic diagram of compression on NPG pillar using a flat punch. (b) Compressive load (P)-displacement (h) curves before and after correction.

During testing, the raw load (P_{raw}) and displacement (h_{raw}) data of microcompression were recorded directly by the software. After the identification of the point of surface contact, the load on pillar (P_p) is obtained after compensating the force exerted by the spring that support the indenter shaft:

$$P_p = P_{raw} - K_s h_{raw} \tag{3.6}$$

where K_s is the stiffness of the supporting spring that is determined at the factory. Based on that, the engineering stress (σ) of the deformed pillar is calculated directly:

$$\sigma = \frac{4P_p}{\pi D^2} \tag{3.7}$$

where D is the diameter of pillar.

However, before calculating the engineering strain (ε), the raw displacement (h_{raw}) needs to be corrected since it includes the displacement of the load frame and the substrate material. During testing, the pillar acts like a punch penetrating into the substrate material, resulting in a displacement of below the pillar. Since the substrate material (NPG) here is the same as the pillar, this leads an significant displacement. Therefore, the contributions from the load frame of the indenter and the underlying material of the pillar need to be subtracted from the raw displacement. Based on that, the displacement of pillar (h_p) is determined by:

$$h_p = h_{raw} - h_{surface} - h_{LF} - h_{substrate} \tag{3.8}$$

where $h_{raw} - h_{surface}$ was calculated by the software automatically after surface finding correction. h_{LF} and $h_{substrate}$ are displacement of load frame and substrate material, respectively, and they are calculated by the following two equations [182]:

$$h_{LF} = \frac{P_p}{S_{LF}} \tag{3.9}$$

$$h_{substrate} = \frac{(1-\vartheta^2)P_p}{ED_{bottom}} \tag{3.10}$$

where S_{LF} is the load frame stiffness. E and ϑ are elastic modulus and Poisson's ratio of the substrate, respectively, and D_{bottom} is the diameter at the bottom of the pillar. The load-displacement curves before and after correction are shown in Figure 3.13 (b). The engineering strain ε was calcuated using the corrected displacement (h_p) and the initial height (H_o) of the pillar:

$$\varepsilon = \frac{h_p}{H_o} \tag{3.11}$$

The elastic modulus (E_p) of the pillar, defined as the slope of the stress-strain curve in the elastic deformation, can be estimated from the slope of the upper portion of the unloading stress-strain curves where we assume that only elastic recovery occurs.

$$E_p = \frac{d\sigma}{d\varepsilon} \tag{3.12}$$

The E_p of the pillar can also be calculated from the dynamic contact stiffness of pillar (S_p) that is measured basing on the CSM mode, as shown in equation 3.13. The oscillation amplitude

and frequency of the CSM mode applied for microcompression here were 2 nm and 45 Hz, respectively, as was used for the Berkovich nanoindentation test.

$$E_p = \frac{d\sigma}{d\varepsilon} = \frac{dP}{dh_p}\frac{4H_o}{\pi D^2} = S_p\frac{4H_o}{\pi D^2} \tag{3.13}$$

4 Intrinsic and extrinsic size effects in the mechanical behavior of nanoporous gold

The "smaller is stronger" size effect of conventional metals is well established for decades. In the case of NPG with a complex network structure, the influence of microstructural length-scale (intrinsic size) on mechanical properties has been found in many studies, while less research focused on the impacts of the deformation length-scale (extrinsic size). Recent investigation in hierarchical NPG [21], where the interconnected ligaments are themselves nanoporous, indicated that the overall mechanical behaviors are strongly dependent on both the upper and lower hierarchical length scales, which implies that both the extrinsic and intrinsic size effects need to be considered in describing mechanical behavior of NPG, especially when there are only several ligaments involved in the network structure. In this chapter, nanoindentation and microcompression testing were carried out on NPG samples. By varying both micropillar diameter and ligament size, the coupled influence of microstructure length-scale and sample size on mechanical responses of NPG was investigated here.

4.1 Microstructure and micropillars of NPG

Cylindrical NPG samples (diameter: 1 mm, height: 2 mm) with nominal ligament sizes of 35 nm, 50 nm, 200 nm and 350 nm were used in this chapter for nanoindentation and microcompression testing. The NPG cylinders were synthesized by electrochemical dealloying, which yields a ligament size of around 35 nm, while coarser structures were obtained via post-annealing treatment, as described in Chapter 3.2.1. SEM images of NPG samples with ligament sizes of 35 nm, 50 nm, 200 nm and 350 nm were shown in Figure 4.1(a)-(d). The method of estimating the ligament size of the network structure is detailed in Chapter 3.3.1. As can been seen, the porous network structure exhibits similar geometry characteristics, except for the feature size, suggesting that NPG appears to coarsen in a self-similar way, in good agreement with the corresponding results in [9, 114, 183, 184], where the morphological and topological features of the 3D volumes of NPG reconstructed by FIB tomography were found to be nearly invariant during annealing.

Micropillars with diameter (D) ranging from 1 to 8 μm and from 2 to 20 μm were produced in the polished surface of NPG samples with nominal ligament size (L) of 50 and 350 nm, respectively, utilizing FIB annular milling. Details regarding the machining processes were presented in Chapter 3.3.2. By varying the ligament size and pillar diameter, the ratio ($\alpha=D/L$) of pillars used in this chapter can be changed from 6 to 160, as summarized in Table. 3.2.

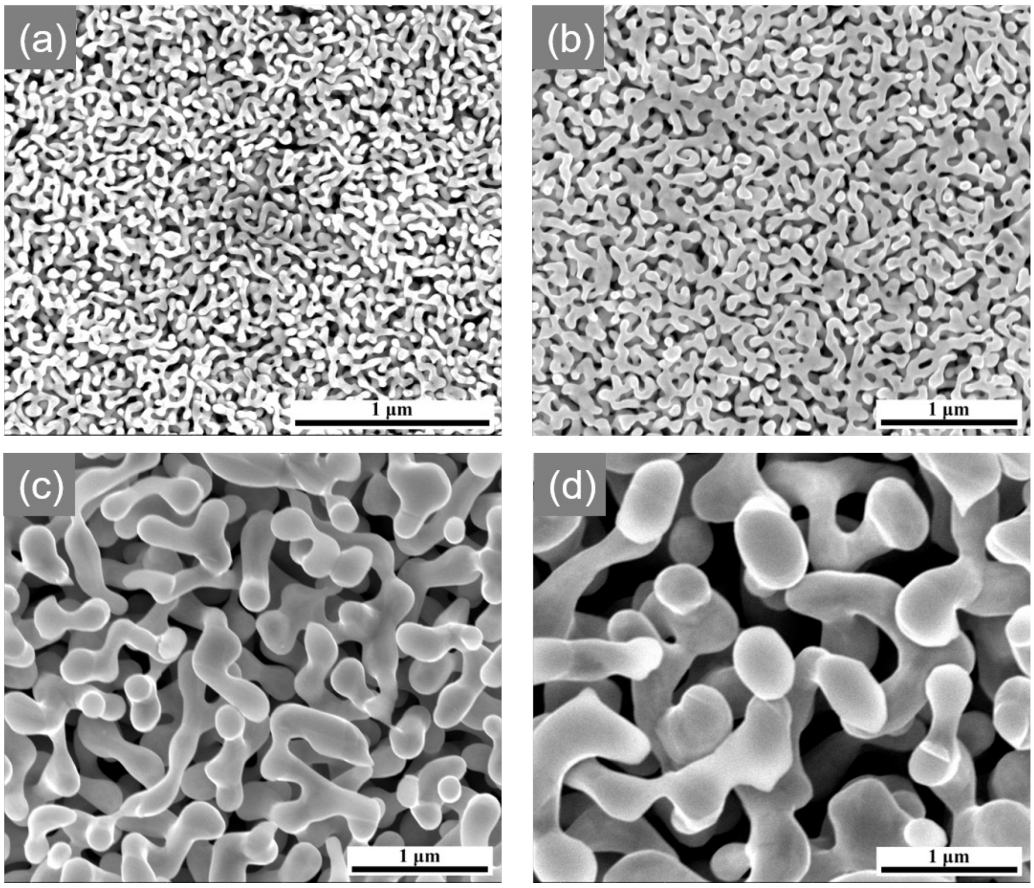

Figure 4.1. SEM images of cylindrical NPG surface with different ligament size (L) obtained by electrochemical dealloying and post-annealing. (a) *L=35 nm*; (b) *L=50 nm*; (c) *L=200 nm*; (d) *L=350 nm*.

The SEM images of pillars with different α were shown in Figure 4.2. It is seen that all of pillars show excellent bicontinuous porous structure, and no significant redeposition caused by FIB milling is observed, even at the smallest values of α. The number of ligaments included in the pillars decreases considerably with decreasing α for a fixed ligament size, resulting in a decrease in the number of load-bearing units. That is to say that the number of interconnected rings providing structural support and thus contributing to the to the mechanical behavior decreases with decreasing α, as shown in Figure 2.2 [115]. It is important to note that the base

of all pillars can be observed clearly from the SEM images, which helps us to determine the height of the pillars simply and accurately, since any errors in height estimation can lead to inaccuracies in the stress-strain analysis of compression.

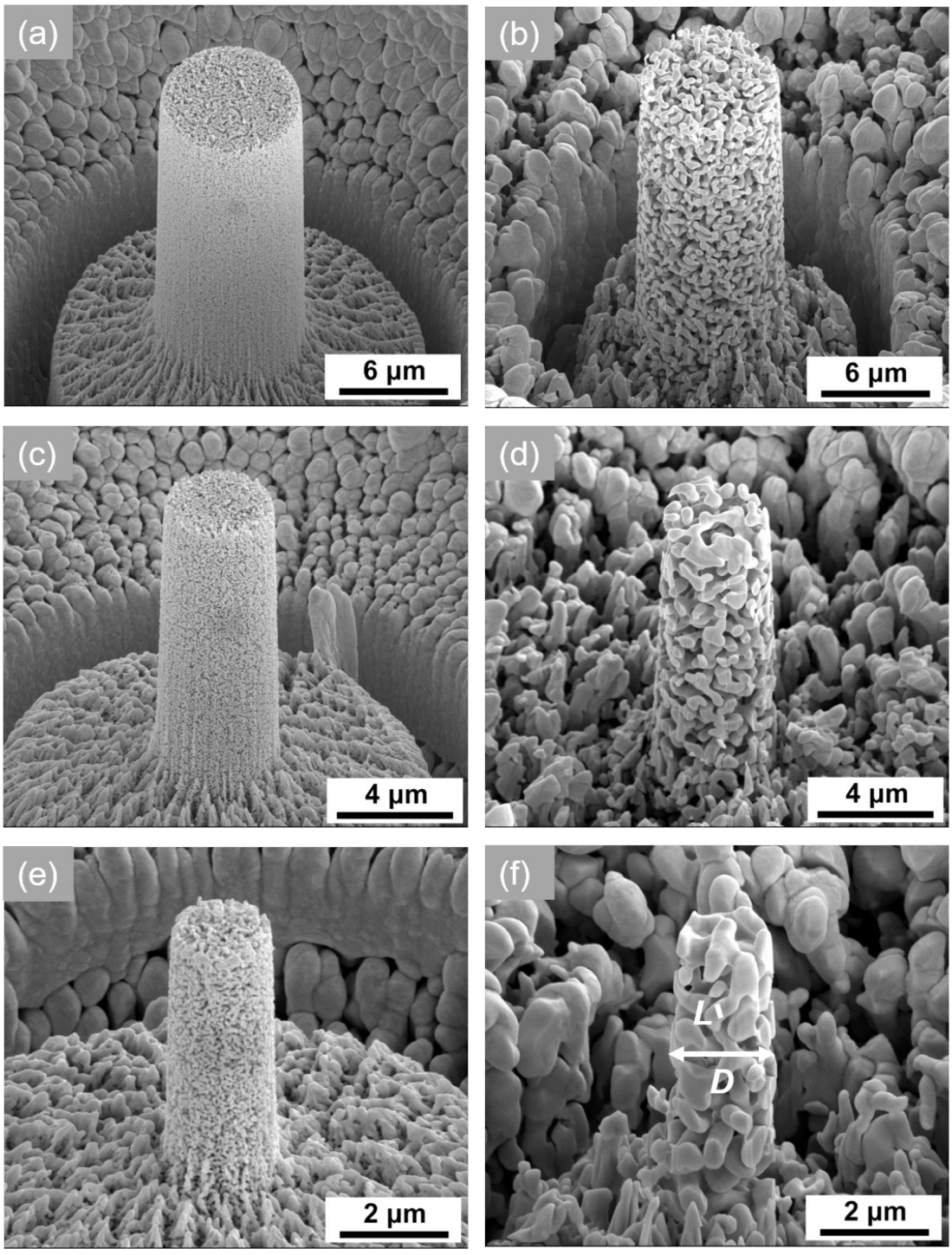

Figure 4.2. NPG micropillars with varying ratio (α) of pillar diameter (D) to ligament size (L). (a) *D= 8 μm, L=50 nm, α=160.* (b) *D=8 μm, L=350 nm, α≈23.* (c) *D=4 μm, L=50 nm, α=80.* (d) *D=4 μm, L=350 nm, α≈11.* (e) *D=2 μm, L=50 nm, α=20.* (f) *D=2 μm, L=350 nm, α≈6.*

4.2 Micromechanical behavior of NPG

4.2.1 Nanoindentation

Nanoindentation, as a micromechanical technique with less requirement for sample preparation, has been widely used in many investigations to characterize the elastic and plastic behaviors of materials. In this chapter, Berkovich nanoindentation combined with the continuous stiffness measurement (CSM) mode with an oscillation of 2 nm and a frequency of 45 Hz, was performed on bulk cylindrical NPG samples with different ligament size, in order to study the effects of ligament size on the elastic modulus and hardness. The details of experimental processes and the corresponding calculations are described in Chapter 3.3.3. During testing, a diamond Berkovich indenter tip penetrates into the sample surface at a constant indentation strain rate of 0.05/s until reaching the desired displacement, the load is held constant for 10s prior to unloading. The load-displacement curves of NPG with ligament size of 35, 50, 200 and 350 nm, are shown in Figure 4.3 (a). A strong dependence of the load-displacement curves on the ligament size is observed, load increasing with decreasing ligament size for the same displacement, agreeing well with the corresponding results in [62, 185]. Note that the final displacement for each curve is less than the displacement at the peak load due to the elastic recovery during unloading.

The corresponding results of elastic modulus and hardness of NPG as a function of nanoindentation displacement measured dynamically with CSM mode are shown in Figure 4.3 (b) and (d). As observed in both plots, at the beginning of testing (below ~ 200 nm depth regime), elastic modulus and hardness are extremely high, and then they decrease dramatically until reaching a plateau after indentation displacement larger than 800 nm. This nanoindentation size effect in the sub-micrometer depth regime, which also was found in other bulk materials [186], is sometimes attributed to strain gradients, where the large strain gradients in small indentations result in geometrically necessary dislocations that lead to increased hardening [54, 187]. This is less applicable to nanoporous materials. Rather, issues with determining the true area of contact may lead to inaccuracies in the analysis of H and E. In any cases to circumvent this size effected displacement regime, we selected the measured values corresponding to displacement ranging between 2500 and 3500 nm to estimate the average of elastic modulus and hardness of NPG with different ligament sizes. The calculated results are presented in Figure 4.3 (c) and (e). Apparently, ligament coarsening causes a noticeable decrease in both elastic modulus and hardness. As the ligament size increases from 35 to 200 nm, the elastic modulus decreases from 0.79 to 0.14 GPa, and there is a reduction in hardness from 0.04 to

0.006 GPa. However, since the influence of coarse ligaments on dislocation movement is weak, the size effect is not evident in samples with ligament size between 200 and 350 nm.

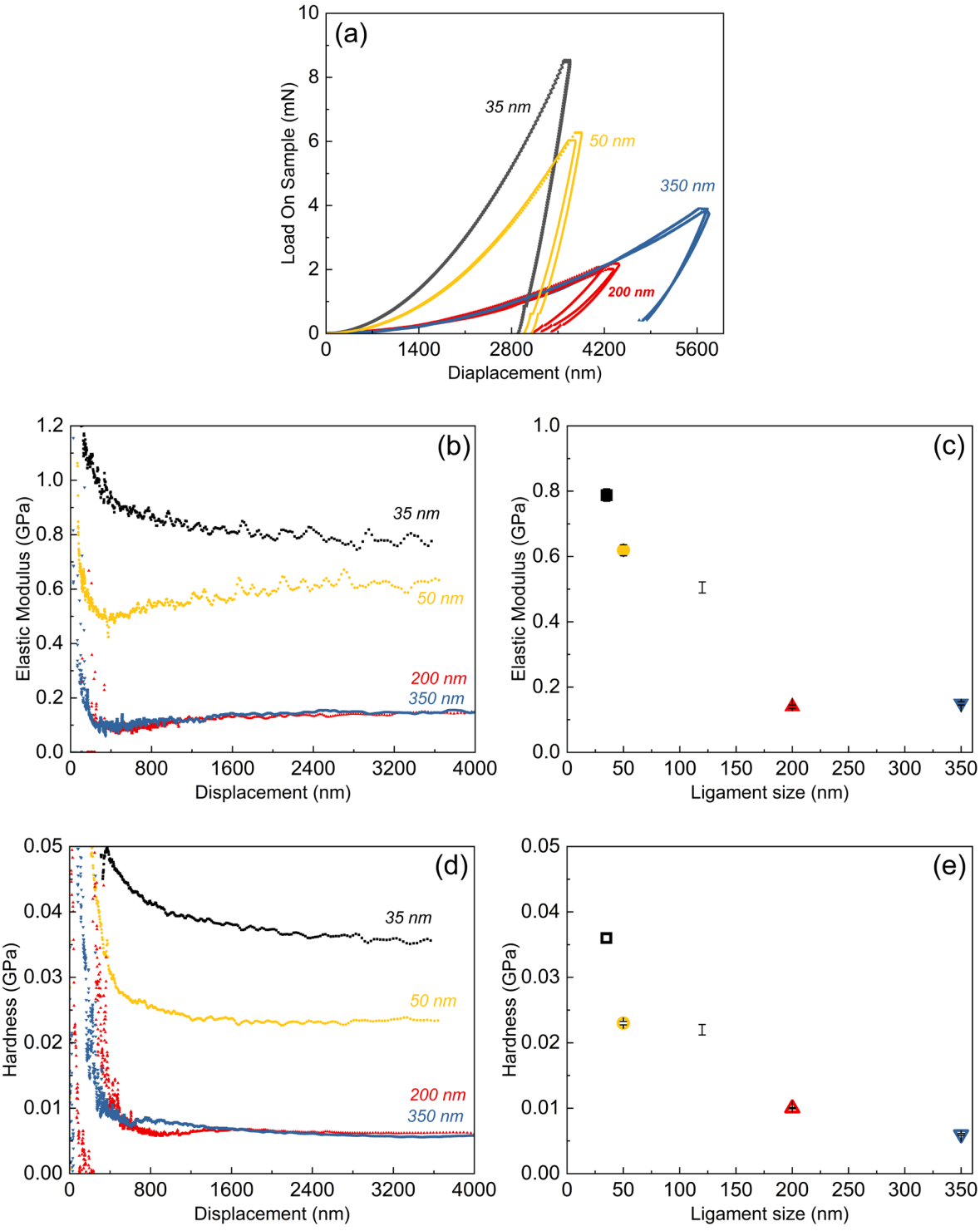

Figure 4.3. Berkovich nanoindentation results of NPG with different ligament size of 35, 50, 200, 350 nm, respectively. (a) Load-displacement curves. (b) Dynamic elastic modulus and (d) hardness measured under continuous stiffness measurement (CSM) mode during testing. The average (c) of elastic modulus and (e) hardness as a function of ligament size.

4.2.2 Microcompression

A set of microcompression tests were conducted on pillars with varying diameter (from 20 μm to 1 μm) and different ligament size of 50 nm and 350 nm, at room temperature using a nanoindenter outfitted with a flat punch tip. The engineering stress-strain curves were calculated from load-displacement curves recorded directly by the instrument. With continuous stiffness measurement (CSM) mode, the dynamic contact stiffness was measured during compression, which can be used for determining the variation elastic modulus over the testing. Details regarding the compression process and corresponding calculations are described in Chapter 3.3.3.

Microcompression results of pillars with varying ratio ($\alpha=D/L$) of diameter (D) to ligament size (L) were shown in Figure 4.4. The engineering stress-strain curves displayed in Figure 4.4 (a), where pillar diameter (D) ranges from 8 to 1 μm sufficiently larger than the ligament size *(L=35nm),* are identical, in agreement with the corresponding results in [60], indicating no influence of pillar diameter on the flow stress when α of pillar varies between 160 and 20. The transition from elastic to plastic deformation can be observed clearly on the flow stress curves. The elastic modulus, as displayed in Figure 4.4 (b), increases significantly with increasing strain during deformation, which is owing to the densification of the porous structure. Yet, it is insensitive to the variation of α, consistent with the trend of flow stress. The SEM images of pillars with $\alpha=160$ ($D=8\ \mu m$) and $\alpha=20$ ($D=1\ \mu m$) before and after compression, as presented in Figure 4.4 (c) and (d), respectively, confirms that pillars experience a uniform deformation. Additionally, no evident difference in diameter of pillar before and after compression is observed, i.e. the transversal strain is nearly zero during compression, implying the Poisson's ratio of this NPG sample is close to zero, consistent with results in [64, 115].

In contrast, the corresponding mechanical results of pillars with ligament size of 350 nm, where diameter changes from 20 to 8 μm, shown in Figure 4.4 (e)-(h), exhibit differences. Here, the corresponding α is smaller ranging from 57 to 6. No distinguishing transition from elastic to plastic deformation is observed on the stress-strain curves, as shown in Figure 4.4 (e), indicating that plastic deformation occurs immediately at the beginning of compression, in agreement with the macrocompression results presented in [16, 109]. The stress-strain curves displayed in Figure 4.4 (e), reveal that the reduction of α from 57 to 23 does not cause a great variation in flow stress, while α varies from 23 to 6 leads to a significant decrease in flow stress. It declines from 10 to 5 MPa at strain $\varepsilon=0.27$ with decreasing α from 23 to 6, where pillar diameter varies from 8 to 2 μm, indicating a significant effect of deformation length scale

(extrinsic size) on the mechanical response. There are several drops on the stress-strain curve when α is around 6, implying the existence of non-uniform deformation and plasticity instability. The elastic modulus as a function of strain, plotted in Figure 4.4 (f), shows the same trend as the flow stress. Although the degree of noise on the measurement of stiffness rises with the reduction of α, the influence of α on the elastic modulus still can be inspected clearly on these curves. Comparing SEM images of pillars before after compression shown in Figure 4.4 (g) and (h), the pillar with $\alpha=23$ ($D=8\ \mu m$) undergoes an expected uniform deformation dominated by compression, while the pillar with $\alpha=6$ ($D=2\ \mu m$) seems to experience a mixture deformation of torsion and compression. This discrepancy might be due to the structural heterogeneity.

In order to further investigate this interesting behavior coming from such small structures with low α, we go into more detail on the stress-strain curves and the SEM images of pillars with $\alpha=8.5$ ($D=3\ \mu m,\ L=350nm$) and $\alpha=6$ ($D=2\ \mu m,\ L=350nm$). As shown in Figure 4.5 (a), stochastic behavior of flow stress is observed for the pillar with $\alpha=8.5$, the flow stress of one of the pillars is extremely lower than that of others, and it keeps a quite low state until the strain reaches 0.23. Comparing the corresponding SEM images displayed in Figure 4.5 (c) of two pillars showing different flow stress responses, no significant discrepancy in the structure is found. Although all pillars are fabricated from the same bulk NPG sample, the position of each pillar on the polycrystalline NPG is selected randomly, resulting in a local geometry or orientation of pillars is different from each other. Some load-bearing units with low connectivity or locating at a favorable deformation position governs the mechanical response and cause the lower flow stress.

Furthermore, another more distinct non-uniform deformation was found when α is around 6. The corresponding stress-strain curves and SEM images of pillars are shown in Figure 4.5 (b) and (d), respectively. Although α is identical, the pillars exhibit totally different responses to the external load. It is seen that the flow stress of one of the pillars is more than two times as high as the stress of others and even higher than the flow stress of pillar with larger α=8.5 shown in Figure 4.5 (a). Interestingly, the SEM images of pillars before and after compression, as shown in Figure 4.5 (d), indicate that the load-bearing units (i.e. the closed rings consisting of interconnected ligaments contributing to mechanical properties of the porous structure, as described in Chapter 2.1.3) of one of the pillars are incomplete. This suggests that the size of the load-bearing units is close to 6 times the corresponding ligament size.

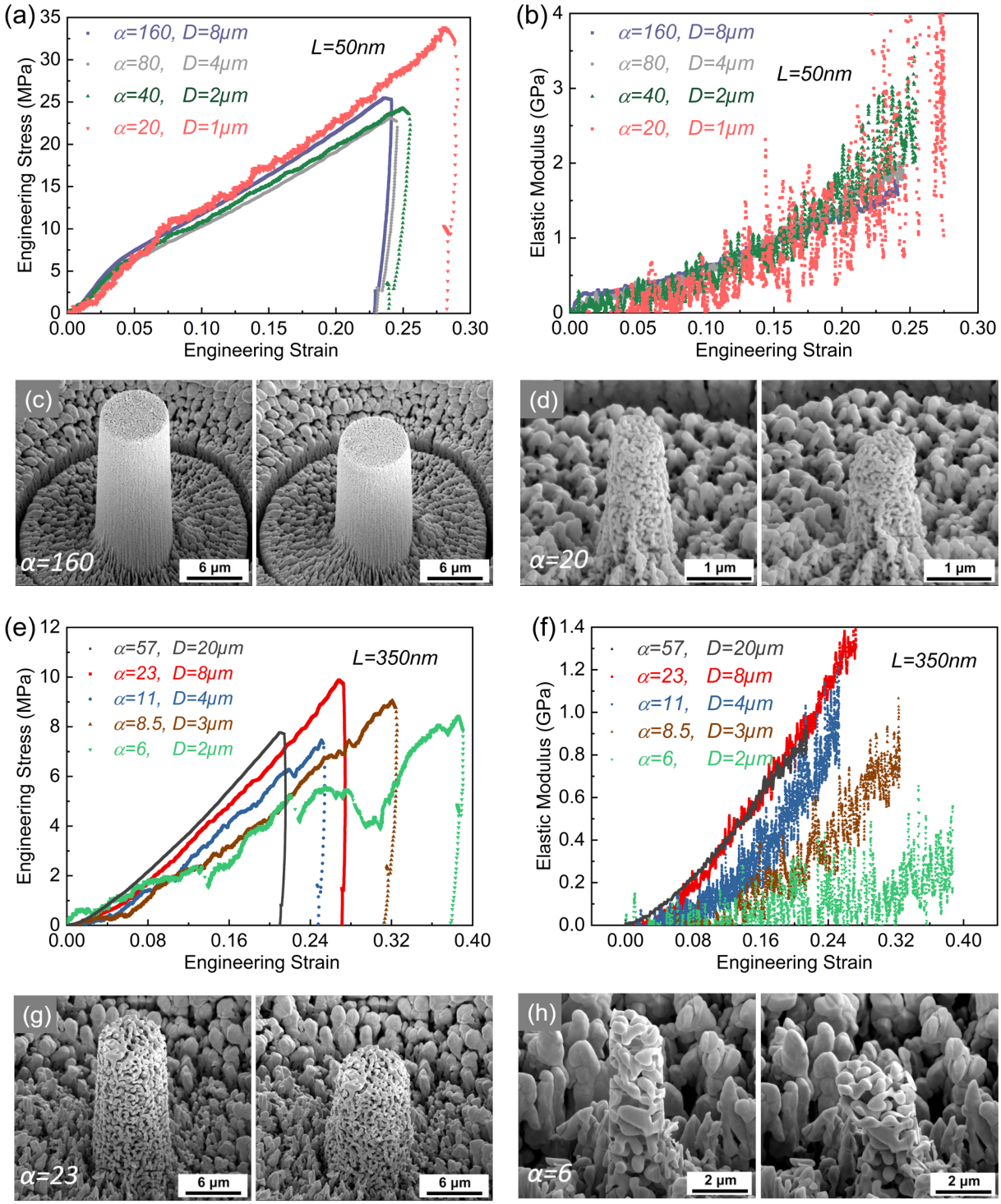

Figure 4.4. Compression results of NPG pillars with varying ratios ($\alpha=D/L$) of pillar diameter (D) to ligament size (L). (a)-(d). Compression results of NPG pillar with ligament size of 50 nm; (a) Engineering stress-strain curves and (b) elastic modulus of pillar with α ranging from 160 to 20; SEM images of pillars with (c) $\alpha=160$ and (d) $\alpha=20$ before and after compression. (e)-(h). Compression results of NPG pillar with ligament size of 350 nm; (e) Engineering stress-strain curves (f) elastic modulus of pillar with α ranging from 23 to 6; SEM images of pillars with (g) $\alpha=23$ and (h) $\alpha=6$ before and after compression.

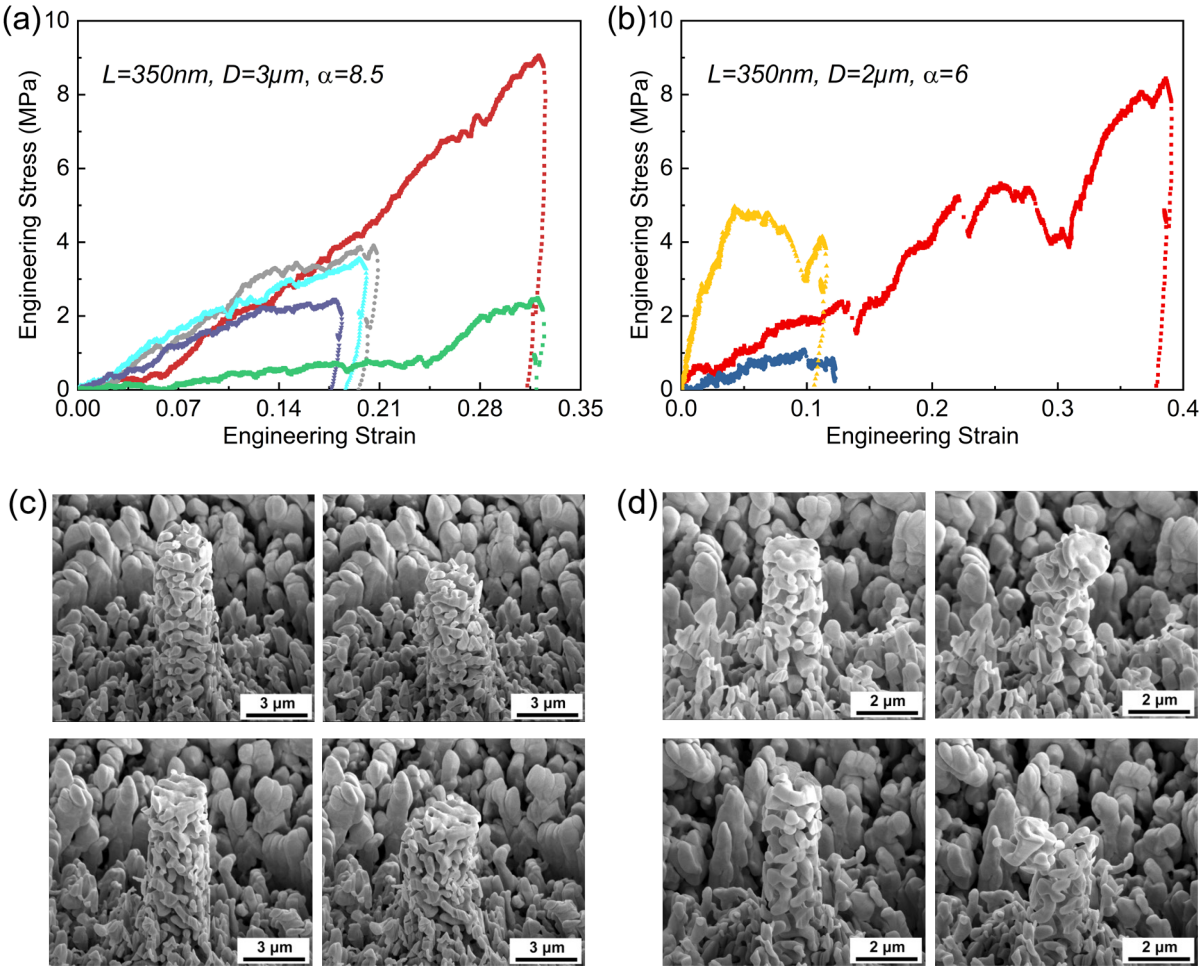

Figure 4.5. Compression results of NPG pillars with different ratios (α) of pillar diameter (D) to ligament size (L=*350 nm*). Engineering stress-strain curves of pillars with (a) α=*8.5* (D=*3 μm*) and (b) α=*6* (D=*2 μm*). SEM images of pillars with (c) α=*8.5* and (d) α=*6* before and after compression.

4.3 Discussion and conclusion

4.3.1 Discussion

Our nanoindentation and microcompression testing results indicate that both ligament size and pillar diameter have a significant influence on the elastic and plastic behaviors of NPG within certain ranges. It was found that reducing the ligament size from 350 to 35 nm can considerably enhance the elastic and plastic properties of NPG. This is consistent with results in other studies [16, 36, 62]. Furthermore, according to microcompression results of pillars with varying ligament size (L) and pillar diameter (D), as shown in Figure 4.4, the flow stress and elastic modulus at strain ε=0.16 of pillars as a function of $\alpha = D/L$ (a relative values of the geometric and microstructure length-scales) is summarized in Figure 4.6. Apparently, both flow

stress and elastic modulus exhibit the same trend in the range of α from 160 to 6. They stay nearly constant for a fixed ligament size when the α of the pillar is larger than 20. Stress is around 17 MPa for *L=50 nm* and 5.5 MPa for *L=350 nm*, while elastic modulus remains ~1 and 0.6 GPa, respectively. Conversely, for the pillars with α lower than 20, where the corresponding ligament size is 350 nm, flow stress and elastic modulus shows a significant decrease with decreasing α. In addition, stochastic behavior and non-uniform deformation were found in pillars with α less 10. The basis for these size effects can be explained in terms of the reduction of connectivity and ligament size distribution, as will now be discussed.

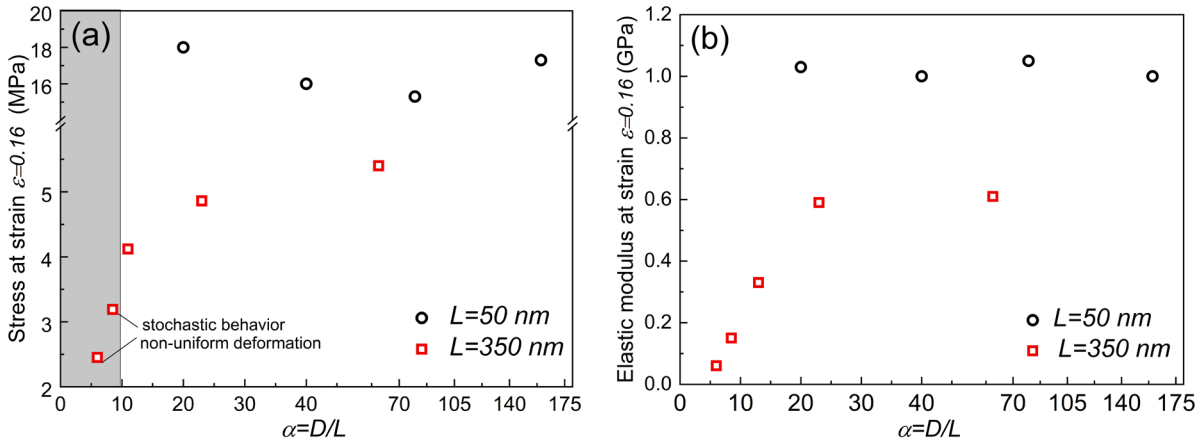

Figure 4.6. (a) Flow stress and (b) elastic modulus at strain *ε=0.16* of pillars with varying ratio (*α,*) of pillar diameter (*D*) and ligament size (*L*). These data are captured from the stress-strain curves and elastic modulus displayed in Figure 4.4.

Cutting a column of finite size out of the monolithic NPG sample will cause a change in the constraints of the ligaments at the column sidewall, as shown in Figure 4.7, which leads to the increase of isolated and dangling ligaments. Thus, the number of interconnected ligaments that contribute to the connectivity density and mechanical properties relative to the accessible total number of ligaments decreases with decreasing α, resulting in the reduction of the amount of the load-bearing units. In the case of the pillars with sufficiently high α, the amount of connectivity reduction induced by cutting is sufficiently small compared to the total value, hence no influence of pillar diameter on the mechanical behavior, as shown in Figure 4.6. Yet, a change can be observed when α drops below 20, both strength and elastic modulus of NPG with *L=350 nm* decrease considerably with decreasing α from 23 to 6. This size effect is opposite from the conventional size effect of "smaller is stronger" found on massive metals [57] that is associated with dislocation movements during deformation. This points to the importance

of connectivity density in determination of elastic and plastic properties of nanoporous materials.

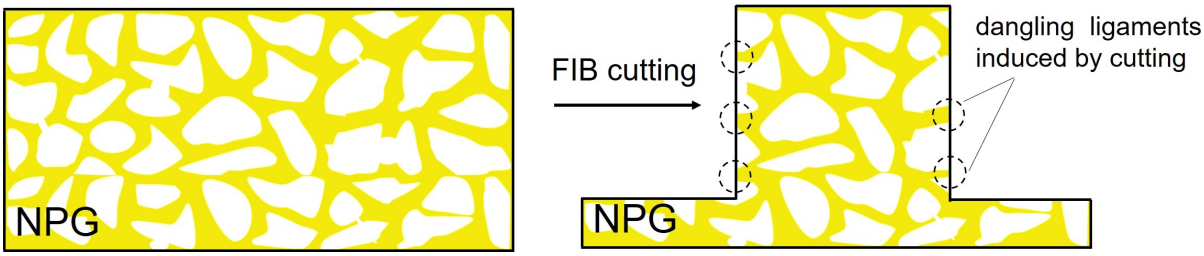

Figure 4.7. Schematic of a pillar cut from a bulk NPG sample by FIB milling, where some ligaments change from the interconnected to the dangling state caused by cutting.

Further reduction of the pillar size, e.g. α <10, might produce the samples with few or even no complete load-bearing units, as shown in Figure 4.8. It could cause an increase of anisotropy in the structure. As a consequence, any failure of the local structure with the weakest load-bearing units dominates the response to the external load, resulting in stochastic behavior or even mechanical instability, as stress-strain curves and SEM images of pillars with α=8.5 and 6 shown in Figure 4.5. In addition, according to the results of the structural analysis on NPG in [114], the ligament size distribution of the network structure fabricated by electrochemical dealloying is broad, revealing that there might exist a discrepancy in the average ligament size for pillars with such low α. This could be another factor leading to the irregular mechanical behavior since the deformation behavior is found to be highly dependent on the ligament size.

Based on the discussion above, a critical ratio of $\alpha=20$ was determined, above which the test structure can be considered a representative volume element (RVE) of bulk NPG resulting in a reproducible and uniform mechanical response. When α is lower than 20, the compression results of pillars with coarse structure ($L=350$ *nm*) reveal that the flow stress and elastic modulus decrease with decreasing diameter of pillars. The stochastic behavior is observed along with non-uniform deformation and failure when α decreases below 10. This size-dependent strength NPG pillars found here is consistent with the corresponding compression results of Al foams [20, 188], where the strength also shows a decrease with decreasing ratio of sample size to cell size when the sample is smaller than the RVE. However, due to the structural discrepancy between Al foams with elongated millimeter-scaled cells and NPG with random and nanoscaled ligaments, the critical ratio ($\alpha=20$) of RVE found here is different from the corresponding critical ratio ($\alpha=8$) of the Al foam. Furthermore, the critical ratio ($\alpha=15$) of RVE of NPG

identified by Hu *et al*. in [114] is a little smaller than the value found in current work. It might be attributed to the different ways of characterization. The RVE defined in [114], as the minimum size above which a set of structural parameters showed minimum variation, is based on the quantification analysis of structural parameters of NPG. Of course, this value holds only for those parameters and does not ensure the mechanical behavior is reproducible. Here, the ratio of RVE is determined via analysis of the results of the mechanical response and structural morphology of pillars.

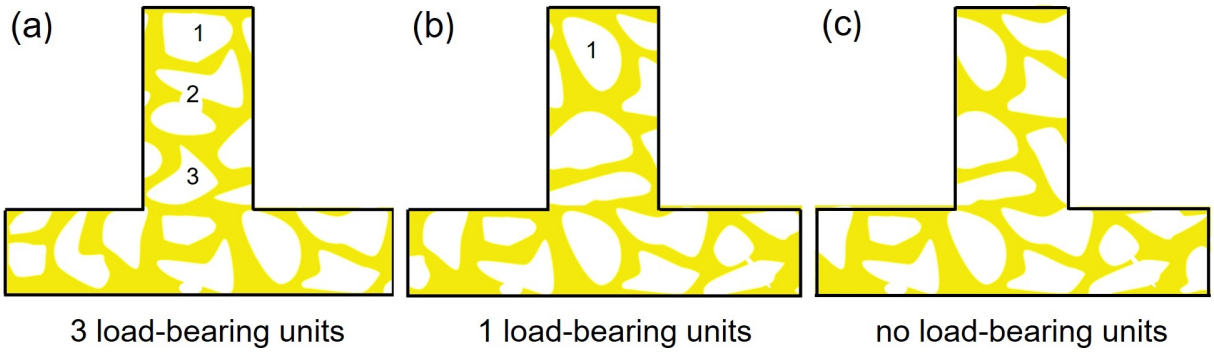

Figure 4.8. Schematics of NPG pillars with (a) 3, (b) 1 and (c) without load-bearing units (closed load-bearing rings).

4.3.2 Conclusion

In the current chapter, the impact of microstructural length-scale and deformation length-scale on mechanical response of NPG were studied by carrying out nanoindentation and microcompression testing on bulk NPG samples and micropillars fabricated by focused ion beam milling, respectively. By varying the ligament size (L, from 1 to 20 µm) and pillar diameters (D, between 50 and 350 nm), the ratio ($\alpha=D/L$) of pillars can be changed from 6 to 160. The micromechanical results indicated that increasing ligament size can lead to a significant decrease in elastic modulus, hardness and strength. Based on the microcompression results of pillars with varying α, it was found that both flow stress and elastic modulus showed independence on the pillar diameter for α higher than 20, while they decreased with decreasing pillar diameter for $L=350$ *nm* when α is below 20. According to this, a critical ratio ($\alpha=20$) was defined here, above which the test structure with $L=350$ *nm* can be considered a representative volume element (RVE) of NPG resulting in reproducible mechanical responses and uniform deformation. Furthermore, stochastic mechanical behaviors along with non-uniform

deformation and failure controlled by the local structure were observed when α decreases below 10. implying that this ratio is close to the corresponding ratio of the load-bearing units .

5 Electro-chemo-mechanical coupling of NPG at the microscale

Coupled electro-chemo-mechanical measurements on macroscopic NPG samples indicate that the mechanical behaviors of NPG can be modulated reversibly by electrochemical potentials application [23, 24], which in turn shows that mechanical properties can be tailed for various applications. Yet gaining a definitive understanding of structural correlations to the behavior is challenging due to the complex structural geometry and length-scales involved. The accomplishment of mechanical measurement *in situ* in an electrochemical environment is a key step toward this goal. In this chapter, we introduce a new experimental approach to investigate the elastic and plastic behaviors of NPG under electrochemical potential at the micro-scale using a modified nanoindentation setup, and then make a comparison with the corresponding results at the macroscale. Note that the NPG samples used here for the pillar fabrication are disc-shaped, not the same as the cylindrical samples used in Chapter 4, to weaken the actuation from the substrate material, as will be detailed in section 5.2.2.

5.1 *In situ* testing set-up and cyclic voltammogram measurement of NPG

5.1.1 *In situ* testing set-up

The micromechanical testing *in situ* in an electrochemical environment was conducted by a TI 980 Triboindenter (Bruker) incorporated with an electrochemical cell (Bruker) and high performance potentiostat. The schematic diagram of the *in situ* testing setup as well as the pictures of nanoindenter and electrochemical cell are displayed in Figure 5.1. The electrochemical cell is installed mechanically on the stage of the nanoindenter, and the indenter tip used for the testing is a flat punch with a length of 10 mm and a nominal diameter of 15 μm fabricated from sapphire. The length of the plat punch used in current work is longer than the standard in order to prevent the contact between the electrochemical system and the indenter transducer. Sapphire is an electrical insulator at room temperature, and it is highly inert and

resistant to chemical attacks in most electrochemical environments. The positions of each pillar are selected and saved by means of optical microscopy.

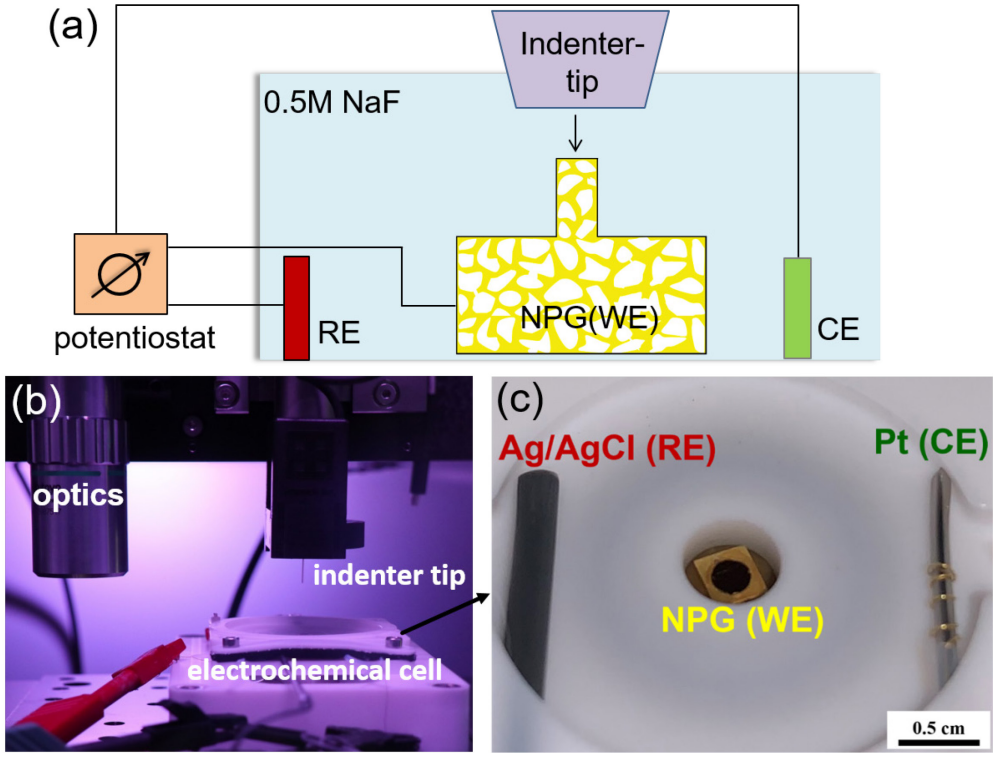

Figure 5.1. (a) Schematic diagram of the *in situ* setup for compression tests on micropillars of NPG in the electrolyte where the potential is controlled by a potentiostat. (b) A picture of a nanoindeter equipped with a tip of flat punch made from sapphire. (c) A picture of electrochemical cell where NPG severs as working electrode (WE), while a commercially available Ag/AgCl electrode and a Pt wire are used as reference electrode (RE) and counter electrode (CE), respectively.

In the electrochemical system, the electrochemical cell made from inert materials can be used in a variety of electrochemical environments. The disc-shape NPG sample is placed within the center of the electrochemical cell, serving as working electrode, while a commercially available Ag/AgCl electrode which is calibrated by a commercial calomel electrode (XR110, Radiometer Analytical) before testing and a platinum wire are used as the reference electrode (RE) and counter electrode (CE), respectively. While most of the macroscopic tests are carried out in $HClO_4$ solution, 0.5 M NaF was preferably used here as to minimize potential damage to the indentation system; NaF has been shown to serve equivalently for actuation of NPG [147]. Only a minimal amount of HF is present in the solution because NaF is a weak base in an

aqueous solution and tends to remain as F^-, rather than generating a substantial amount of HF. The three electrodes are connected to a potentiostat (PG-STAT 302N, Metrohm AUTOLAB) through which the potential applied on the NPG sample is controlled by NOVA (Metrohm) software.

5.1.2 Cyclic voltammogram of NPG in 0.5M NaF aqueous solution

Prior to the electro-chemo-mechanical testing, a cyclic voltammogram (CV) is measured to verify a sufficient electrochemical performance of the setup. A corresponding curve of NPG with a ligament size of 35 nm measured in 0.5M NaF electrolyte with a scan rate of 5 mV/s is presented in Figure 5.2. As can be seen, the maximum and minimum potential for the CV scan is 1.4 V and -0.2V, respectively. All the electrode potentials mentioned in the work are specified vs standard hydrogen electrode (SHE). The most prominent features of the CV curve are the OH-adsorption peak associated with the formation of an OH- monolayer at positive potentials and the desorption peak, i.e., the stripping of that monolayer at negative potential. Basing on that, the potential window of oxidation adsorption and desorption is recorded, through which we are able to change the surface states by selecting appropriate potentials. Here, we select two potentials, 1.4 V and -0.2 V, demoted by "on and "off", respectively, for concision, for the *in situ* micromechanical testing to indicate OH- covered and clean surface, respectively.

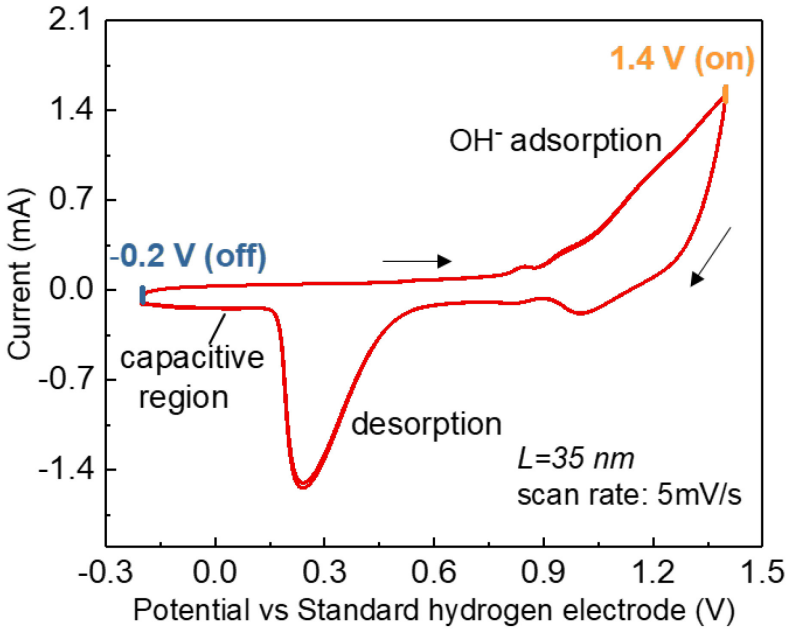

Figure 5.2. Cyclic voltammogram (CV) curve of NPG with ligament size (L) of 35 nm measured in 0.5 M NaF electrolyte at a scan rate of 5 mV/s, scan direction as indicated by arrows.

5.2 *In situ* microcompression

NPG pillars used for *in situ* compression testing are fabricated on disc-shaped NPG samples (thickness: 300 μm, diameter: 2.3 mm) rather than the cylindrical NPG samples used in chapter 4, in order to reduce the actuation of the substrate affecting the displacement measurement of the pillar. Since the micocompression results in Chapter 4 reveal that the extrinsic size of pillar has an influence on the mechanical responses of NPG when the ratio of extrinsic size to intrinsic size decreases below a critical value, here we choose pillars with a high ratio $\alpha = 228$ (ligament size: 35 nm, middle-diameter: 8 μm) to probe measurements of electro-chemo-mechanical coupling at the microscale. Details regarding pillar preparation were described in section 3.3.2.

During *in situ* testing, pillars are compressed at a constant strain rate of 0.001/s under potentials control. A target maximum displacement of 4500 nm was used, in part due to the limitation of the nanoindenter displacement range. This displacement corresponds to a nominal engineering strain of 20%, which provides sufficient strain range without leading to significant densification, The latter could influence the flow of electrolyte through the structure when carrying the experiments out in an electrochemical environment. The engineering stress-strain curve was calculated from load-displacement curves using the diameter of the corresponding pillar and correcting for the underlying substrate deformation, as described in section 3.3.3. The elastic modulus was calculated from the slope of the initial 20% of data of each unloading curve.

5.2.1 Microcompression at constant potential

A set of pillars was compressed in air as well as in the electrolyte with the constant potential -0.2 V (off) and 1.4 V (on), and the results are shown in Figure 5.3. Multiple partial unloading was applied on pillars during the mechanical test in order to calculate the elastic modulus at different stages of deformation. There, any given load-unload segment was carried out at a single potential state, i.e., on or off. The engineering stress-strain curves, as exhibited in Figure 5.3 (a), measured in air and at -0.2 V are the same, which implies no influence from the infiltration of liquid. The averaged yield strength, represented by the flow stress at 2%, from 5 micropillars is around 14.78±1.47 MPa in air and 14.87±0.36 MPa at -0.2V, indicating high reproducibility of the mechanical setup. However, the flow stress obtained with potential off (referring to clean) and on (referring to OH^- coverage) including the unloading steps shows strongly different behavior. The strength increased by 32% when OH^- is adsorbed on the ligament surface, compared to the strength of an identical pillar with a clean surface. This agrees well with the macrocompression results of similar samples in [24]. Interestingly, the width of the hysteresis loop during the unloading steps increases with increasing strain.

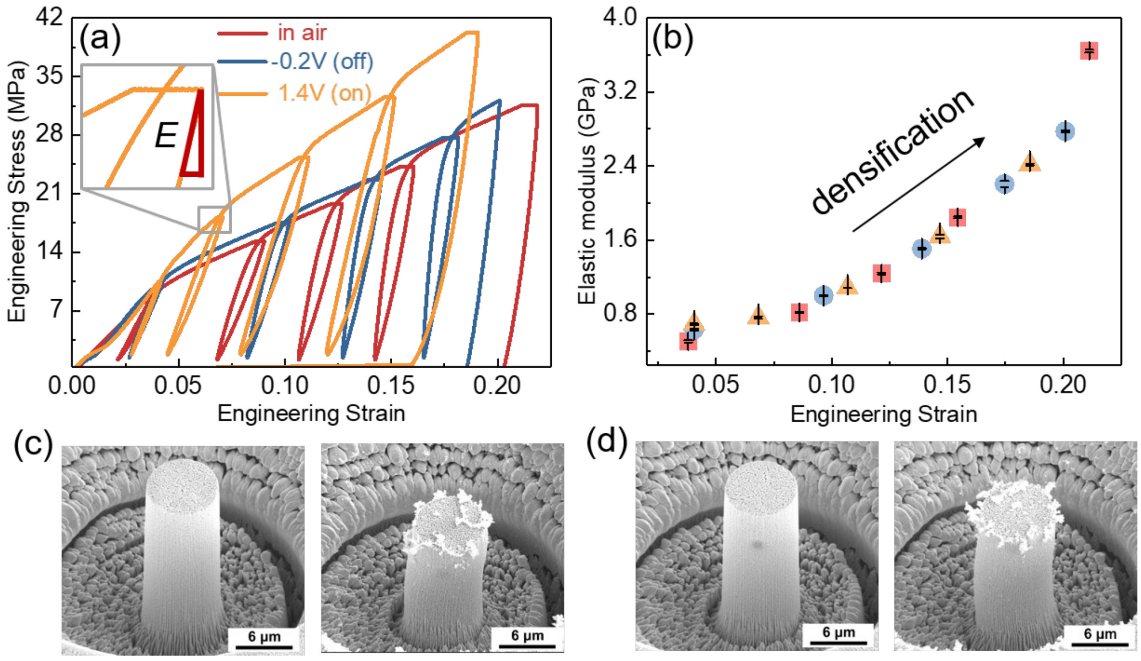

Figure 5.3. Results of microcompression with and without electrolyte in the pores of NPG with ligament size of 35 nm and middle-diameter of 8 μm. (a) Engineering stress-strain curves measured in air, and at two constant potentials (1.4 V and -0.2 V) in 0.5 M NaF electrolyte. 1.4 V corresponds to ligament surface covered by OH monolayer, while -0.2 V represents a clean surface. (b) The variation of elastic modulus was calculated from each unloading curve during compression tests. SEM images of pillars are taken before and after compression (c) in air and (d) at -0.2 V.

The variation of elastic modulus, E, as calculated from the slope of the initial 20% of data of each unloading curve is illustrated in Figure 5.3 (b). It is apparent that E increases significantly (from 0.51±0.01 GPa to 2.75±0.05 GPa) during compression largely because of the densification of the samples, where some dangling ligaments may come to contact with other ligaments and become load-bearing units. Yet the effect of surface adsorption on E is not observed in this experiment; the modulus as a function of strain is identical for both cases of applied potential. The standard deviation of the determined elastic modulus measured from three micropillars at each surface state is less than 3% at all stages of deformation. The precision of the measurement is high enough that a change of Young's modulus of 8% or more, as reported in Ref. [23], should be clearly discernible. This discrepancy between micro- and macroscale experiments might indicate a history dependence of the mechanism of stiffening, in which the surface state and its possible change with the applied potential depend on its strain path and applied load. The SEM images of two pillars before and after compression, as shown

in Figure 5.3 (c) and (d), confirm uniform deformation. It should be noted that the white particles observed on the pillar surface are NaF in crystalline form originating from the electrolyte after drying in air before transferring it into the SEM; it is not related to the deformation of the pillar.

5.2.2 Microcompression under potential jumps

Microcompression behavior of pillars measured under potential jumps are also explored in the current study. Initially, a standard single load-unloading function along with potential jumps was imposed on the samples, and the corresponding results were shown in Figure 5.4. It is seen that the variation of flow stress modulated by potential jumps shows the same trend as the corresponding results at the macroscale. However, there is existing an unexpected time-dependent flow stress when potential changes from off to on, and pronounced hysteresis in flow stress when potential switches from on to off, which is attributed to the actuation of the substrate materials. During *in situ* testing, the whole NPG sample is immersed in the electrolyte. Therefore, any actuation resulting from the application of the potential will occur to the whole sample, not just the pillar of interest. Based on the actuation results found in [147, 148], the estimated length change of bulk NPG induced by the OH adsorption at high potential ranges between 0.03 and 0.1% (mainly depending on the ligament size). This influence of actuation induced by potential switching on the measured displacement is neglected in the deformation of bulk samples, but cannot be ignored in micropillar experiments, in which the displacement due to deformation is concentrated on the pillar but the displacement due to actuation originates from the whole macroscopic sample.

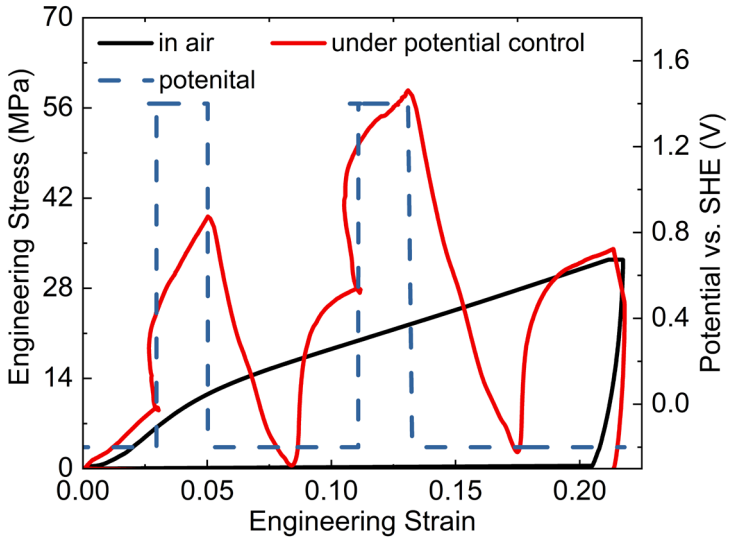

Figure 5.4. Engineering stress-strain curves of NPG with a ligament size of 35 nm measured in air and under potential jumps using standard loading profile.

In order to decouple the effects of deformation-induced displacements and sample actuation, a unique load function profile was proposed for the compression tests, as shown in Fig 5.5 (a). Here, five load-unloading cycles are used, each separated by a switching of the applied potential in the unloaded condition. The 1st, 3rd, and 5th cycles were performed at the potential of -0.2 V, while the 2nd and 4th at the potential of 1.4 V. The corresponding engineering stress-strain curve under potential jumps, and the schematics of the compression process referring to the first three loading cycles are exhibited in Figure 5.5 (b) and (c), respectively. During the first cycle, the displacement grows at the applied constant strain rate until it reaches the set value, holding for 10 s prior to the unloading. After unloading, the flat punch is brought out of contact with the sample surface, and held for 40 s, during which we change the potential, here from off (-0.2 V) to on (1.4 V), allowing the expansion of the sample to occur without putting additional load on the indenter tip. Then, the next loading cycle is applied on the pillar, after that, the flat punch moves away from the sample surface again, followed by the second switching of the potential from off to on and the induced contraction of the sample before the 3rd loading step. Due to the actuation of the whole sample, the displacement of the flat punch at re-contact differs from the last unloading point: during a cycle with the potential at 1.4 V, the indenter contacts the pillar much earlier, i.e. above the last contact point.

The stress-strain curves measured under potential jumps proved that the flow stress of NPG can be tuned reversibly by electrochemical potentials, and the increase of flow stress when the surface of the ligaments changes into an oxidized state is not based on variations of mechanical properties of different micropillars. The observed variation of the flow stress after potential jumps which scales with the actual flow stress at the already applied strain agrees well with the results of macrocompression [57]. The SEM image of the pillar after compression, inset in Figure 5.5 (b), indicate a uniform deformation despite the multiple changes of small length scale and surface state during testing. Additionally, the white particles observed on the pillar surface is the residual NaF crystals that is from the electrolyte, as mentioned in that last section.

We can decouple the actuation effect during compression by means of the multiple unloading profile, but it makes the measured stress-strain curves complicated: there is an overlap or interrupted region between the stress-strain curve of two adjacent cycles, such as the curves for the 1st cycle and the 2nd cycle represented in Figure 5.5 (b). In this case, such curves can not describe the mechanical behaviors of the sample accurately. Therefore, we correct the curve, as shown in Figure 5.6, by moving the starting point of each loading cycle to the ending point of the last cycle, except for the first cycle. After correction, the total strain is larger than

the previous, but it is closer to the real deformation behaviors of pillar. Furthermore, a comparison of the flow stress and its changes with applied potential for both presented approaches, constant potential, and potential jumps show a good agreement, suggesting good reproducibility of these measurements.

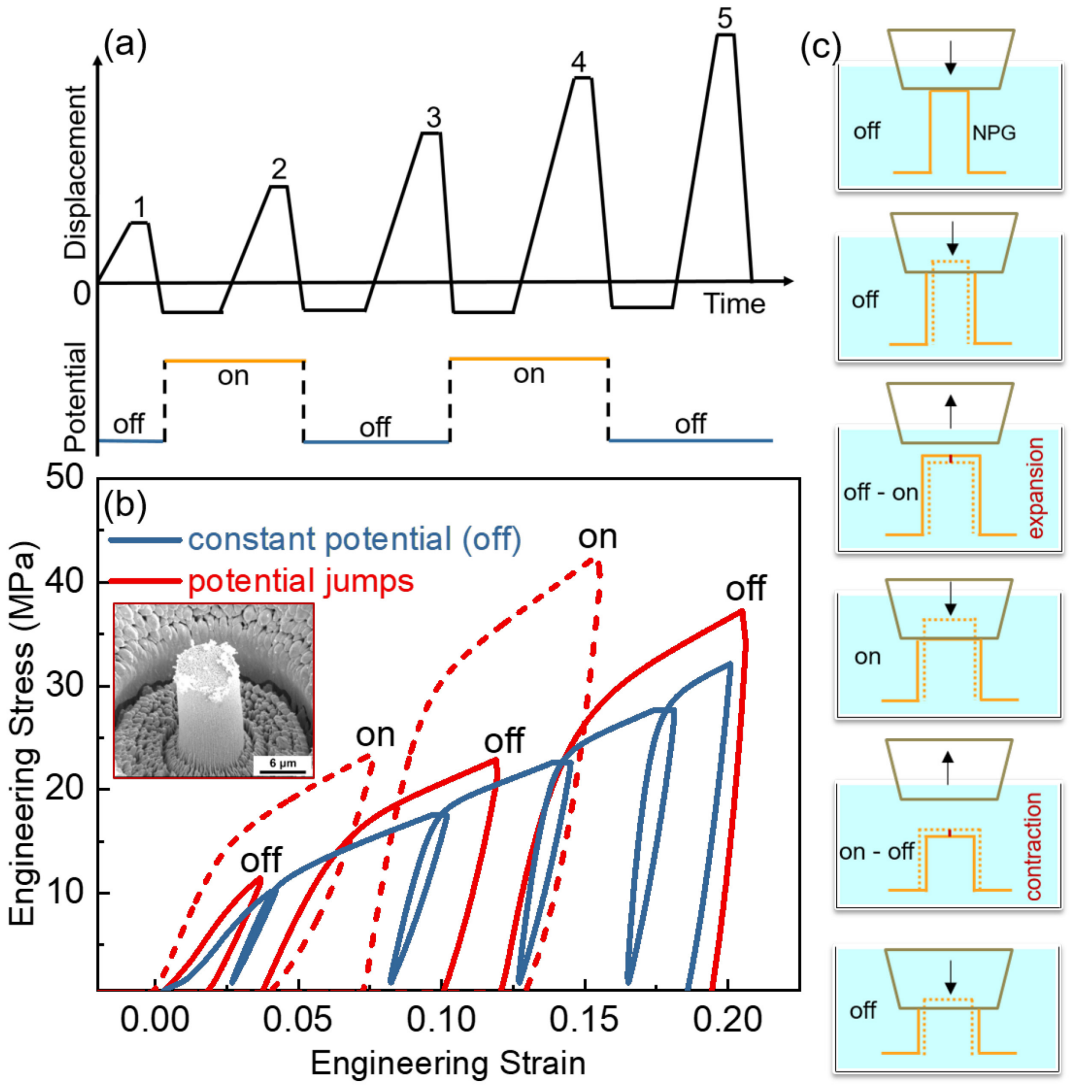

Figure 5.5. Results of *in situ* compression under potential jumps. (a) Applied loading profile. (b) Engineering stress-strain curve of a pillar under potential jumps (starting with clean surface: off-on-off-on-off) and constant potential (-0.2V). The inset is the SEM image of pillar after compression under potential jumps. (c) Schematics of compression process under potential jumps refer to the first three loading cycles.

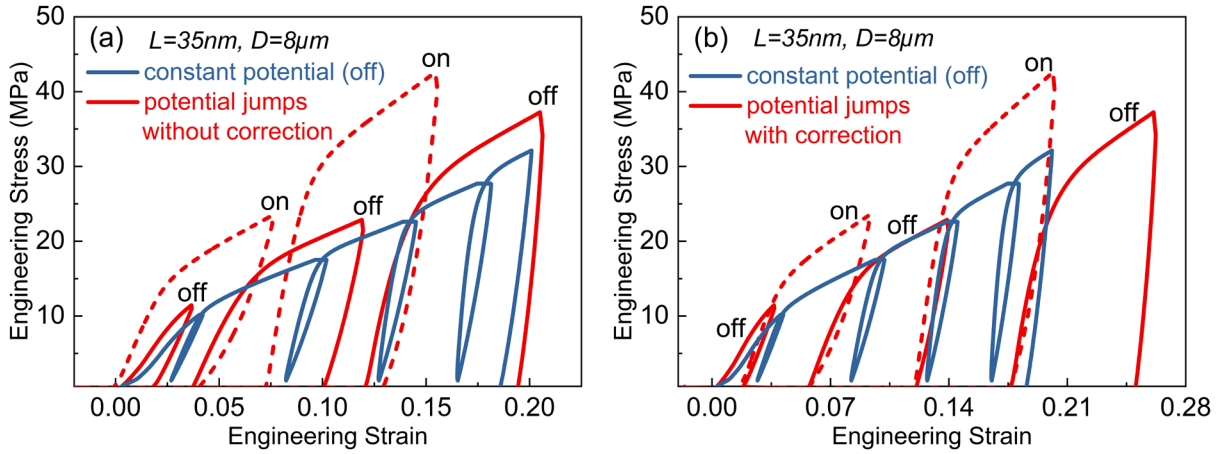

Figure. 5.6. Engineering stress-strain curves of NPG with ligament size of 35 nm measured under potential jumps (a) before and (b) after actuation correction.

5.3 Discussion and conclusion

5.3.1 Discussion

The charging of the surface changes the surface energy, the surface stress, and can cause surface adsorption, which leads to the variation of outer dimensions, i.e. actuation, and mechanical performance of NPG simultaneously. Our results of electro-chemo-mechanical coupling at the microscale reveal that oxidation adsorption on the ligament surface can enhance strength significantly of NPG, and this variation can be tuned reversibly, which is consistent with the corresponding results of bulk NPG [24, 172]. However, the elastic modulus of nanoporous micropillars affected by electrical potential behaves differently: no dependence on the surface coverage, which is different from the behavior of the bulk samples in 1M $HClO_4$ [23]. The sample length scale, electrolyte and loading approach used in [23] is significantly different to that in the present study. The *in situ* compression results of bulk NPG in 0.5M NaF, where the stress-strain curve is measured by a mechanical testing machine and the elastic modulus is calculated from the initial 20% of each unloading curve, as displayed in Figure 5.7 (a) and (b), agrees well with the corresponding results of micron pillars in Figure 5.3 (b). The OH adsorption (1.4 V) enhances the strength while having no evident effect on the elastic modulus. It reveals that a significant influence of the sample size on the change of elastic behavior can be ruled out.

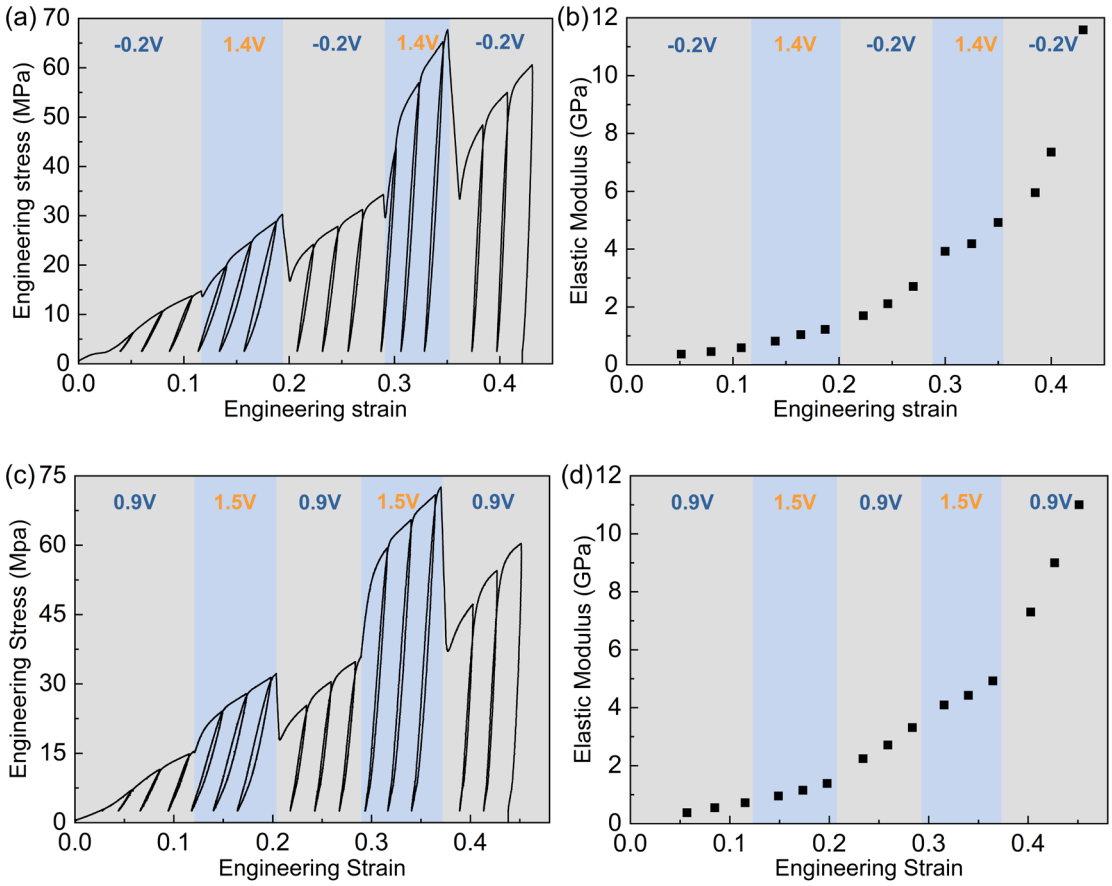

Figure 5.7. Compression results of bulk NPG with ligament size of 35 nm under potential jumps in 0.5M NaF and 1M $HClO_4$, respectively. (a) Engineering stress-strain curve and (b) the variation of elastic modulus calculated from each unloading curve in 0.5M NaF. (c) Engineering stress-strain curve and (d) the variation of elastic modulus calculated from each unloading curve in 1M $HClO_4$.

In addition, the process of electrochemical oxidation of a planar single-crystal Au surface and the effect of specific adsorption of anions (such as SO_4^{2-} and Cl^-) from the electrolyte on the formation of the OH- monolayer has been investigated thoroughly [125, 128, 129]. The F^- and ClO_4^- are two kinds of anions with a strongly bound solvation shell, which induces only weakly specific or even non-specific adsorption at the gold surface when the NPG is positively charged [121]. We expect that the discrepancy of specific adsorption of F^- and ClO_4^- should be weak compared to the formation of an OH monolayer, which dominates the interaction between gold and electrolyte in the oxidation region. In order to clarify whether the anion (F- or ClO_4^-) changes the electro-chemo-mechanical coupling, we carried out macro-compression testing of NPG under potential jumps in 1 M $HClO_4$ (additionally to the ones in NaF) and presented the results in Figure 5.7 (c) and (d). The two potentials 1.5 V (referring to OH^- coverage or oxidized

surface) and 0.9 V (referring to the clean surface) vs. SHE selected here correspond to the maximum and minimum values of elastic modulus from dynamic mechanical analysis (DMA) results, respectively. Yet the elastic modulus shows no obvious variation at these two different surface states, which agrees well with the in situ compression results in 0.5 M NaF.

More likely, this difference might be caused by the different loading protocol, i.e. analyzing unloading sections of the stress-strain curve and DMA testing during which the elastic modulus was measured via analysis of the oscillatory load and displacement signals by a lock-in amplifier while the potential was changed. The load state have a strong influence on the variation of mechanical properties during the change of electrode potential for nanoporous metals [153]. This points to the advantage of this micro-scale test setup which allows the decoupling of the actuation and loading responses.

With decreasing sample size, the fabrication of the samples tends to become more reproducible, i.e. it is considerably easier to fabricate identical and crack-free micropillars than bulk samples in the same conditions [35]. Furthermore, the monolithic NPG with sample size in the range of millimeters size used for macromechanical testing is polycrystalline [24], which is different from pillars with a diameter of 8 μm used here, which can be considered as single crystalline samples since the grain size of the master alloy is around 20~30 μm. The position of each pillar on the polycrystalline NPG is selected randomly and tens of pillars are fabricated on one disc-shaped sample, thus the crystal orientation of each pillar might be different. In order to explore the crystal orientation effect, we produced several pillars of NPG in specific crystals which were identified by electron backscatter diffraction (EBSD) of the master alloy, as shown in Figure 5.8 (a), since the sample retains its crystalline orientation structure during dealloying [176]. Microcompression of these pillars was carried out in an electrochemical environment under potential jumps using a multiple load-unloading profile as displayed in Figure 5.5 (a). It was found that the stress-strain curves of pillars with (111) and (101) orientation, as exhibited in Figure 5.8 (b), are identical, suggesting plastic behavior coupled with potentials is not sensitive to these two crystal orientations. This is not surprising, because of the existence of a large number of slip systems in face-centered cubic (FCC) metals, such as Au [57] and Cu [189]. Moreover, the NPG micropillars even offer additional deformation modes, most prominent ligament bending, which even further randomizes the orientation of the plastic processes.

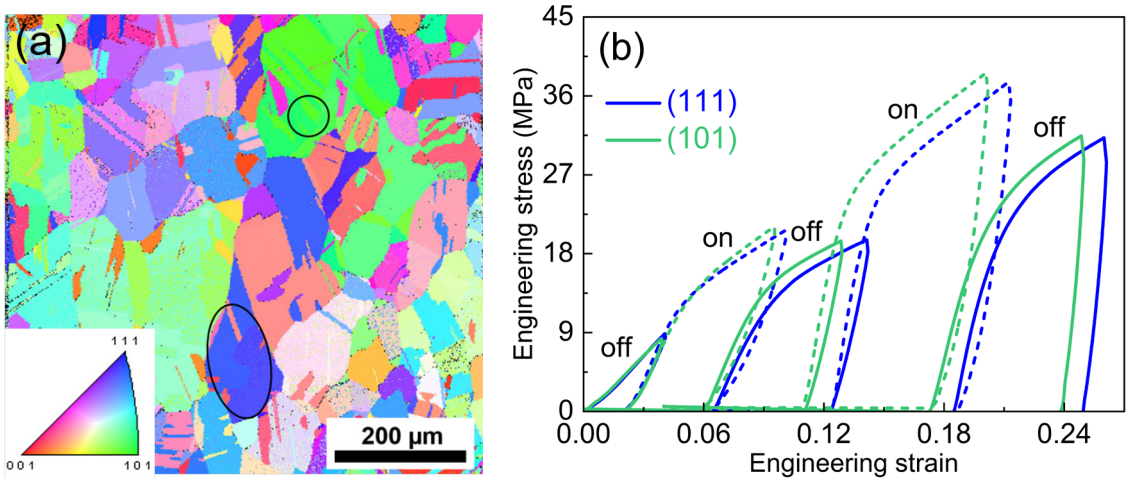

Figure 5.8. *In situ* compression behaviors of micropillars (ligament size: *L=35 nm*, diameter: *D=4µm*, *α=D/L=114*) with different crystal orientations under potential jumps. (a) Electron Backscattering Diffraction (EBSD) orientation map of $Ag_{25}Au_{75}$ master alloy before dealloying. (b) Engineering stress-strain curves of pillars with (101) and (111) orientation measured under potential jumps.

5.3.2 Conclusion

The first microcompression of NPG *in situ* in electrolyte and under potentials control was carried out and described in the current chapter, which provides opportunities to investigate the influence of microstructural aspects and sample size on the electro-chemo-mechanical coupling. By means of a multiple load-unloading profile, we are able to decouple the actuation effect from the impact of elastic strain when potential changes. The *in situ* compression results reveal that the strength of a NPG pillar can be improved significantly with the OH monolayer coverage on ligament surface and this variation is found to be reversible under potential jumps control, which is in agreement with the corresponding behavior of bulk NPG. However, the elastic modulus was found to be insensitive to the surface state, inconsistent with the bulk dynamic mechanical analysis (DMA) results. The reason for this discrepancy is still not fully understood.

6 Intrinsic and extrinsic size effects, and the influence of the deformation history on electro-chemo-mechanical coupling of NPG

Both microstructural length-scale (intrinsic size) and deformation length-scale (extrinsic size) of NPG exhibit significant influence on mechanical behavior even without application of an electrochemical environment, as confirmed in Chapter 4. In addition, in Chapter 5, the electro-chemo-mechanical coupling measurement on NPG at the microscale was achieved successfully using a modified indenter and a novel loading profile. The plastic response under potential control is consistent with the corresponding macroscopic results. Inspired by the results obtained in these two chapters, the focus now lies on the effects of ligament size and sample diameter of NPG pillars on the flow stress coupled with electrochemical potentials via *in situ* microcompression testing. The corresponding results are then compared with the results of size effects without potential application, as shown in Chapter 4, which helps us further understand the correlations between structure, chemical states and mechanical behaviors. The impact of deformation history with a clean surface on the subsequent flow stress with surface oxidation adsorption is also studied in this chapter.

6.1 Intrinsic and extrinsic size effects on the electro-chemo-mechanical coupling

As mentioned in Chapter 5.2.2, disc-shaped bulk NPG samples, rather than cylindrical samples used in Chapter 4, were used for the pillar fabrication for the testing of electro-chemo-mechanical coupling, in order to reduce the actuation of the substrate that has a significant influence on the displacement measurement of pillars. In this chapter, in addition to the disc-shaped samples, pillars are also milled on the NPG thin films, where the substrate of the pillar is massive Au rather than a porous structure. The information regarding all the pillars used in this chapter is illustrated in Table. 3.2.

6.1.1 *In situ* microcompression of pillars fabricated on the disc-shaped NPG

Pillars, with a diameter of 8 μm and 4 μm, as shown in Figure 6.1, were machined on disc-shaped NPG samples with a ligament size of 35, 150 and 300 nm, where the ratio (α) of pillar diameter to ligament size ranges between 228 and 13. Then they were compressed at 0.001/s constant strain rate under potential jumps in 0.5 M NaF aqueous solution, using the multiple load-unloading cycles that is the same as the loading profile in the last chapter, as displayed in Figure 6.2 (a), and "off" and "on" refer to clean and OH covered surface state.

The *in situ* compression results of pillars with the same diameter of 8 μm but different ligament size are displayed in Figure 6.2 (b)-(e). As can be seen, engineering stress-strain curves show the same variation trend in response to potential jumps, a considerable increase in strength with OH adsorption and reversible changes with altering surface conditions. However, the overall strength decreases considerably with ligament size increasing from 35 to 300 nm, in agreement with the compression results without electrochemical environment in chapter 4. Furthermore, in order to address the effect of ligament size on the variation of flow stress induced by oxidation adsorption, we calculate the relative change of flow stress induced by electrode potential variation ($\Delta\sigma/\sigma_{off} = (\sigma_{on} - \sigma_{off})/\sigma_{off}$), as shown in Figure 6.2(b), it determined as a change of flow stress for potential switching from off to on normalized by σ_{off}. The $\Delta\sigma/\sigma_{off}$ as a function of ligament size are plotted in Figure 6.2 (e). It is seen that the relative variation of stress shows strong dependence on the ligament size, it decreases from 33.4% to 10.24% at a strain $\varepsilon=0.07$ as the ligament coarsens from 35 to 300 nm. This might be attributed to the significant decrease of the specific surface area of NPG with increasing ligament size that results in the reduction of OH coverage thus weaken the interface effects.

Apart from that, *in situ* compression results of pillars with different diameter, where $\alpha=D/L$ ranges from 228 to 13, are illustrated in Figure 6.3. No obvious variation on stress-strain curves shown in Figure 6.3 (a)-(d) was observed when the ligament size is the same, either 35 or 300 nm. The reduction of pillar diameter from 8 to 4 μm has no influence on flow stress coupled with potential jumps. Furthermore, the results for relative variation of flow stress induced by surface adsorption ($\Delta\sigma/\sigma_{off}$) calculated based on the stress-strain curve shown in Fig 6.3 (a)-(d) as a function of α at the strain $\varepsilon=0.17$ was shown in Figure 6.2 (e). It further confirms this point: $\Delta\sigma/\sigma_{off}$ is not sensitive to the reduction of pillar diameter even though α varies from 26 to 13.

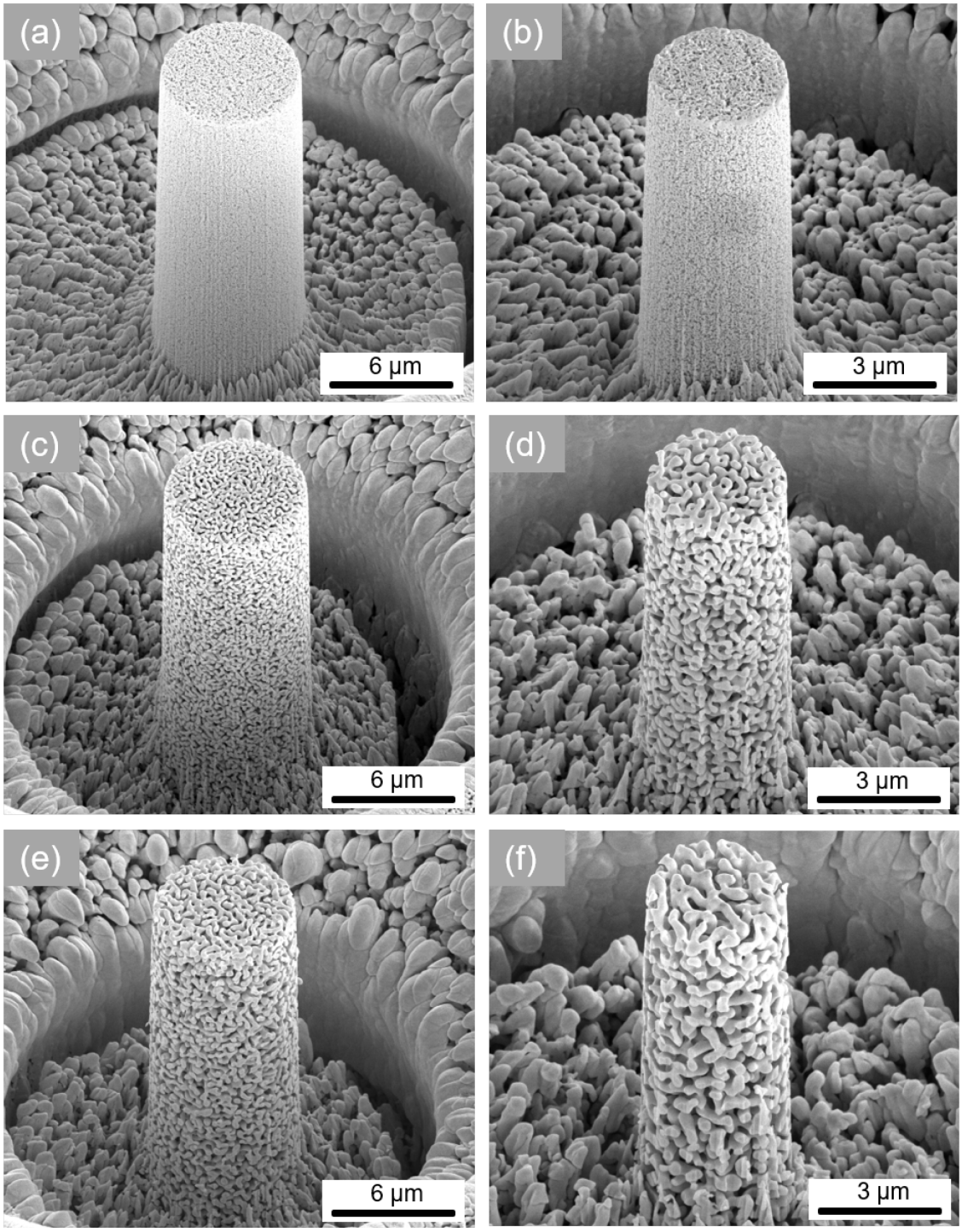

Figure 6.1. Micropillars (fabricated from disc-shaped NPG samples) with varying ratio (α) of pillar diameter (D) and ligament size (L). (a) *D=8 µm, L=35 nm, α=228.* (b) *D=4 µm, L=35 nm, α=114.* (c) *D=8 µm, L=150 nm, α=53.* (d) *D=4 µm, L=150 nm, α=26.* (e) *D=8 µm, L=300 nm, α=27.* (f) *D=4 µm, L=300 nm, α=13.*

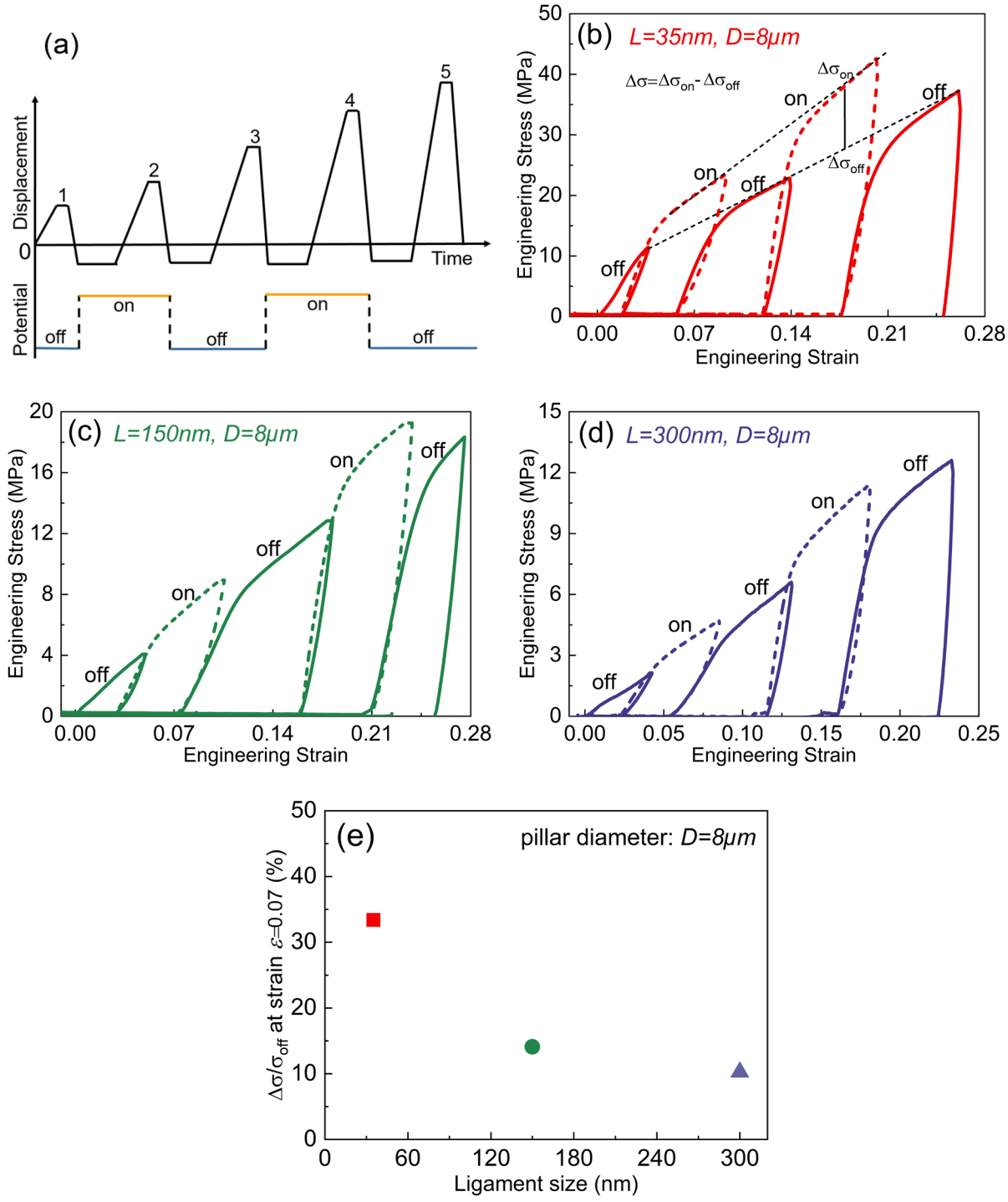

Figure 6.2. Compression results of pillars with the same diameter of 8 μm but varying ligament size under potential jumps. (a) Multiple loading profile, potential on and off refer to 1.4V and -0.2V, respectively. (b)-(d) Engineering stress-strain curves of pillars with ligament size of 35, 150 and 300 nm, respectively. (e) Relative variation of flow stress ($\Delta\sigma/\sigma_{off}$) induced by electrode potential variation (here mainly due to adsorption) at strain $\varepsilon=0.17$ as a function of ligament size.

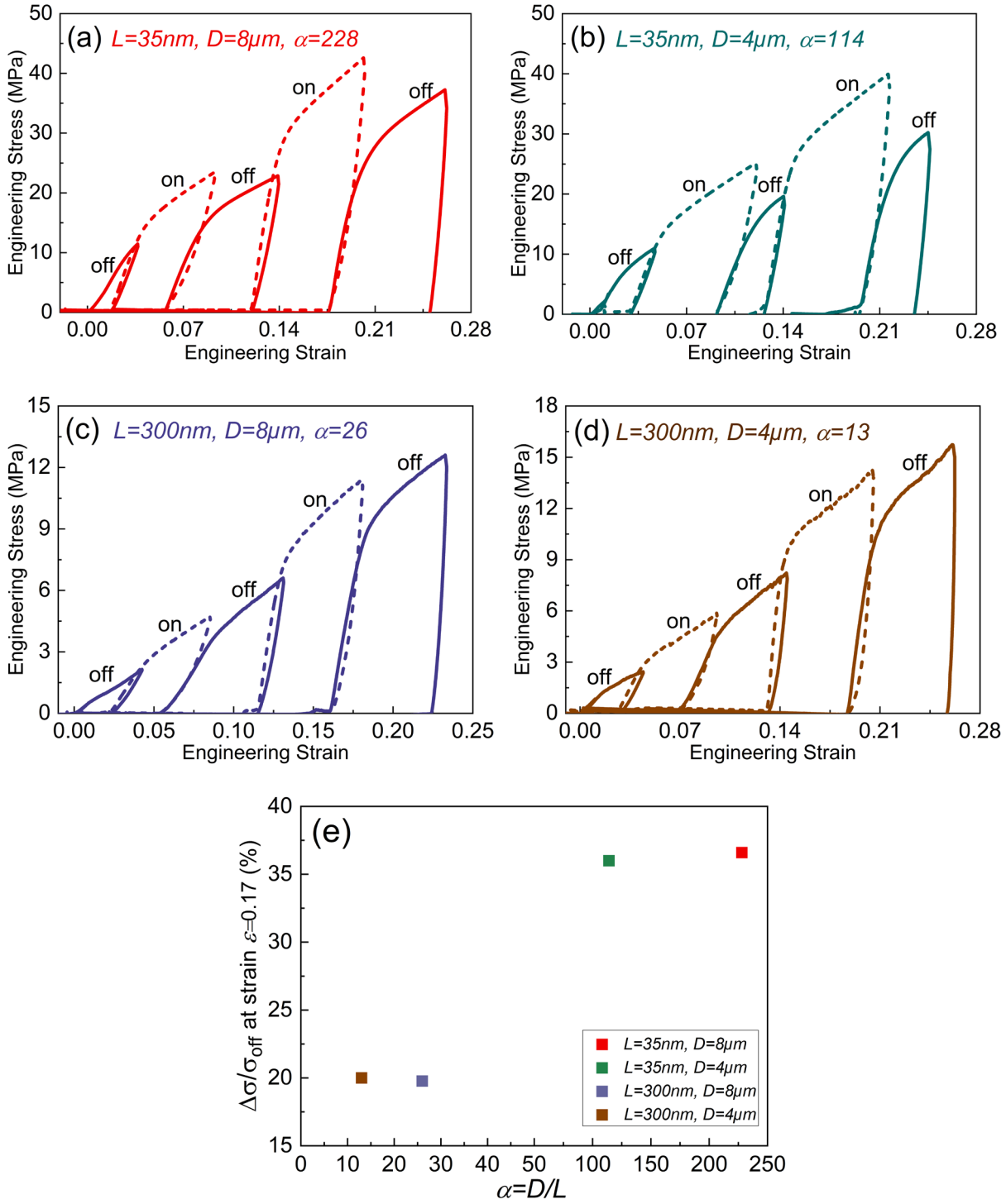

Figure 6.3. Compression results of pillars with the different ratios (α) of pillar diameter (D) to ligament size (L) under potential jumps. (a)-(d) Engineering stress-strain curves of pillars with α of 228 (L=*35 nm, D= 8μm*), 114 (L=*35 nm, D= 4μm*), 26 (L=*300 nm, D= 8μm*) and 23 L=*300 nm, D= 4μm*), respectively. (e) Relative variation of flow stress induced by electrode potential variation ($\Delta\sigma/\sigma_{off}$) of pillars at strain ε=*0.17* as a function of α. Details of the calculation is examplized in Figure 6.2 (b).

It should be noted here that the load is not constant in the period of displacement holding between two loading cycles where the flat punch does not contact the sample, due to the load limitation of the nanoindenter system (Bruker) used here. The variation of load over holding can be neglected compared to the compression load working on the pillars with a diameter larger than 4 µm, but it affects considerably the load measurement when the diameter decreases to 2 µm or even smaller, as shown in Figure 6.4, where the change of load during the holding region is comparable to the measured load. Therefore, in order to further explore the external sample size effect, the electro-chemo-mechanical measurement of smaller volumes will be carried out on pillars fabricated on NPG thin films, which will be described in the following section.

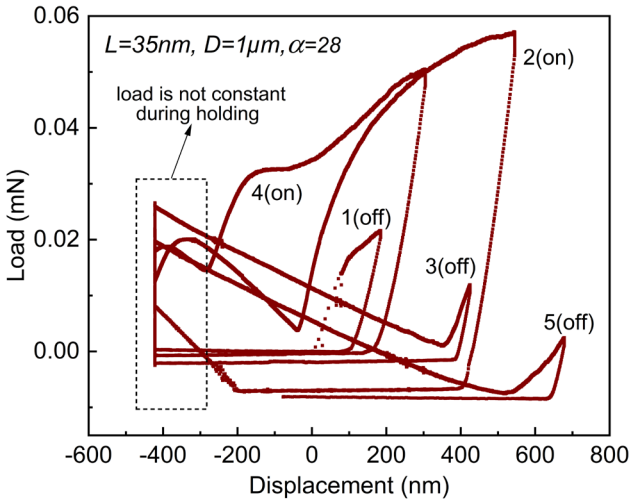

Figure 6.4. A load-displacement curve of a pillar with a ligament size (L) of 35 nm and diameter of 1 µm (D) measured under potential jumps, using the multiple load-unloading profile shown in Figure 6.2 (a).

6.1.2 *In situ* microcompression on pillars fabricated on NPG thin films

Due to the limitation of the multiple load-unloading profile for the pillars with diameter lower than 2 µm, as described in the last section, pillars fabricated on NPG thin films with a thickness of 2.5 µm were used in this section to further investigate the impact of pillar diameter on the electro-chemo-mechanical coupling. The ligament size of NPG thin films is 25 and 200 nm, and the corresponding synthesis processes can be found in Chapter 3.2.2.

Micropillars with a diameter of 8, 2.5 and 1.5 µm were machined on NPG thin films with ligament size of 25 and 200 nm, where the ratio (α) of pillar diameter (D) to ligament size (L) varies from 100 to 7.5. SEM images of these pillars are shown in Figure 6.5. Apparently, the

substrate material of all pillars has been exposed after cutting, and the base of the pillars can be observed clearly, which helps us measure the height of the pillars accurately. As can be seen, the amount of ligaments contained in a pillar decreases considerably with decreasing α. The height of all pillars is equal to the thickness of the NPG film (~ 2.5 μm), leading to the aspect ratio of height to pillar diameter of these pillars varies from 0.3 to 1.67, lower than the corresponding ratio (~3) of pillars cut from bulk NPG samples. The low aspect ratio will increase the possibility of barreling during deformation if the friction between the pillar and the substrate is high. Since the substrate material is pure massive Au rather than NPG, there is no significant actuation effect from the substrate when the potential changes, neither from off to on or from on to off, different from the pillars machined on the bulk NPG samples, as shown in Figure 6.1. In this case, the electro-chemo-mechanical coupling of such small pillars can be measured via a single load-unloading function, as shown in Figure 6.6 (a), where the flat punch stays in contact with the pillar surface over the whole compression testing, i.e. no unloading and holding periods during testing, which avoids load fluctuations induced by the nanoindentation system that affect the measurements.

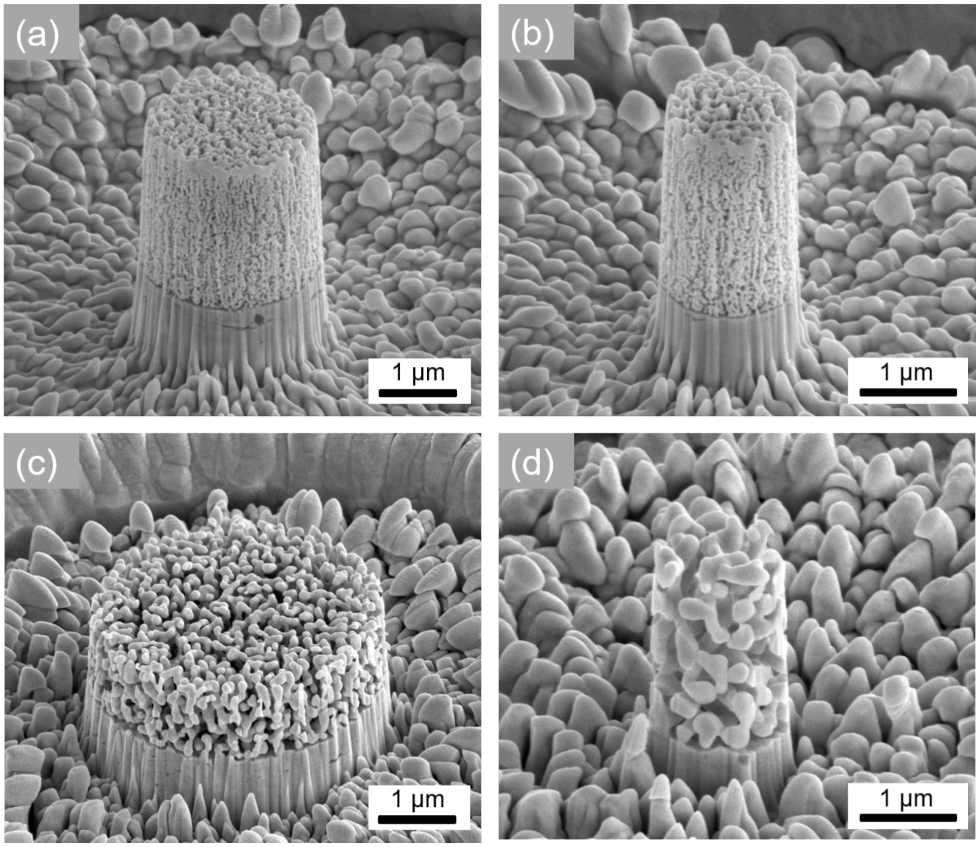

Figure 6.5. SEM images of pillars with different ratio (α) of pillar diameter (D) to ligament size (L) fabricated in NPG films. (a) *D=2.5 μm, L=25 nm, α=100*. (b) *D=1.5 μm, L=25 nm, α=60.* (c) *D=8 μm, L=200 nm, α=40*. (d) *D=1.5 μm, L=200 nm, α=7.5*

Compressive stress-strain curves of pillars (ligament size: 25 nm) with a diameter of 2.5 µm measured in 0.5 M NaF under electrochemical potential control were illustrated in Figure 6.6 (b). Apparently, the flow stress coupled with potential jumps shows the same variation trend as the pillars fabricated in disc-shaped NPG samples, as shown in Figure 6.3. It can be enhanced by OH adsorption and be tuned reversibly by potential jumps, suggesting that the network structure of NPG films is similar to that of disc-shaped NPG samples in terms of electro-chemo-mechanical coupling, even though the master alloys are prepared by different techniques, as described in Chapter 3.2, and the thickness of the thin film was decreased to only several micrometers. The yielding transition on the stress-strain curves is obvious, and the average yield strength, represented by the strength at 2% strain, is around 38 MPa. As expected, the hysteresis observed in flow stress at the switching points of potentials is very weak due to the missing actuation from the substrate material, which consequently does not affect the mechanical measurement on such small pillars. Additionally, the stress measured under potential jumps and low constant potential agrees well, confirming the high reproducibility also of these measurements.

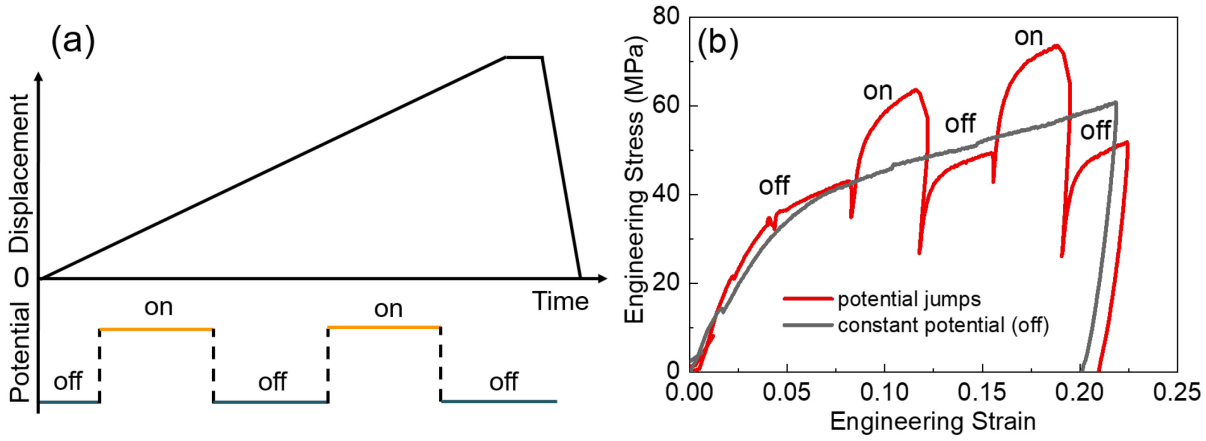

Figure 6.6. (a) A single load-unloading profile using for *in situ* compression testing of pillars fabricated in NPG films. (b) Engineering stress-strain curves of pillars with a diameter of 2.5 µm and ligament size of 25 nm measured under electrochemical potential control.

The *in situ* compression results of pillars with different ligament size (L) and diameter (D) are reported in Figure 6.7, where the ratio $\alpha=D/L$ varies from 100 to 7.5. All of the stress-strain curves show a reversible response to potential jumps. Comparing the stress-strain curves shown in Figure 6.7 (a)-(d), it is found that increasing the ligament size leads to a weakening in strength, in agreement with the corresponding results of pillars fabricated on disc-shaped

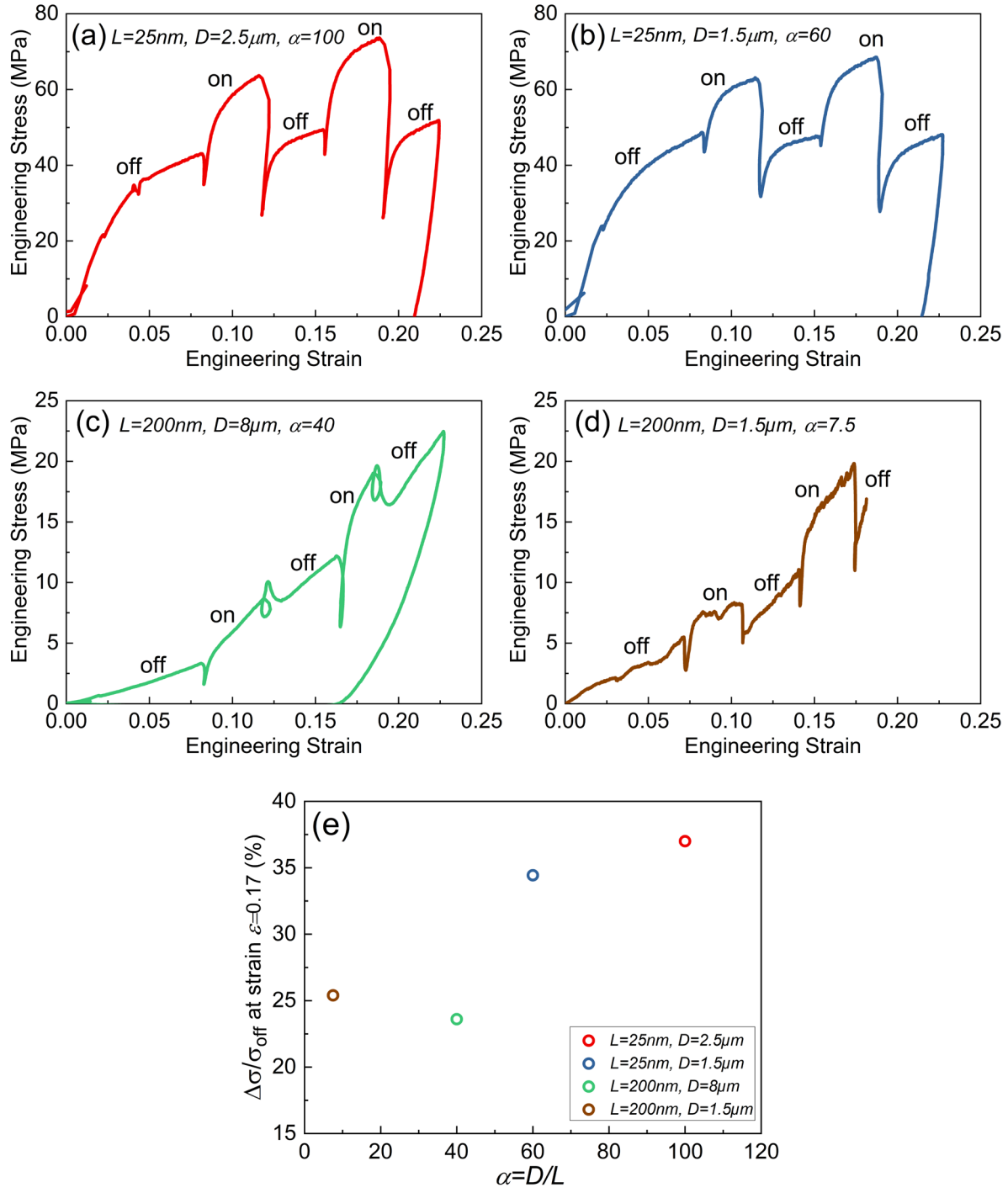

Figure 6.7. *In situ* compression results of pillars with different ratio (α) of pillar diameter (D) to ligament size (L). Engineering stress-strain curves measured under potential jumps of pillars with (a) D=2.5 μm, L=25 nm, α=100. (b) D=1.5 μm, L=25 nm, α=60. (c) D=8 μm, L=200 nm, α=40. (d) D=1.5 μm, L=200 nm, α=75. (e) Relative change of flow stress caused by electrode potential variation ($\Delta\sigma/\sigma_{off}$) at strain ε=0.17 as a function of α calculated from stress-strain curves. Details of the calculation is examplized in Figure 6.2 (b).

samples, as shown in Figure 6.3. Furthermore, based on the results of relative change in flow stress induced by OH adsorption ($\Delta\sigma/\sigma_{off}$) shown in Figure 6.7 (e), a calculation example of which can be found in Figure 6.2 (b), $\Delta\sigma/\sigma_{off}$ also exhibits dependence on ligament size, and it decreases from 38% to 25% at strain ε=*0.17*, as ligament size increases from 25 to 200 nm. However, it seems that $\Delta\sigma/\sigma_{off}$ of pillars fabricated from the same film (i.e. the same ligament size) is almost identical. This implies that the reduction of pillar diameter from 8 to 1.5 μm, where α varies from 100 to 7.5, has no obvious influence on $\Delta\sigma/\sigma_{off}$ for a fixed ligament size, consistent with the results displayed in Figure 6.3 where pillars were fabricated out of monolithic disc-shaped samples.

6.2 Effect of deformation history

During compression testing, NPG ligaments tend to touch each other as plastic deformation proceeds, resulting in a densification of the nanoporous structure, which leads to an increase in solid fraction. Apart from that, the structural geometry will also be changed to some extent after deformation. In the case of microcompression *in situ* in an electrolyte under potential jumps as carried out in the last section, pillars underwent deformation where the surface state was altered several times during testing. From stress-strain curves plotted in Figure 6.3, in which the electro-chemo-mechanical coupling measured using a multiple load-unloading profile, it can be seen that the amount of the plastic strain of a pillar at the 1st cycle is different from each other. Furthermore, due to actuation and system hysteresis, it is hard to make sure that all pillars experience identical initial deformation before we change potentials in experiments. Because the different amount of plastic deformation could cause a different degree of variation in the network structure, the structural discrepancy caused by the history deformation could affect the subsequent change of flow stress coupled with surface oxidation. In order to address this, the plastic behavior of NPG under potential jumps, where samples experience varying deformation at the first stage, are measured and analyzed in this section.

Here, two disc-shaped NPG samples with ligament size of 35 and 300 nm were selected to represent fine and coarse network structures, respectively. As experimental parameters illustrated in Table. 6.1, a set of pillars with the same diameter of 8 μm fabricated from the same bulk NPG samples were first compressed to 5%, 10%, and 15%, respectively, at a constant potential of -0.2 V (off). After unloading, the applied potential was changed to 1.4 V (on) and then the corresponding pillars were continuously compressed by additional 13%, 8% and 3%, respectively, to ensure a total strain of 18% for each pillar.

The corrected engineering stress-strain curves where the starting points of the 2nd cycle have been moved to the ending points of the 1st cycle are shown in Figure 6.8. Although the total compressive strain for each pillar we choose is around 18%, it seems to increase as the deformation strain at the 1st cycle increases. That discrepancy is because the hysteresis between the two loading cycles increases with increasing strain. Apparently, the flow stress with potential on, given in Figure 6.8 (a), reaches a good agreement in all cases, no matter how much deformation the pillars experience previously under potential off, indicating that stress coupled oxidation adsorption shows no dependence on the deformation history. Furthermore, the response of flow stress to the potential jumps in the coarse structure, in Figure 6.8. (b), exhibits an identical trend, although the strength and its variation induced by OH adsorption are weaker due to the increase of ligament size.

Table 6.1. Experimental parameters of microcompression under potential jumps

Ligament size	Loading cycles	Compression strain		
		Pillar 1	Pillar 2	Pillar3
35 nm	1st cycle (off) 2nd cycle (on)	5% 13%	10% 8%	15% 3%
300 nm	1st cycle (off) 2nd cycle (on)	5% 13%	10% 8%	15% 3%

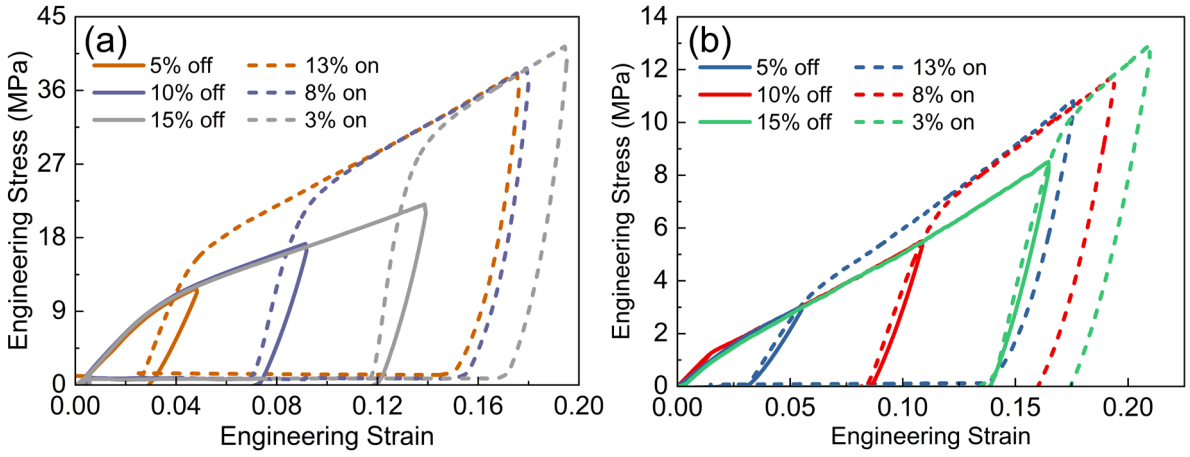

Figure 6.8. Engineering stress-strain curves of pillars with ligament size of (a) 35 nm and (b) 300 nm measured under potential jumps using the experimental parameters illustrated in Table. 6.1.

6.3 Discussion and conclusion

6.3.1 Discussion

As mentioned at the beginning of this chapter, NPG pillars used for investigating microstructural length-scale and deformation length-scale effects on the electro-chemo-mechanical coupling are fabricated from different types of samples, disc-shaped NPG (the same samples used in the Chapter 5) and NPG thin films. Master alloys and the synthesis methods of these two types of samples are different, details of which can be found in Chapter 3.2.

Based on the compressive stress-strain curves of NPG pillars with varying ligament size (L) and diameter (D) fabricated from the disc-shaped samples and the thin films under potential jumps, as shown in Figure 6.3 and Figure 6.7, the strength (σ_{off}) of pillars with high $\alpha=D/L$ measured at potential off, as well as its absolute ($\Delta\sigma = \sigma_{on} - \sigma_{off}$) and relative ($\Delta\sigma/\sigma_{off}$) variations induced by potential change from off to on, i.e. the surface varies from clean to OH-covered states, as a function of L for a fixed strain $\varepsilon=0.17$ are summarized in Figure 6.9. As expected, ligament size has significant influence on the σ_{off} of pillars machined from the same type of samples, coarsening ligament structure leading to a decrease in σ_{off}, as shown in Figure 6.9 (a). However, pillars with similar L but fabricated from different type of samples show a considerable difference in σ_{off}; the σ_{off} (~52 MPa) of pillars with $L=25$ *nm* fabricated on thin films, shows twice the corresponding strength (~26 MPa) of pillars machined on disc-shaped samples. In addition to the effects of ligament size, other influences in terms of the microstructure and geometry of the pillars are needed to be considered, to explain this large discrepancy, since the master alloy of these two types of pillars is different. First, numerous grain boundaries, which might come from the fine grains of the master alloy, observed on the SEM images of NPG thin films, as displayed in Fig 3.7, might have a contribution on the higher strength via hindering the dislocations movement during deformation [190]. Second, the aspect ratios (0.3~1.67) of pillars obtained from thin films is much lower than the corresponding ratio (~3) of pillars fabricated in disc-shaped samples, as mentioned in section 6.1.2. The low aspect ratio will cause an increase in friction coefficients between the pillar and substrate [191]. This might resist the transversal deformation of pillars during compression, thus more load is required to be applied on the samples. However, since the Poisson's ratio of NPG was found to be close to zero in other studies [65, 115, 192], the effect of aspect ratio on the strength of NPG might not be as strong as for conventional massive metals. Additionally, the solid fraction and

the connectivity density of these two pillars might be different, which could also lead to a variation in σ_{off}.

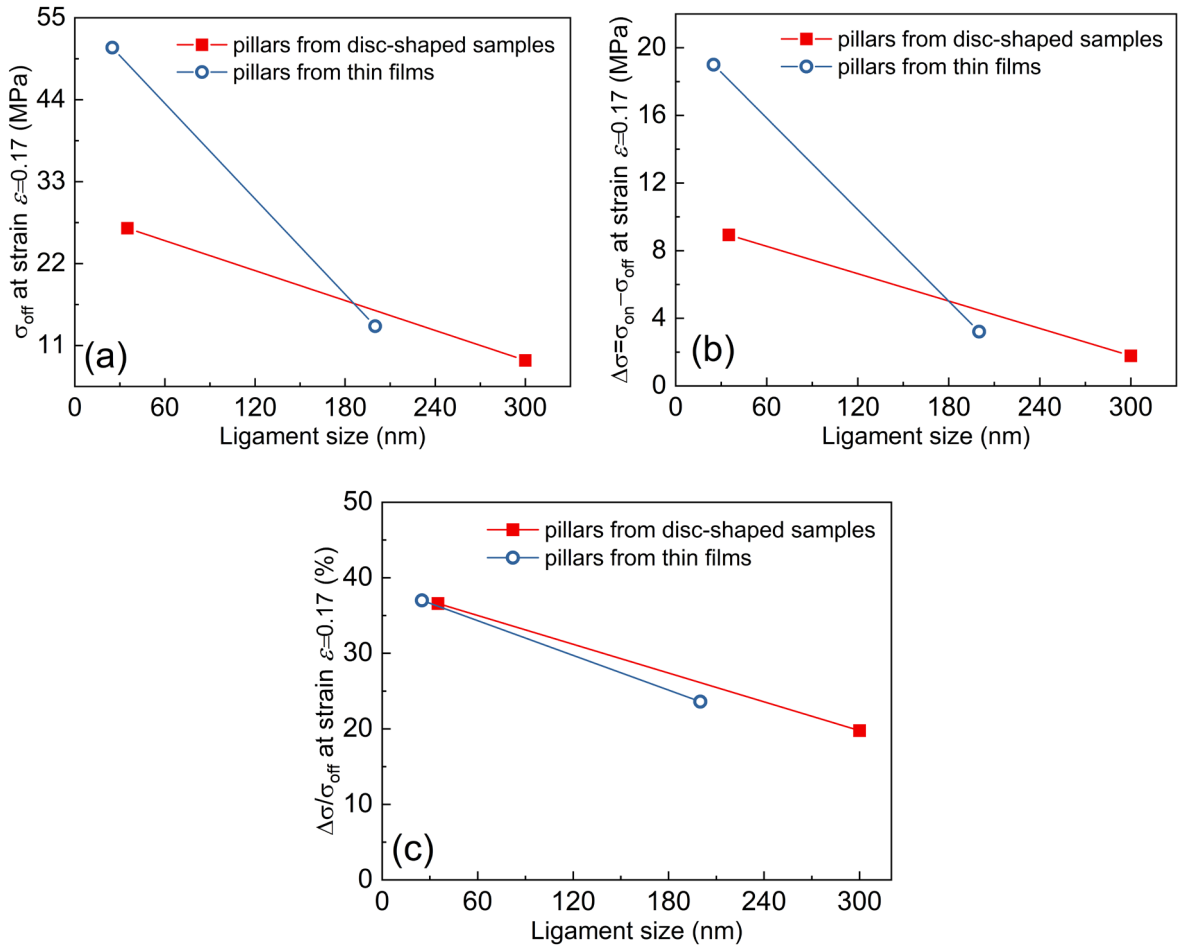

Figure 6.9. (a) The strength (σ_{off}) of NPG pillars, fabricated from disc-shaped and film samples, with high α=D/L measured at potential off, as well as its (b) absolute ($\Delta\sigma = \sigma_{on} - \sigma_{off}$) and (c) relative ($\Delta\sigma/\sigma_{off}$) variations induced by potential change from off to on, i.e. the surface varies from clean to OH-covered states, as a function of ligament size (L) for a fixed strain ε=*0.17*.The lines are simply given as a guide to the eye.

The absolute change of strength ($\Delta\sigma$) during surface coverage of OH, is also dependent on the ligament size, as shown in Fig 6.9 (b); increasing the ligament size of the pillars from the same type of samples (i.e., thin film or bulk disc-shaped) results in a significant decrease in $\Delta\sigma$. The improvement of strength with surface oxidation adsorption is attributed to the surface effects controlled by electrochemical potentials, such as a decrease of surface tension and dislocation movement pinned by adsorbed species [24]. Ligament structure coarsening leads to

a reduction of specific surface area, which will weaken the interaction between the Au surface and electrolyte, as well as surface effects, resulting in a decrease in $\Delta\sigma$. Additionally, comparing the results presented in Figure 6.9 (a) and Figure 6.9 (b), it is found that $\Delta\sigma$ seems to scale with the σ_{off}; the higher σ_{off} can induce a larger $\Delta\sigma$ for pillars with similar ligament size, implying that the difference in microstructure of disc-shaped samples and films we discussed above might have an impact on the $\Delta\sigma$.

In order to further clarify the interdependencies of σ_{off}, $\Delta\sigma$ and L, we plotted the corresponding relative variation of strength ($\Delta\sigma/\sigma_{off}$) as a function of ligament size, as presented in Figure 6.9 (c). $\Delta\sigma/\sigma_{off}$ of pillars fabricated from two types of samples exhibits the same dependence on the ligament size, decreasing with increasing L, implying that the dependence of ligament size on σ_{off} and the $\Delta\sigma$ is in a different manner, either for disc-shaped samples or for thin films. Furthermore, the nearly identical values of $\Delta\sigma/\sigma_{off}$ between pillars with *L=25* nm and *L=35 nm* coming from different type of samples further verify that the $\Delta\sigma$ scales with the σ_{off}.

In addition to the ligament size, the $\Delta\sigma/\sigma_{off}$ of pillars as a function of α *=D/L* are summarized in Figure 6.10, where α varies from 228 to 7.5. It is found that $\Delta\sigma/\sigma_{off}$ remains nearly constant when ligament size is invariant, even though α decreases to 7.5, indicating that a variation of pillar diameter in this certain range for a fixed ligament size has no significant influence on the electro-chemo-mechanical coupling. That is different from the results of compression behavior of NPG pillars without an electrochemical environment, as shown in Fig 4.6, where the mechanical behavior is insensitive to the pillar diameter when $\alpha \geq 20$, while for $\alpha < 20$ both strength and elastic modulus of pillars with a ligament size of 350 nm decreased with the lower pillar diameter. This variation is attributed to the reduction in connectivity density and ligament size distribution contributing to the mechanical behavior of NPG, as discussed in Chapter 4.3.1. However, the electro-chemo-mechanical coupling of NPG is governed by the specific surface area of the sample rather than the connectivity density, thus no size-dependence on functional behavior was observed, as shown in Figure 6.10.

Due to the heterogeneity of the ligament structure, the distribution of adsorbates on the individual ligament surface is not homogeneous, i.e. adsorption might occur preferentially on some local surface structure, depending on the geometries (shape, curvature) and the strain of the ligaments [174]. This local inhomogeneity can be neglected for pillars with high α, resulting in reproducible functional behavior, verified by the results shown in Figure 6.10, while for

pillars with low α, especially only few ligaments involved, it might become a dominant factor in effecting electro-chemo-mechanical coupling, leading to stochastic functional behaviors. In addition, the ligament size of pillars with low α might differ, even though they are milled from the same sample, since the ligament size distribution of NPG is broad [114], which could also cause stochastic responses in $\Delta\sigma/\sigma_{off}$. Therefore, we expect that the existence of a critical α, above which the tested volume can be considered a representative volume element (RVE) resulting in reproducible electro-chemo-mechanical coupling, is similar to the corresponding RVE in terms of mechanical behavior as described in Chapter 4.3.1. This critical ratio is thought to be independent on ligament size if the network structure remains self-similar. Due to the limit of the nanoindentation system and sample preparation method, as mentioned in Chapter 3.2.2 and 3.3.3, α=*7.5* is the minimal ratio of pillars we can test here, and the corresponding $\Delta\sigma/\sigma_{off}$ of such pillars is nearly identical to that of pillars with high α=*40* for a fixed ligament size (*L=200nm*), as shown in Figure 6.10. This implies that the critical size of RVE in terms of the functional behavior is lower than 10 times the corresponding ligament size, smaller than the corresponding size of RVE with regard to the mechanical behavior that is around 20 times the ligament size, as described in Chapter 4.

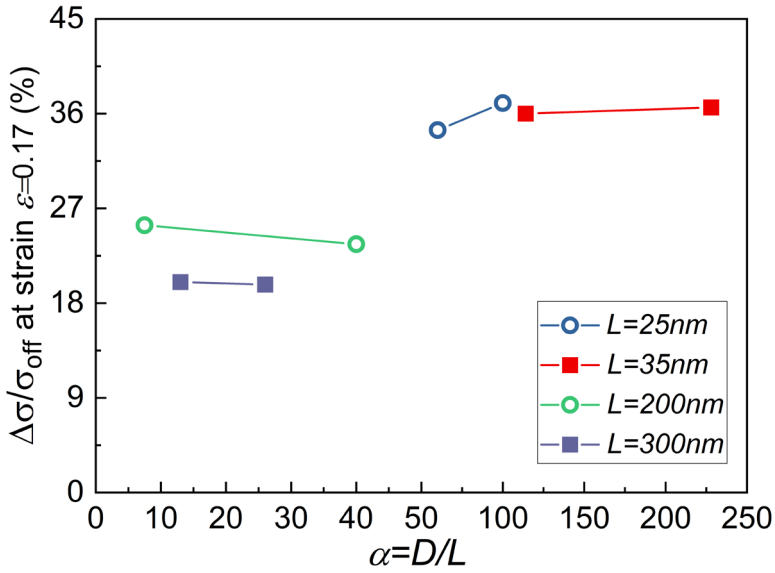

Figure 6.10. The relative variation of flow stress induced by electrode potential variation ($\Delta\sigma/\sigma_{off}$) of pillars at strain ε=*0.17* with varying ratio (α) of ligament size (L) and pillar diameter (D). Data are collected from Figure 6.3 (e) and Figure 6.7 (e). Solid square symbols: pillars fabricated from disc-shaped NPG samples. Cycle symbols: pillars fabricated from NPG films.

6.3.2 Conclusion

In this chapter, the influence of intrinsic and extrinsic size, as well as deformation history on the electro-chemo-mechanical coupling of NPG were studied via microcompression *in situ* in an electrolyte. The engineering stress-strain curves of pillars with varying ligament size (L) and diameter (D), fabricated on disc-shaped NPG samples and NPG films, where $\alpha=D/L$ ranges from 228 to 7.5, revealed that the flow stress (σ_{off}), as well as its absolute ($\Delta\sigma$) and relative ($\Delta\sigma/\sigma_{off}$) changes induced by surface adsorption strongly depends on the ligament size. All of them decrease significantly with increasing ligament size, but in different ways. The first is arising from size effects of "smaller is stronger", while the latter two is owing to the decrease of specific surface area as the structure coarsens. Furthermore, the $\Delta\sigma$ also scales with the σ_{off}. However, it was found that a variation of pillar diameter does not affect $\Delta\sigma/\sigma_{off}$ if the pillars are machined from the same type of sample with a fixed ligament size, even though α is reduced to 7.5. This implies that the size of the RVE in terms of functional behavior is lower than 7.5 times the corresponding ligament size, smaller than the corresponding size (20 times the ligament size) of RVE regarding the mechanical response without electrolyte, as described in Chapter 4. In addition, the results of *in situ* compression testing, where pillars with fine and coarsened structures experienced different amount of plastic deformation before potential changes, indicated that the deformation history with a clean surface has no influence on the subsequent flow stress coupled with the surface coverage of OH.

7 Summary and outlook

7.1 Summary

The first electro-chemo-mechanical coupling of NPG at the microscale was implemented in the present work, using a modified nanoindentation system combined with an electrochemical cell, which provides the opportunity to investigate the effects of microstructural aspects. Basing on that, we are focusing on the micromechanical behavior, with and without electrochemical control, of NPG micropillars with different microstructural length scales and deformation length scales, in order to study the interdependencies of deformation, microstructural length scale and electrochemical environment.

First, the consequence of intrinsic and extrinsic size effects in the mechanical behaviors of NPG was addressed by conducting nanoindentation and uniaxial microcompression on bulk NPG and micropillars, respectively. With the change of ligament size (L) and pillar diameter (D), the ratio $\alpha=D/L$ of the pillars can be varied from 160 to 6. The nanoindentation results indicated that both hardness and elastic modulus decrease with increasing ligament size, in agreement with results in other studies [65, 185]. Furthermore, based on the microcompression results of pillars with varying α, it was found that the mechanical response shows identical behavior for α larger than 20, while both flow stress and elastic modulus decrease with decreasing diameter when α is below 20, as evidenced for pillars with $L=350\ nm$. Therefore, a critical ratio ($\alpha=20$) is defined here, above which the test structure with $L=350\ nm$ can be considered a representative volume element (RVE) of NPG resulting in reproducible mechanical responses and uniform deformation. Below this critical ratio, the mechanical response shows dependence on the pillar diameter. Furthermore, stochastic behavior along with non-uniform deformation and failure were observed when $\alpha<10$, suggesting the size of the mechanical load-bearing units of NPG with $L=350\ nm$ is about 10 times the ligament diameter.

In the case of *in situ* microcompression in an electrolyte, a novel multiple load-unloading profile was developed to decouple the contribution of displacement due to the actuation from the compression-induced deformation. The flow stress of pillars measured under potential jumps exhibited the same trend as the corresponding macroscopic results: strength can be

enhanced significantly during the adsorption region and this response is reversible. Interestingly, the elastic modulus was found not to depend on the electrochemical potential, a result in contrast to that found with dynamic mechanical analysis (DMA) on macro-scale NPG. The reason for this discrepancy is still not fully understood.

The influence of intrinsic and extrinsic size, as well as deformation history on the electro-chemo-mechanical coupling of NPG were also studied here. The engineering stress-strain curves of pillars fabricated in disc-shaped NPG samples and NPG films, where α ranges from 228 to 7.5, indicated that the relative change in strength ($\Delta\sigma/\sigma_{off}$) induced by the applied positive potential, i.e. surface coverage of OH, decreases significantly with increasing ligament size, implying that the absolute change ($\Delta\sigma$) in strength and the strength itself (σ_{off}) scale differently with the ligament size. A change in pillar size, however, does not affect the potential-induced strengthening for a fixed ligament size, even though α declined below 10, implying that the critical ratio of RVE in terms of functional behavior is smaller than the corresponding ratio (20) of RVE regarding mechanical behavior. In addition, the flow stress of the pillars, which experienced different amounts of plastic deformation before potential changes from clean to oxygen covered surface, demonstrated that the deformation path of network structure with a clean surface has no influence on the subsequent flow stress coupled with OH adsorption.

7.2 Outlook

Electro-chemo-mechanical coupling at the microscale has been carried out on NPG samples in the present thesis using a modified nanoindenter, with which we investigate the effects of deformation length scales, microstructure length scales and deformation history. Due to the complex structure of NPG, the effects of other structural elements, such as grain boundaries and local geometries, are also worth investigating in further research, for a comprehensive understanding of the correlation between structure and mechanical properties coupled with electrochemical potentials.

Basing on the compression results displayed in chapter 5, the elastic modulus of NPG pillars was found to be insensitive to the surface state, inconsistent with the bulk dynamic mechanical analysis results (DAM), the reason for this discrepancy and the coupling between NPG elasticity and electrochemical potential need further investigations. Furthermore, the flow stress behavior shows a strong dependence on electrode potentials, in agreement well with the corresponding macroscopic results, but the underlying mechanism is still not fully understood. Although the strengthening induced by adsorption and its variation with strain is thought to be

based on the interaction between dislocations and adsorbates at the surface, it lacks supports from experimental evidence. It would be challenging but useful to characterize the dislocation behavior of different surface states during micromechanical testing under potential control using transmission electron microscope (TEM) technique, in order to understand the corresponding mechanisms.

Except for micropillars of NPG, the mechanical behaviors coupled with electrochemical potentials of individual ligaments is of interest to explore, since oxidation adsorption of NPG occurs on the ligament surface. *In situ* mechanical testing of Au micro- or nano-pillars with different external shapes and crystallographic orientations that are considered as representative of a single ligament, can be carried out using the indenter by the experimental approach developed in the current work. It would help to understand how the single ligaments transfer their functionality to the overall network structure through comparing and analyzing the electro-chemo-mechanical coupling of Au pillars and NPG.

8 Bibliography

[1] J. Weissmüller, K. Sieradzki, Dealloyed nanoporous materials with interface-controlled behavior, MRS Bulletin 43(1) (2018) 14-19.

[2] D. Kramer, R.N. Viswanath, J. Weissmüller, Surface-Stress Induced Macroscopic Bending of Nanoporous Gold Cantilevers, Nano Letters 4(5) (2004) 793-796.

[3] C. Stenner, L.H. Shao, N. Mameka, J. Weissmüller, Piezoelectric Gold: Strong Charge‐Load Response in a Metal‐Based Hybrid Nanomaterial, Advanced functional materials 26(28) (2016) 5174-5181.

[4] Z. Wang, P. Liu, J. Han, C. Cheng, S. Ning, A. Hirata, T. Fujita, M. Chen, Engineering the internal surfaces of three-dimensional nanoporous catalysts by surfactant-modified dealloying, Nature Communications 8(1) (2017) 1066.

[5] H.J. Jin, D. Kramer, Y. Ivanisenko, J. Weissmüller, Macroscopically Strong Nanoporous Pt Prepared by Dealloying, Advanced Engineering Materials 9(10) (2007) 849-854.

[6] I.C. Cheng, A.M. Hodge, Morphology, Oxidation, and Mechanical Behavior of Nanoporous Cu Foams, Advanced Engineering Materials 14(4) (2012) 219-226.

[7] J.H. Shim, Y.S. Kim, M. Kang, C. Lee, Y. Lee, Electrocatalytic activity of nanoporous Pd and Pt: effect of structural features, Physical Chemistry Chemical Physics 14(11) (2012) 3974-3979.

[8] J. Erlebacher, M.J. Aziz, A. Karma, N. Dimitrov, K. Sieradzki, Evolution of nanoporosity in dealloying, Nature 410(6827) (2001) 450-453.

[9] F. Kertis, J. Snyder, L. Govada, S. Khurshid, N. Chayen, J. Erlebacher, Structure/processing relationships in the fabrication of nanoporous gold, Jom 62(6) (2010) 50-56.

[10] L. Lührs, B. Zandersons, N. Huber, J. Weissmüller, Plastic Poisson's Ratio of Nanoporous Metals: A Macroscopic Signature of Tension–Compression Asymmetry at the Nanoscale, Nano Letters 17(10) (2017) 6258-6266.

[11] D.A. Crowson, D. Farkas, S.G. Corcoran, Mechanical stability of nanoporous metals with small ligament sizes, Scripta Materialia 61(5) (2009) 497-499.

[12] D. Lee, X. Wei, X. Chen, M. Zhao, S.C. Jun, J. Hone, E.G. Herbert, W.C. Oliver, J.W. Kysar, Microfabrication and mechanical properties of nanoporous gold at the nanoscale, Scripta Materialia 56(5) (2007) 437-440.

[13] R.N. Viswanath, S.R. Polaki, R. Rajaraman, S. Abhaya, V.A. Chirayath, G. Amarendra, C.S. Sundar, On the scaling behavior of hardness with ligament diameter of nanoporous-Au: Constrained motion of dislocations along the ligaments, Applied Physics Letters 104(23) (2014) 233108.

[14] S. Parida, D. Kramer, C.A. Volkert, H. Rösner, J. Erlebacher, J. Weissmüller, Volume Change during the Formation of Nanoporous Gold by Dealloying, Physical Review Letters 97(3) (2006) 035504.

[15] R. Dou, B. Derby, Deformation mechanisms in gold nanowires and nanoporous gold, Philosophical Magazine 91(7-9) (2011) 1070-1083.

[16] N. Mameka, K. Wang, J. Markmann, E.T. Lilleodden, J. Weissmüller, Nanoporous Gold—Testing Macro-scale Samples to Probe Small-scale Mechanical Behavior, Materials Research Letters 4(1) (2016) 27-36.

[17] J. Biener, A.M. Hodge, A.V. Hamza, L.M. Hsiung, J.H. Satcher, Nanoporous Au: A high yield strength material, Journal of Applied Physics 97(2) (2004) 024301.

[18] L.-Z. Liu, X.-L. Ye, H.-J. Jin, Interpreting anomalous low-strength and low-stiffness of nanoporous gold: Quantification of network connectivity, Acta Materialia 118 (2016) 77-87.

[19] G. Pia, F. Delogu, Nanoporous Au: Statistical analysis of morphological features and evaluation of their influence on the elastic deformation behavior by phenomenological modeling, Acta Materialia 85 (2015) 250-260.

[20] E.W. Andrews, G. Gioux, P. Onck, L.J. Gibson, Size effects in ductile cellular solids. Part II: experimental results, International Journal of Mechanical Sciences 43(3) (2001) 701-713.

[21] S. Shi, Y. Li, B.-N. Ngo-Dinh, J. Markmann, J. Weissmüller, Scaling behavior of stiffness and strength of hierarchical network nanomaterials, Science 371(6533) (2021) 1026.

[22] H. Angerstein-Kozlowska, B.E. Conway, A. Hamelin, L. Stoicoviciu, Elementary steps of electrochemical oxidation of single-crystal planes of Au—I. Chemical basis of processes involving geometry of anions and the electrode surfaces, Electrochimica Acta 31(8) (1986) 1051-1061.

[23] N. Mameka, J. Markmann, H.-J. Jin, J. Weissmüller, Electrical stiffness modulation—confirming the impact of surface excess elasticity on the mechanics of nanomaterials, Acta Materialia 76 (2014) 272-280.

[24] H.-J. Jin, J. Weissmüller, A Material with Electrically Tunable Strength and Flow Stress, Science 332(6034) (2011) 1179.

[25] S.G. Corcoran, S.R. Brankovic, N. Dimitrov, K. Sieradzki, Nanoindentation of atomically modified surfaces, MRS Online Proceedings Library Archive 505 (1997).

[26] S.G. Corcoran, R.J. Colton, E.T. Lilleodden, W.W. Gerberich, Anomalous plastic deformation at surfaces: Nanoindentation of gold single crystals, Physical Review B 55(24) (1997) R16057-R16060.

[27] A. Barnoush, J. Dake, N. Kheradmand, H. Vehoff, Examination of hydrogen embrittlement in FeAl by means of in situ electrochemical micropillar compression and nanoindentation techniques, Intermetallics 18(7) (2010) 1385-1389.

[28] A. Barnoush, H. Vehoff, In situ electrochemical nanoindentation: A technique for local examination of hydrogen embrittlement, Corrosion Science 50(1) (2008) 259-267.

[29] A. Barnoush, H. Vehoff, Recent developments in the study of hydrogen embrittlement: Hydrogen effect on dislocation nucleation, Acta Materialia 58(16) (2010) 5274-5285.

[30] B.C. Tappan, S.A. Steiner Iii, E.P. Luther, Nanoporous Metal Foams, Angewandte Chemie International Edition 49(27) (2010) 4544-4565.

[31] R. Zeis, A. Mathur, G. Fritz, J. Lee, J. Erlebacher, Platinum-plated nanoporous gold: An efficient, low Pt loading electrocatalyst for PEM fuel cells, Journal of Power Sources 165(1) (2007) 65-72.

[32] A. Wittstock, J. Biener, M. Bäumer, Nanoporous gold: a new material for catalytic and sensor applications, Physical Chemistry Chemical Physics 12(40) (2010) 12919-12930.

[33] A.M. Hodge, J.R. Hayes, J.A. Caro, J. Biener, A.V. Hamza, Characterization and Mechanical Behavior of Nanoporous Gold, Advanced Engineering Materials 8(9) (2006) 853-857.

[34] T.J. Balk, C. Eberl, Y. Sun, K.J. Hemker, D.S. Gianola, Tensile and compressive microspecimen testing of bulk nanoporous gold, JOM 61(12) (2009) 26.

[35] J. Weissmüller, R.C. Newman, H.-J. Jin, A.M. Hodge, J.W. Kysar, Nanoporous Metals by Alloy Corrosion: Formation and Mechanical Properties, MRS Bulletin 34(8) (2011) 577-586.

[36] N. Badwe, X. Chen, K. Sieradzki, Mechanical properties of nanoporous gold in tension, Acta Materialia 129 (2017) 251-258.

[37] R. Xia, R.N. Wu, Y.L. Liu, X.Y. Sun, The Role of Computer Simulation in Nanoporous Metals—A Review, Materials 8(8) (2015) 5060-5083.

[38] X.-Y. Sun, G.-K. Xu, X. Li, X.-Q. Feng, H. Gao, Mechanical properties and scaling laws of nanoporous gold, Journal of Applied Physics 113(2) (2013) 023505.

[39] S. Mathesan, D. Mordehai, On the yielding and densification of nanoporous Au nanopillars in molecular dynamics simulations, Computational Materials Science 191 (2021) 110307.

[40] M.F. Ashby, L.J. Gibson, Cellular solids: structure and properties, Press Syndicate of the University of Cambridge, Cambridge, UK (1997) 175-231.

[41] L.J. Gibson, Cellular Solids, MRS Bulletin 28(4) (2003) 270-274.

[42] R. Dou, B. Derby, Strain gradients and the strength of nanoporous gold, Journal of Materials Research 25(4) (2010) 746-753.

[43] R. Li, K. Sieradzki, Ductile-brittle transition in random porous Au, Physical Review Letters 68(8) (1992) 1168-1171.

[44] T.G. Nieh, K. Higashi, J. Wadsworth, Effect of cell morphology on the compressive properties of open-cell aluminum foams, Materials Science and Engineering: A 283(1) (2000) 105-110.

[45] J.R. Greer, W.C. Oliver, W.D. Nix, Size dependence of mechanical properties of gold at the micron scale in the absence of strain gradients, Acta Materialia 53(6) (2005) 1821-1830.

[46] M.D. Uchic, D.M. Dimiduk, J.N. Florando, W.D. Nix, Sample Dimensions Influence Strength and Crystal Plasticity, Science 305(5686) (2004) 986.

[47] Z.W. Shan, R.K. Mishra, S.A. Syed Asif, O.L. Warren, A.M. Minor, Mechanical annealing and source-limited deformation in submicrometre-diameter Ni crystals, Nature Materials 7(2) (2008) 115-119.

[48] D.M. Dimiduk, M.D. Uchic, T.A. Parthasarathy, Size-affected single-slip behavior of pure nickel microcrystals, Acta Materialia 53(15) (2005) 4065-4077.

[49] C.P. Frick, B.G. Clark, S. Orso, A.S. Schneider, E. Arzt, Size effect on strength and strain hardening of small-scale [111] nickel compression pillars, Materials Science and Engineering: A 489(1) (2008) 319-329.

[50] A. Rinaldi, P. Peralta, C. Friesen, K. Sieradzki, Sample-size effects in the yield behavior of nanocrystalline nickel, Acta Materialia 56(3) (2008) 511-517.

[51] D. Kiener, A.M. Minor, Source-controlled yield and hardening of Cu(100) studied by in situ transmission electron microscopy, Acta Materialia 59(4) (2011) 1328-1337.

[52] D. Kiener, W. Grosinger, G. Dehm, R. Pippan, A further step towards an understanding of size-dependent crystal plasticity: In situ tension experiments of miniaturized single-crystal copper samples, Acta Materialia 56(3) (2008) 580-592.

[53] G. Dehm, Miniaturized single-crystalline fcc metals deformed in tension: New insights in size-dependent plasticity, Progress in Materials Science 54(6) (2009) 664-688.

[54] M. Shell De Guzman, G. Neubauer, P. Flinn, W.D. Nix, The Role of Indentation Depth on the Measured Hardness of Materials, MRS Proceedings 308 (1993) 613.

[55] J.R. Greer, W.D. Nix, Nanoscale gold pillars strengthened through dislocation starvation, Physical Review B 73(24) (2006) 245410.

[56] W.D. Nix, J.R. Greer, G. Feng, E.T. Lilleodden, Deformation at the nanometer and micrometer length scales: Effects of strain gradients and dislocation starvation, Thin Solid Films 515(6) (2007) 3152-3157.

[57] C.A. Volkert, E.T. Lilleodden, Size effects in the deformation of sub-micron Au columns, Philosophical Magazine 86(33-35) (2006) 5567-5579.

[58] J.R. Greer, J.T.M. De Hosson, Plasticity in small-sized metallic systems: Intrinsic versus extrinsic size effect, Progress in Materials Science 56(6) (2011) 654-724.

[59] V.S. Deshpande, A. Needleman, E. Van der Giessen, Plasticity size effects in tension and compression of single crystals, Journal of the Mechanics and Physics of Solids 53(12) (2005) 2661-2691.

[60] C. Volkert, E. Lilleodden, D. Kramer, J. Weissmüller, Approaching the theoretical strength in nanoporous Au, Applied Physics Letters 89(6) (2006) 061920.

[61] E.M. Saviëtìskii, Handbook of precious metals, 1989.

[62] J. Biener, A.M. Hodge, J.R. Hayes, C.A. Volkert, L.A. Zepeda-Ruiz, A.V. Hamza, F.F. Abraham, Size Effects on the Mechanical Behavior of Nanoporous Au, Nano Letters 6(10) (2006) 2379-2382.

[63] I. McCue, E. Benn, B. Gaskey, J. Erlebacher, Dealloying and Dealloyed Materials, Annual Review of Materials Research 46(1) (2016) 263-286.

[64] J. Biener, A.M. Hodge, A.V. Hamza, L.M. Hsiung, J.H.S. Jr., Nanoporous Au: A high yield strength material, Journal of Applied Physics 97(2) (2005) 024301.

[65] A.M. Hodge, J. Biener, J.R. Hayes, P.M. Bythrow, C.A. Volkert, A.V. Hamza, Scaling equation for yield strength of nanoporous open-cell foams, Acta Materialia 55(4) (2007) 1343-1349.

[66] I.C. Cheng, A.M. Hodge, Strength scale behavior of nanoporous Ag, Pd and Cu foams, Scripta Materialia 69(4) (2013) 295-298.

[67] T.A. Parthasarathy, S.I. Rao, D.M. Dimiduk, M.D. Uchic, D.R. Trinkle, Contribution to size effect of yield strength from the stochastics of dislocation source lengths in finite samples, Scripta Materialia 56(4) (2007) 313-316.

[68] M.F. Horstemeyer, M.I. Baskes, S.J. Plimpton, Length scale and time scale effects on the plastic flow of fcc metals, Acta Materialia 49(20) (2001) 4363-4374.

[69] D. Farkas, A. Caro, E. Bringa, D. Crowson, Mechanical response of nanoporous gold, Acta Materialia 61(9) (2013) 3249-3256.

[70] V.S. Deshpande, A. Needleman, E. Van der Giessen, Discrete dislocation modeling of fatigue crack propagation, Acta Materialia 50(4) (2002) 831-846.

[71] A.A. Benzerga, N.F. Shaver, Scale dependence of mechanical properties of single crystals under uniform deformation, Scripta Materialia 54(11) (2006) 1937-1941.

[72] J. Senger, D. Weygand, P. Gumbsch, O. Kraft, Discrete dislocation simulations of the plasticity of micro-pillars under uniaxial loading, Scripta Materialia 58(7) (2008) 587-590.

[73] H. Tang, K.W. Schwarz, H.D. Espinosa, Dislocation escape-related size effects in single-crystal micropillars under uniaxial compression, Acta Materialia 55(5) (2007) 1607-1616.

[74] C.R. Weinberger, W. Cai, Surface-controlled dislocation multiplication in metal micropillars, Proceedings of the National Academy of Sciences 105(38) (2008) 14304.

[75] S.I. Rao, D.M. Dimiduk, T.A. Parthasarathy, M.D. Uchic, M. Tang, C. Woodward, Athermal mechanisms of size-dependent crystal flow gleaned from three-dimensional discrete dislocation simulations, Acta Materialia 56(13) (2008) 3245-3259.

[76] S.H. Oh, M. Legros, D. Kiener, G. Dehm, In situ observation of dislocation nucleation and escape in a submicrometre aluminium single crystal, Nature Materials 8(2) (2009) 95-100.

[77] D. Kiener, A.M. Minor, Source Truncation and Exhaustion: Insights from Quantitative in situ TEM Tensile Testing, Nano Letters 11(9) (2011) 3816-3820.

[78] H.-J. Jin, L. Kurmanaeva, J. Schmauch, H. Rösner, Y. Ivanisenko, J. Weissmüller, Deforming nanoporous metal: Role of lattice coherency, Acta Materialia 57(9) (2009) 2665-2672.

[79] A. Mathur, J. Erlebacher, Size dependence of effective Young's modulus of nanoporous gold, Applied physics letters 90(6) (2007) 061910.

[80] B. Wu, A. Heidelberg, J.J. Boland, Mechanical properties of ultrahigh-strength gold nanowires, Nature Materials 4(7) (2005) 525-529.

[81] E. Seker, J.T. Gaskins, H. Bart-Smith, J. Zhu, M.L. Reed, G. Zangari, R. Kelly, M.R. Begley, The effects of post-fabrication annealing on the mechanical properties of freestanding nanoporous gold structures, Acta Materialia 55(14) (2007) 4593-4602.

[82] R. Newman, S. Corcoran, J. Erlebacher, M. Aziz, K. Sieradzki, Alloy corrosion, MRS Bulletin-Materials Research Society 24 (1999) 24-28.

[83] S.J.A. Koh, H.P. Lee, Molecular dynamics simulation of size and strain rate dependent mechanical response of FCC metallic nanowires, Nanotechnology 17(14) (2006) 3451-3467.

[84] E. Seker, J.T. Gaskins, H. Bart-Smith, J. Zhu, M.L. Reed, G. Zangari, R. Kelly, M.R. Begley, The effects of annealing prior to dealloying on the mechanical properties of nanoporous gold microbeams, Acta Materialia 56(3) (2008) 324-332.

[85] L.A. Zepeda-Ruiz, B. Sadigh, J. Biener, A.M. Hodge, A.V. Hamza, Mechanical response of freestanding Au nanopillars under compression, Applied Physics Letters 91(10) (2007) 101907.

[86] Y. Sun, J. Ye, Z. Shan, A.M. Minor, T.J. Balk, The mechanical behavior of nanoporous gold thin films, JOM 59(9) (2007) 54-58.

[87] R.C. Cammarata, Surface and interface stress effects in thin films, Progress in Surface Science 46(1) (1994) 1-38.

[88] H.L. Duan, J. Wang, B.L. Karihaloo, Theory of Elasticity at the Nanoscale, in: H. Aref, E. van der Giessen (Eds.), Advances in Applied Mechanics, Elsevier2009, pp. 1-68.

[89] R. Dingreville, J. Qu, C. Mohammed, Surface free energy and its effect on the elastic behavior of nano-sized particles, wires and films, Journal of the Mechanics and Physics of Solids 53(8) (2005) 1827-1854.

[90] J. He, C.M. Lilley, Surface Effect on the Elastic Behavior of Static Bending Nanowires, Nano Letters 8(7) (2008) 1798-1802.

[91] S. Cuenot, C. Frétigny, S. Demoustier-Champagne, B. Nysten, Surface tension effect on the mechanical properties of nanomaterials measured by atomic force microscopy, Physical Review B 69(16) (2004) 165410.

[92] G.Y. Jing, H.L. Duan, X.M. Sun, Z.S. Zhang, J. Xu, Y.D. Li, J.X. Wang, D.P. Yu, Surface effects on elastic properties of silver nanowires: Contact atomic-force microscopy, Physical Review B 73(23) (2006) 235409.

[93] M.T. McDowell, A.M. Leach, K. Gall, On The Elastic Modulus of Metallic Nanowires, Nano Letters 8(11) (2008) 3613-3618.

[94] L.Y. Chen, G. Richter, J.P. Sullivan, D.S. Gianola, Lattice Anharmonicity in Defect-Free Pd Nanowhiskers, Physical Review Letters 109(12) (2012) 125503.

[95] X. Li, T. Ono, Y. Wang, M. Esashi, Ultrathin single-crystalline-silicon cantilever resonators: Fabrication technology and significant specimen size effect on Young's modulus, Applied Physics Letters 83(15) (2003) 3081-3083.

[96] S.G. Nilsson, X. Borrisé, L. Montelius, Size effect on Young's modulus of thin chromium cantilevers, Applied Physics Letters 85(16) (2004) 3555-3557.

[97] L. Qiao, X. Zheng, Effect of surface stress on the stiffness of micro/nanocantilevers: nanowire elastic modulus measured by nano-scale tensile and vibrational techniques, Journal of Applied Physics 113(1) (2013) 013508.

[98] H. Liang, M. Upmanyu, H. Huang, Size-dependent elasticity of nanowires: Nonlinear effects, Physical Review B 71(24) (2005) 241403.

[99] H. Petrova, J. Perez-Juste, Z. Zhang, J. Zhang, T. Kosel, G.V. Hartland, Crystal structure dependence of the elastic constants of gold nanorods, Journal of Materials Chemistry 16(40) (2006) 3957-3963.

[100] J. Diao, K. Gall, M. L. Dunn, Atomistic simulation of the structure and elastic properties of gold nanowires, Journal of the Mechanics and Physics of Solids 52(9) (2004) 1935-1962.

[101] B.A.M. Elsner, S. Müller, S. Bargmann, J. Weissmüller, Surface excess elasticity of gold: Ab initio coefficients and impact on the effective elastic response of nanowires, Acta Materialia 124 (2017) 468-477.

[102] J. Jiao, N. Huber, Deformation mechanisms in nanoporous metals: Effect of ligament shape and disorder, Computational Materials Science 127 (2017) 194-203.

[103] N. Huber, Connections Between Topology and Macroscopic Mechanical Properties of Three-Dimensional Open-Pore Materials, Frontiers in Materials 5(69) (2018).

[104] C. Richert, N. Huber, A Review of Experimentally Informed Micromechanical Modeling of Nanoporous Metals: From Structural Descriptors to Predictive Structure–Property Relationships, Materials 13(15) (2020) 3307.

[105] N. Huber, R.N. Viswanath, N. Mameka, J. Markmann, J. Weißmüller, Scaling laws of nanoporous metals under uniaxial compression, Acta Materialia 67 (2014) 252-265.

[106] B. Roschning, N. Huber, Scaling laws of nanoporous gold under uniaxial compression: Effects of structural disorder on the solid fraction, elastic Poisson's ratio, Young's modulus and yield strength, Journal of the Mechanics and Physics of Solids 92 (2016) 55-71.

[107] K.R. Mangipudi, E. Epler, C.A. Volkert, Topology-dependent scaling laws for the stiffness and strength of nanoporous gold, Acta Materialia 119 (2016) 115-122.

[108] K.R. Mangipudi, E. Epler, C.A. Volkert, Morphological similarity and structure-dependent scaling laws of nanoporous gold from different synthesis methods, Acta Materialia 140 (2017) 337-343.

[109] B.-N.D. Ngô, A. Stukowski, N. Mameka, J. Markmann, K. Albe, J. Weissmüller, Anomalous compliance and early yielding of nanoporous gold, Acta Materialia 93 (2015) 144-155.

[110] N.J. Briot, T. Kennerknecht, C. Eberl, T.J. Balk, Mechanical properties of bulk single crystalline nanoporous gold investigated by millimetre-scale tension and compression testing, Philosophical Magazine 94(8) (2014) 847-866.

[111] A. Odgaard, H.J.G. Gundersen, Quantification of connectivity in cancellous bone, with special emphasis on 3-D reconstructions, Bone 14(2) (1993) 173-182.

[112] A. Odgaard, Three-dimensional methods for quantification of cancellous bone architecture, Bone 20(4) (1997) 315-328.

[113] L.-Z. Liu, H.-J. Jin, Scaling equation for the elastic modulus of nanoporous gold with “fixed” network connectivity, Applied Physics Letters 110(21) (2017) 211902.

[114] K. Hu, M. Ziehmer, K. Wang, E.T. Lilleodden, Nanoporous gold: 3D structural analyses of representative volumes and their implications on scaling relations of mechanical behaviour, Philosophical Magazine 96(32-34) (2016) 3322-3335.

[115] K. Hu, Micromechanical and three-dimensional microstructural characterization of nanoporous gold-epoxy composites, Technische Universität Hamburg-Harburg, 2017.

[116] C. Soyarslan, S. Bargmann, M. Pradas, J. Weissmüller, 3D stochastic bicontinuous microstructures: Generation, topology and elasticity, Acta Materialia 149 (2018) 326-340.

[117] H. Gleiter, J. Weissmüller, O. Wollersheim, R. Würschum, Nanocrystalline materials: a way to solids with tunable electronic structures and properties?, Acta Materialia 49(4) (2001) 737-745.

[118] C.G. Zoski, Handbook of electrochemistry, Elsevier2006.

[119] A.J. Bard, L.R. Faulkner, Fundamentals and applications, Electrochemical Methods 2(482) (2001) 580-632.

[120] W. Schmickler, E. Santos, Interfacial electrochemistry, Springer Science & Business Media2010.

[121] O.M. Magnussen, Ordered Anion Adlayers on Metal Electrode Surfaces, Chemical Reviews 102(3) (2002) 679-726.

[122] H. Ibach, Physics of surfaces and interfaces, Springer2006.

[123] F. El Kadiri, R. Faure, R. Durand, Electrochemical reduction of molecular oxygen on platinum single crystals, Journal of Electroanalytical Chemistry and Interfacial Electrochemistry 301(1) (1991) 177-188.

[124] B.E. Conway, Electrochemical oxide film formation at noble metals as a surface-chemical process, Progress in Surface Science 49(4) (1995) 331-452.

[125] H. Angerstein-Kozlowska, B.E. Conway, A. Hamelin, L. Stoicoviciu, Elementary steps of electrochemical oxidation of single-crystal planes of Au Part II. A chemical and structural basis of oxidation of the (111) plane, Journal of Electroanalytical Chemistry and Interfacial Electrochemistry 228(1) (1987) 429-453.

[126] H. Angerstein-Kozlowska, B.E. Conway, K. Tellefsen, B. Barnett, Stochastically-gated surface processes involving anions in oxidation of Au: time-resolution of processes down to 0.25% coverages and 50 μs time-scales, Electrochimica Acta 34(8) (1989) 1045-1056.

[127] D.M. Kolb, J. Schneider, Surface reconstruction in electrochemistry: Au(100-(5 × 20), Au(111)-(1 × 23) and Au(110)-(1 × 2), Electrochimica Acta 31(8) (1986) 929-936.

[128] H. Angerstein-Kozlowska, B.E. Conway, B. Barnett, J. Mozota, The role of ion adsorption in surface oxide formation and reduction at noble metals: General features of the surface process, Journal of Electroanalytical Chemistry and Interfacial Electrochemistry 100(1) (1979) 417-446.

[129] J. Lipkowski, Z. Shi, A. Chen, B. Pettinger, C. Bilger, Ionic adsorption at the Au(111) electrode, Electrochimica Acta 43(19) (1998) 2875-2888.

[130] J. Biener, A. Wittstock, T.F. Baumann, J. Weissmüller, M. Bäumer, A.V. Hamza, Surface Chemistry in Nanoscale Materials, Materials 2(4) (2009).

[131] H. Lüth, Solid surfaces, interfaces and thin films, Springer2001.

[132] R. Shuttleworth, The Surface Tension of Solids, Proceedings of the Physical Society. Section A 63(5) (1950) 444-457.

[133] W. Haiss, Surface stress of clean and adsorbate-covered solids, Reports on Progress in Physics 64(5) (2001) 591-648.

[134] J. Weissmüller, D. Kramer, Balance of Force at Curved Solid Metal−Liquid Electrolyte Interfaces, Langmuir 21(10) (2005) 4592-4603.

[135] D. Kramer, J. Weissmüller, A note on surface stress and surface tension and their interrelation via Shuttleworth's equation and the Lippmann equation, Surface Science 601(14) (2007) 3042-3051.

[136] J.W. Cahn, Surface stress and the chemical equilibrium of small crystals—I. the case of the isotropic surface, Acta Metallurgica 28(10) (1980) 1333-1338.

[137] J. Weissmüller, Electrocapillarity of solids and its impact on heterogeneous catalysis, Electrocatalysis 14 (2013) 163-220.

[138] D. Kramer, Dependence of surface stress, surface energy and surface tension on potential and charge, Physical Chemistry Chemical Physics 10(1) (2008) 168-177.

[139] J. Biener, A. Wittstock, L.A. Zepeda-Ruiz, M.M. Biener, V. Zielasek, D. Kramer, R.N. Viswanath, J. Weissmüller, M. Bäumer, A.V. Hamza, Surface-chemistry-driven actuation in nanoporous gold, Nature Materials 8 (2008) 47.

[140] D. Wang, P. Schaaf, Nanoporous gold nanoparticles, Journal of Materials Chemistry 22(12) (2012) 5344-5348.

[141] F. Bødker, S. Mørup, S. Linderoth, Surface effects in metallic iron nanoparticles, Physical Review Letters 72(2) (1994) 282-285.

[142] L.-B. He, L. Zhang, L.-P. Tang, J. Sun, Q.-B. Zhang, L.-T. Sun, Novel behaviors/properties of nanometals induced by surface effects, Materials Today Nano 1 (2018) 8-21.

[143] G.-F. Wang, X.-Q. Feng, Effects of surface elasticity and residual surface tension on the natural frequency of microbeams, Applied Physics Letters 90(23) (2007) 231904.

[144] S. Shi, J. Markmann, J. Weissmüller, Verifying Larché–Cahn elasticity, a milestone of 20th-century thermodynamics, Proceedings of the National Academy of Sciences 115(43) (2018) 10914.

[145] K. Wang, J. Weissmüller, Composites of Nanoporous Gold and Polymer, Advanced Materials 25(9) (2013) 1280-1284.

[146] K. Wang, C. Stenner, J. Weissmüller, A nanoporous gold-polypyrrole hybrid nanomaterial for actuation, Sensors and Actuators B: Chemical 248 (2017) 622-629.

[147] L.-H. Shao, H.-J. Jin, R. Viswanath, J. Weissmüller, Different measures for the capillarity-driven deformation of a nanoporous metal, EPL (Europhysics Letters) 89(6) (2010) 66001.

[148] H.-J. Jin, X.-L. Wang, S. Parida, K. Wang, M. Seo, J. Weissmüller, Nanoporous Au−Pt Alloys As Large Strain Electrochemical Actuators, Nano Letters 10(1) (2010) 187-194.

[149] J. Weissmüller, R.N. Viswanath, D. Kramer, P. Zimmer, R. Würschum, H. Gleiter, Charge-Induced Reversible Strain in a Metal, Science 300(5617) (2003) 312.

[150] H.-J. Jin, S. Parida, D. Kramer, J. Weissmüller, Sign-inverted surface stress-charge response in nanoporous gold, Surface Science 602(23) (2008) 3588-3594.

[151] S. Shi, J. Markmann, J. Weissmüller, Actuation by hydrogen electrosorption in hierarchical nanoporous palladium, Philosophical Magazine 97(19) (2017) 1571-1587.

[152] H.-J. Jin, J. Weissmüller, Bulk Nanoporous Metal for Actuation, Advanced Engineering Materials 12(8) (2010) 714-723.

[153] L.-Z. Liu, N. Mameka, J. Markmann, H.-J. Jin, J. Weissmüller, Surface-driven actuation: Sign reversal under load and surface load-memory effect, Physical Review Materials 3(6) (2019) 066001.

[154] J. Weissmüller, J.W. Cahn, Mean stresses in microstructures due to interface stresses: A generalization of a capillary equation for solids, Acta Materialia 45(5) (1997) 1899-1906.

[155] R.N. Viswanath, D. Kramer, J. Weissmüller, Adsorbate effects on the surface stress–charge response of platinum electrodes, Electrochimica Acta 53(6) (2008) 2757-2767.

[156] D.A. Crowson, D. Farkas, S.G. Corcoran, Geometric relaxation of nanoporous metals: The role of surface relaxation, Scripta Materialia 56(11) (2007) 919-922.

[157] J. Zhang, P. Liu, H. Ma, Y. Ding, Nanostructured Porous Gold for Methanol Electro-Oxidation, The Journal of Physical Chemistry C 111(28) (2007) 10382-10388.

[158] P. Rehbinder, New Physico-Chemical Phenomena in the Deformation and Mechanical Treatment of Solids*, Nature 159(4052) (1947) 866-867.

[159] A.R.C. Westwood, The rebinder effect and the adsorption-locking of dislocations in lithium fluoride, The Philosophical Magazine: A Journal of Theoretical Experimental and Applied Physics 7(76) (1962) 633-649.

[160] J. Gilman, The mechanism of surface effects in crystal plasticity, Philosophical Magazine 6(61) (1961) 159-161.

[161] M. Aponte-Roman, B. Mohanty, A.B. Mann, Chemomechanical effects of self-assembled monolayers on gold films, Acta Materialia 68 (2014) 52-60.

[162] R.M. Latanision, Surface effects in crystal plasticity, Advances in Colloid and Interface Science 6(4) (1976) 267-312.

[163] M. Metzger, T. Read, The effect of surface films on the creep of cadmium crystals, Trans. Met. Soc. AIME 212 (1958).

[164] K. Sieradzki, R.C. Newman, Brittle behavior of ductile metals during stress-corrosion cracking, Philosophical Magazine A 51(1) (1985) 95-132.

[165] P.A. Rehbinder, E.D. Shchukin, Surface phenomena in solids during deformation and fracture processes, Progress in Surface Science 3 (1972) 97-188.

[166] C.J. van der Wekken, The Effect of Cathodic Polarization on the Creep Rate of Gold, Journal of The Electrochemical Society 129(4) (1982) 706-711.

[167] C.J. van der Wekken, Surface Dislocation Pinning by Adsorbed Ions and Water Molecules, Journal of The Electrochemical Society 131(11) (1984) 2481-2483.

[168] S. Sun, X. Chen, N. Badwe, K. Sieradzki, Potential-dependent dynamic fracture of nanoporous gold, Nature Materials 14 (2015) 894.

[169] X.-L. Ye, H.-J. Jin, Electrochemical control of creep in nanoporous gold, Applied Physics Letters 103(20) (2013) 201912.

[170] N. Mameka, L. Lührs, S. Heissler, H. Gliemann, C. Wöll, Tailoring the Strength of Nanoporous Gold by Self-Assembled Monolayers of Alkanethiols, ACS Applied Nano Materials 1(12) (2018) 6613-6621.

[171] N. Mameka, J. Markmann, J. Weissmüller, On the impact of capillarity for strength at the nanoscale, Nature Communications 8(1) (2017) 1976.

[172] P. Wu, X.-L. Ye, L.-Z. Liu, H.-J. Jin, Monolayer oxide enhanced flow stress in nanoporous gold: the size dependence, Materials Research Letters 6(9) (2018) 508-514.

[173] W.G. Johnston, J.J. Gilman, Dislocation Multiplication in Lithium Fluoride Crystals, Journal of Applied Physics 31(4) (1960) 632-643.

[174] M. Gsell, P. Jakob, D. Menzel, Effect of Substrate Strain on Adsorption, Science 280(5364) (1998) 717.

[175] J. Erlebacher, Mechanism of Coarsening and Bubble Formation in High-Genus Nanoporous Metals, Physical Review Letters 106(22) (2011) 225504.

[176] S.V. Petegem, S. Brandstetter, R. Maass, A.M. Hodge, B.S. El-Dasher, J. Biener, B. Schmitt, C. Borca, H.V. Swygenhoven, On the Microstructure of Nanoporous Gold: An X-ray Diffraction Study, Nano Letters 9(3) (2009) 1158-1163.

[177] K.L.M. Elder, W.B. Andrews, M. Ziehmer, N. Mameka, C. Kirchlechner, A. Davydok, J.-S. Micha, A.F. Chadwick, E.T. Lilleodden, K. Thornton, P.W. Voorhees, Grain boundary formation through particle detachment during coarsening of nanoporous metals, Proceedings of the National Academy of Sciences 118(30) (2021) e2104132118.

[178] J. Hütsch, E.T. Lilleodden, The influence of focused-ion beam preparation technique on microcompression investigations: Lathe vs. annular milling, Scripta Materialia 77 (2014) 49-51.

[179] C.A. Volkert, A.M. Minor, Focused Ion Beam Microscopy and Micromachining, MRS Bulletin 32(5) (2007) 389-399.

[180] W.C. Oliver, G.M. Pharr, An improved technique for determining hardness and elastic modulus using load and displacement sensing indentation experiments, Journal of Materials Research 7(6) (1992) 1564-1583.

[181] W.C. Oliver, G.M. Pharr, Measurement of hardness and elastic modulus by instrumented indentation: Advances in understanding and refinements to methodology, Journal of Materials Research 19(1) (2004) 3.

[182] I.N. Sneddon, The relation between load and penetration in the axisymmetric boussinesq problem for a punch of arbitrary profile, International Journal of Engineering Science 3(1) (1965) 47-57.

[183] H. Jeon, N.-R. Kang, E.-J. Gwak, J.-i. Jang, H.N. Han, J.Y. Hwang, S. Lee, J.-Y. Kim, Self-similarity in the structure of coarsened nanoporous gold, Scripta Materialia 137 (2017) 46-49.

[184] M. Ziehmer, K. Hu, K. Wang, E.T. Lilleodden, A principle curvatures analysis of the isothermal evolution of nanoporous gold: Quantifying the characteristic length-scales, Acta Materialia 120 (2016) 24-31.

[185] M. Hakamada, M. Mabuchi, Mechanical strength of nanoporous gold fabricated by dealloying, Scripta Materialia 56(11) (2007) 1003-1006.

[186] N.A. Stelmashenko, M.G. Walls, L.M. Brown, Y.V. Milman, Microindentations on W and Mo oriented single crystals: An STM study, Acta Metallurgica et Materialia 41(10) (1993) 2855-2865.

[187] W.D. Nix, H. Gao, Indentation size effects in crystalline materials: A law for strain gradient plasticity, Journal of the Mechanics and Physics of Solids 46(3) (1998) 411-425.

[188] P.R. Onck, E.W. Andrews, L.J. Gibson, Size effects in ductile cellular solids. Part I: modeling, International Journal of Mechanical Sciences 43(3) (2001) 681-699.

[189] P.J. Imrich, C. Kirchlechner, C. Motz, G. Dehm, Differences in deformation behavior of bicrystalline Cu micropillars containing a twin boundary or a large-angle grain boundary, Acta Materialia 73 (2014) 240-250.

[190] E.O. Hall, The Deformation and Ageing of Mild Steel: III Discussion of Results, Proceedings of the Physical Society. Section B 64(9) (1951) 747-753.

[191] C. Wang, H. Liu, C. Wang, J. Xu, P. Zhang, B. Guo, D. Shan, Z. Wang, Interactive effects of height-to-diameter ratio and strain on tribological behavior in micro compression of pure nickel cylinder, International Journal of Mechanical Sciences 144 (2018) 452-460.

[192] A. Wittstock, J. Biener, J. Erlebacher, M. Bäumer, Nanoporous gold: from an ancient technology to a high-tech material, Royal Society of Chemistry2012.